2021

# Acquisition of 3D shapes of moving objects using fringe projection profilometry

Chengpu Duan

UNIVERSITY
OF WOLLONGONG
AUSTRALIA

# ACQUISITION OF 3D SHAPES OF MOVING OBJECTS USING FRINGE PROJECTION PROFILOMETRY


**Chengpu Duan**

Supervisors:
**Dr. Jun Tong**
**Prof. Jiangtao Xi**
**Prof. Philip Ogunbona**


This thesis is presented as part of the requirement for the conferral of the degree:
**Doctor of Philosophy**


University of Wollongong

School of Electrical, Computer and Telecommunications Engineering

August 2021

# CERTIFICATION

I, Chengpu Duan, declare that this thesis submitted in fulfilment of the requirements for the conferral of the Doctor of Philosophy, from the University of Wollongong, is wholly my own work unless otherwise referenced or acknowledged. This document has not been submitted for qualifications at any other academic institution.

***Chengpu Duan***

31st August 2021

# ACKNOWLEDGMENTS

Throughout my PhD period, I have received a great deal of support and assistance. I would like to take this opportunity to express my thanks to those who offered me help in various aspects.

I would first like to thank my supervisor Dr. Jun Tong for his valuable guidance, patience, and support. His insights for research always inspired me to solve the problem I met. I have learned a tremendous amount under his supervision. Also, I would like to express my sincere and deep gratitude to my co-supervisors, Professor Jiangtao Xi for his constant academic advice, suggestions and encouragement. My thanks also go to my co-supervisors, Professor Philip Ogunbona for broadening my horizons.

I truly appreciate my parents, my father Guoqiang Duan, mother Lixia Cheng for their love, support and understanding.

Many thanks to my colleagues and friends: Dr. Lei Lu, Xu Song, Tian Xie, Xu Zhang Ran Ji, Dr. Yuxi Ruan, Yiwen Mao, Yuewen Zhu. Meanwhile, I would like to give special thanks to Yiwei Zhang, Weimiao Yang and Miao Li for their company and support.

Last but never least I would like to thank all the staffs of the School of Electrical, Computer and Telecommunications Engineering for their help and cooperation.

# AUTHOR'S PUBLICATIONS

[1] **C. Duan**, J. Tong, L. Lu, J. Xi, Y. Yu and Q. Guo, "Improving the Performance of 3D Shape Measurement of Moving Objects by Fringe Projection and Data Fusion," *IEEE Access*, vol. 9, pp. 34682-34691, 2021

[2] **C. Duan**, J. Xi, J. Tong, Y. Zhang, Y. Yu and Q. Guo, "A data fusion approach to improving moving object measurement using phase-shifting profilometry," Proceedings of SPIE - The International Society for Optical Engineering, vol. 11732, pp. 1173208, 2021

[3] **C. Duan**, J. Tong, J. Xi, Y. Zhang, Y. Yu, Q. Guo and L. Lu, "A method for dynamic 3D shape measurements based on multiple-shot FTP and motion compensation," Proceedings of SPIE - The International Society for Optical Engineering, vol. 11205, pp. 1-7, 2019.

[4] **C. Duan**, Y. Zhang, J. Xi, J. Tong, Y. Yu and Q. Guo, "Fringe projection profilometry for the 3D shape measurement of objects with three-dimensional movements," *Proceedings of SPIE - The International Society for Optical Engineering*, vol. 11189, pp. 11890Z-1-11890Z-6, 2019.

[5] Y. Zhang, J. Tong, J. Xi, **C. Duan**, Y. Yu, Q. Guo and L. Lu, "A fringe projection profilometry scheme based on embedded speckle patterns and robust principal component analysis," Proceedings of SPIE - The International Society for Optical Engineering, vol. 11205, pp. 1-7, 2019.

[6] Y. Zhang, **C. Duan**, J. Xi, J. Tong, Y. Yu and Q. Guo, "A new method for fringe order error correction in fringe projection profilometry," Proceedings of SPIE - The International Society for Optical Engineering, vol. 11189, pp. 11890X-1-11890X-8, 2019.

[7] **C. Duan**, J. Tong, J. Xi, L. Lu, Y. Yu and Q. Guo, "A model fitting-based approach for measuring moving 3D objects using phase-shifting fringe projection" *Submitted*.

# TABLE OF CONTENTS

# LIST OF FIGURES

# LIST OF TABLES

# ACRONYMS

2D: two-dimensional

3D: three-dimensional

CMM: coordinate measuring machine

FPP: fringe projection profilometry

FTP: Fourier transform profilometry

GUI: graphical user interface

HVS: human visual system

ICP: iterative closest point

LS: least squares

MRC: maximum ratio combining

NMSE: normalized mean squared error

PSP: phase-shifting profilometry

RPCA: robust principal component analysis

SVD: singular value decomposition

TOF: time-of-flight

# Abstract

Three-dimensional (3D) shape measurement for object surface reconstruction has potential applications in many areas, such as security, manufacturing and entertainment. As an effective non-contact technique for 3D shape measurements, fringe projection profilometry (FPP) has attracted significant research interests because of its high measurement speed, high measurement accuracy and ease to implement. Conventional FPP analysis approaches are applicable to the calculation of phase differences for static objects. However, 3D shape measurement for dynamic objects remains a challenging task, although they are highly demanded in many applications.

The study of this thesis work aims to enhance the measurement accuracy of the FPP techniques for the 3D shape of objects subject to movement in the 3D space. The 3D movement of objects changes not only the position of the object but also the height information with respect to the measurement system, resulting in motion-induced errors with the use of existing FPP technology. The thesis presents the work conducted for solutions of this challenging problem.

Firstly, a model-fitting approach based on phase-shifting fringe projection is developed to extend the multi-shot FPP to objects with general 3D movements. A marker-free method based on the iterative closest point (ICP) algorithm is designed to estimate the movement parameters from initial estimates of the object shape. By establishing the correspondence among the object surface at different time instants, a new analytical model is developed to describe the multiple deformed fringe patterns as an explicit

function of the unknown object height. This model is then fitted to the actual measurements to retrieve the object height by solving an optimization problem.

Secondly, a data fusion approach is designed to enhance the performance of dynamic 3D shape reconstruction. During the movement of the dynamic object, the multiple height maps reconstructed by Fourier transform profilometry (FTP) at different time instants are first denoised individually. Then an adaptive fusion scheme is applied to suppress the errors in the coarse measurements, which exploits the correspondence among the height maps established by estimating the movement parameters and adaptive weights obtained by analyzing the measurements. This approach is also extended by applying phase-shifting profilometry (PSP) to retrieve the course height maps, which is more robust against errors.

Extensive simulation and experimental results are presented in the thesis to demonstrate the performance of the proposed approaches, which show that they provide effective solutions to extend FPP to objects subject to general 3D movements. Limitations of the proposed approaches are also analyzed and potential improvements are outlined.

# 1. INTRODUCTION

In recent years, three-dimensional (3D) shape measurement has become a highly demanded technology in many areas, such as biomedicine [1], entertainment [2,3], industrial monitoring [4], robot control [5], design and manufacturing [6,7]. Although various techniques have been developed, (e.g., time of flight (TOF) [8-12], laser scanner techniques [13-16], stereo vision [17-23], Moiré method [24-25] and structured light [26-33]), accurate and fast measurement of moving objects remains challenging tasks. This thesis aims to tackle the problems of profile measurement of moving objects using fringe projection profilometry (FPP).

This chapter introduces the background of the research problems and contributions. In the following, Section 1.1 gives an overview of 3D shape measurement techniques. Section 1.2 reviews fundamental FPP approaches. Section 1.3 discusses dynamic object measurement using FPP. Section 1.4 introduces the experiment setup and Section 1.5 summarizes the structure of this thesis.

## 1.1 Overview of 3D shape measurement techniques

Fig 1.1 shows the classifications of traditional 3D shape measurement techniques, which can be categorized into contact-based techniques and non-contact techniques. Contact-based techniques acquire the 3D information by physically touching the surface of objects with a probing device. Non-contact techniques include passive measurement techniques and active measurement techniques. Stereo vision is one of the commonly used passive techniques, which requires no additional light projected on the objects.

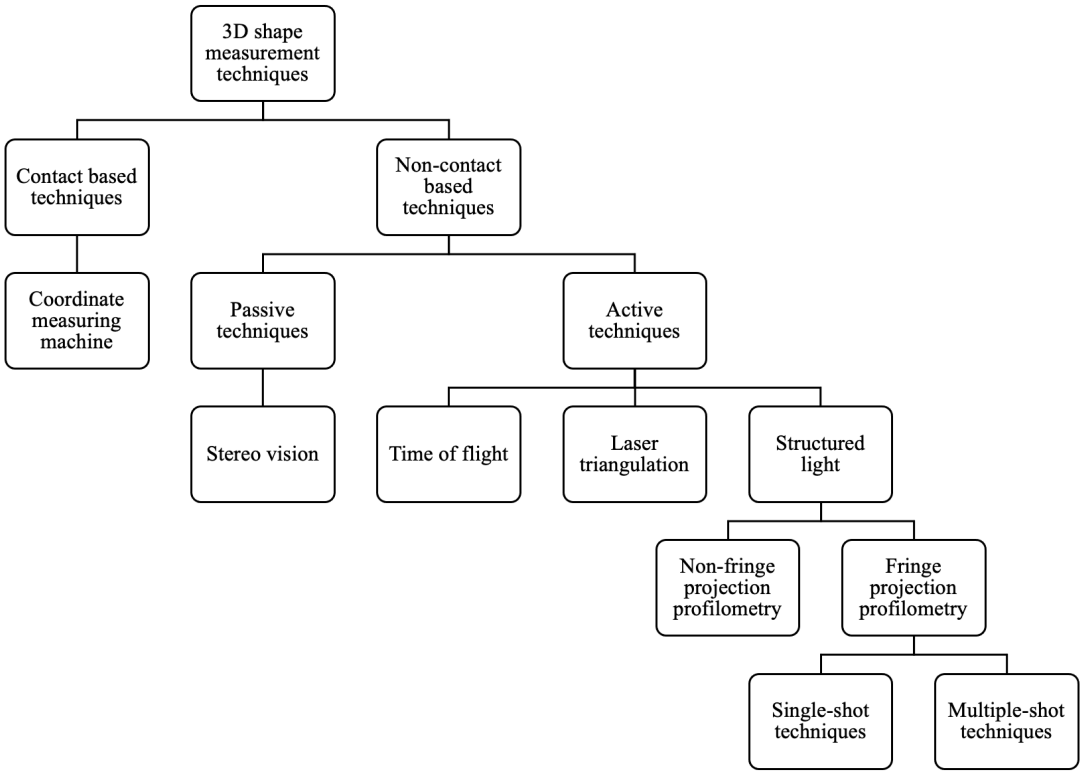


Fig. 1.1 Classifications of 3D shape measurement techniques

TOF techniques and structured light techniques are among the most used active techniques. The TOF techniques are based on the flight time of a laser or light beam between the object and the system to reconstruct objects. The structured light techniques project patterns on objects and use triangulation to retrieve the surface shape of objects, which can be further classified into fringe projection profilometry (FPP) and non-fringe projection profilometry according to the patterns applied. In general, FPP employs patterns with periodical fringes. Single-shot and multiple-shot FPP techniques differ in the number of patterns projected.

### 1.1.1 Contact-based techniques

Contact-based techniques need to touch the surface of the object to obtain the coordinates of all points on the object. The coordinate measuring machine (CMM) [34,35] is a widely

used contact-based measurement technique. The CMM is composed of the main body part, the probing detecting system, and the data collection component. The movement of the probe is controlled by the main body so that the probe can move freely to reach the whole surface of the object. The controlled probe contacts and slides on the surface of the object to collect the shape information on a point-by-point basis, and then these pointwise data are analyzed by the data collection component. Contact techniques are advantageous by high measurement accuracy but also suffer from obvious weaknesses. Firstly, it is time-consuming for the probe to slide on the object surface. Hence, they are not suitable for applications requiring real-time or fast measurement. Secondly, the direct contact between the probe and object limits the material and rigidity of the object. The damage on the object surface may happen for less rigid objects. Besides, the system is usually expensive in implementation and a sophisticated system calibration is required [36]. Finally, these techniques are not suitable for dynamic and large objects.

## 1.1.2 Non-contact techniques

Non-contact techniques can be classified into passive techniques and active techniques. Passive techniques reconstruct the object surface by analyzing the ambient light reflected from objects. For active techniques, light sources with intentionally designed patterns or beams are utilized to probe the object surface, which are deformed and reflected and acquired by a receiving device (e.g., a camera). 3D information is extracted by analyzing the received lights in combination with the probing ones and the geometrical structure of the measurement system.

### 1.1.2.1 Passive techniques

Stereo vision [17,22,37-39] is a typical passive technique that imitates the human visual system (HVS) by using two cameras. With stereo vision, two capturing cameras snap objects from two different perspectives. Different perspectives lead to the corresponding points of the object located at different positions in the captured images. The position difference is described as disparity [23]. The disparity map is obtained by calculating all the disparities between the two captured images. After generating the disparity map, calibration parameters of the stereo vision system are exploited to reconstruct the 3D shape of the object.

Nevertheless, detecting the corresponding points from two images and generating the disparity map require a high computation cost, and the task can be difficult to complete for the object with flat and non-texture areas. Besides, the same points on the object must be snapped simultaneously from two different angles, and the two angles of the cameras should keep some distance to guarantee a distinct disparity map. Therefore, the measurement scope and the shape of the object are highly restricted [39].

#### 1.1.2.2 Active techniques

In contrast to passive techniques, active techniques are usually less sensitive to the object texture and the effect of ambient light. With active techniques, encoded patterns or light beams are projected onto the object surface by means of a projector or a laser. The 3D shape of the object surface will result in distortion and delay on the reflection of the projected light beam or patterns, which are captured by the camera or sensor. By analyzing the difference between the cast pattern or light beam with the captured ones, the shape of the object can be reconstructed. Among other active techniques, TOF, laser triangulation and structured light are widely used, which are reviewed as follows.

## (1) TOF techniques

The time of flight (TOF) technique is inspired by the echolocation system of bats. Bats generate ultrasonic signals and receive the echoes to estimate the distance to a target. Similarly, a TOF system is composed of a light source and a sensor [40]. The light source emits the modulated light beam on the object surface, and the light sensor captures the reflected. According to the time interval between the sent and captured, the distance between the detector and the point on the object surface can be obtained. TOF techniques are typically classified into two categories: optical shutter techniques and intensity modulation techniques. While the time difference between sending and receiving is used to calculate the height information by optical shutter techniques, intensity modulation techniques [11] use phase difference between the lights sent and retrieved. Because the emitter and detector have the same viewing angle, the whole system is compact in its structure [41]. However, each individual point on the object surface is required to be measured separately, which limits the speed of reconstruction. Also, the TOF techniques are sensitive to noise and impairments of the system [8,9,42].

## (2) Laser triangulation

A laser triangulation system [43] consists of a laser source, a laser detector, and a lens. The laser source emits a beam or a line of light, casting on the object surface, which is reflected and captured by the detector. The light path from the source to the point on the target, and back to the detector form a triangle, which is used to obtain the 3D location of the point. To implement the measurement, calibration is required. The detector is normally a CCD array [44] or CMOS array [45], which is able to capture the whole scene. The laser triangulation technique achieves higher measurement resolution than TOF as it

is less sensitive to time. However, their pointwise or line-wise processing is not suitable for objects with large surfaces and objects subject to movement.

### (3) Structured light

Structured light techniques normally use a projector to cast a designed light pattern or onto the object surface for correspondence searching and phase difference analysis. A camera is triggered to capture the images reflected from the object surface, which are deformed by the shape of the surface. By analyzing the difference between the projected patterns and captured patterns, the 3D shape of the object can be extracted, also based on the triangular relationship. The principle for correspondence establishment is similar to the stereo vision system, but structured light techniques rely on the designed pattern rather than the texture feature of the object, and hence they are more reliable and robust in terms of measurements. Generally, structured light techniques can be classified according to the structure of the projected patterns. The most commonly used type of pattern is the one with straight stripes (fringes) across the pattern, and the techniques are referred to as fringe projection profilometry (FPP). Other light patterns can also be used, and the approaches are referred to as non-FPP.

- **Non-FPP techniques**

The non-FPP techniques utilize the distribution of dots in a 2D array to identify the position of each point on the images. 2D spatial coding techniques take advantage of windowed image processing [46]. Pseudo-random patterns, codewords-based mini-patterns, and color-coded patterns are three popular patterns for 2D spatial coding techniques. To guarantee the uniqueness of each dot within a sub-pattern, a pseudo-random binary array (PRBA) applies the marked dots to encode the position information. The displacement of marked dots is detected and then mapped to the height based on the

triangulation relationship. In contrast, a multivalued array [47] encodes the projected pattern by representing each pixel as a unique codeword. By analyzing the variation of codewords on the specific pixels, the shape of the object can be reconstructed. Another non-fringe technique is color-coded grid pattern, which utilizes the feature of color to guarantee the uniqueness of each pixel. All the mentioned non-FPP projection profilometry techniques are single-shot techniques, and thus the accuracy and resolution are limited.

- **FPP techniques**

Fringe-based techniques use fringe patterns to retrieve the height distribution of the object. Traditional fringe patterns can be classified into binary patterns, triangular patterns, trapezoidal patterns, saw-tooth patterns, and sinusoidal patterns. A projector is applied to create the designed fringe patterns and then cast onto the object. Nowadays, FPP is extensively applied for object surface reconstruction due to simple system structure and controllable fringe patterns. Besides, FPP can achieve high-resolution performance, fast measurement speed, and high accuracy results.

## 1.2. Literature review of fringe projection profilometry

A typical FPP system consists of a projector generating the fringe patterns and a camera capturing the patterns deformed by the object, as illustrated in Fig. 1.2. The distance between the lens of the projector and that of the camera is $d_0$ and the distance between the lens of the camera and the reference plane is $l_0$. Firstly, one or several fringe patterns are cast on a reference plane and captured by a camera. Then, the system projects the same fringe patterns on the object. By calculating the difference between the reference patterns and the deformed patterns, the height distribution of the object can be retrieved.

FPP techniques can also be categorized into single-shot and multiple-shot techniques according to the number of patterns projected.

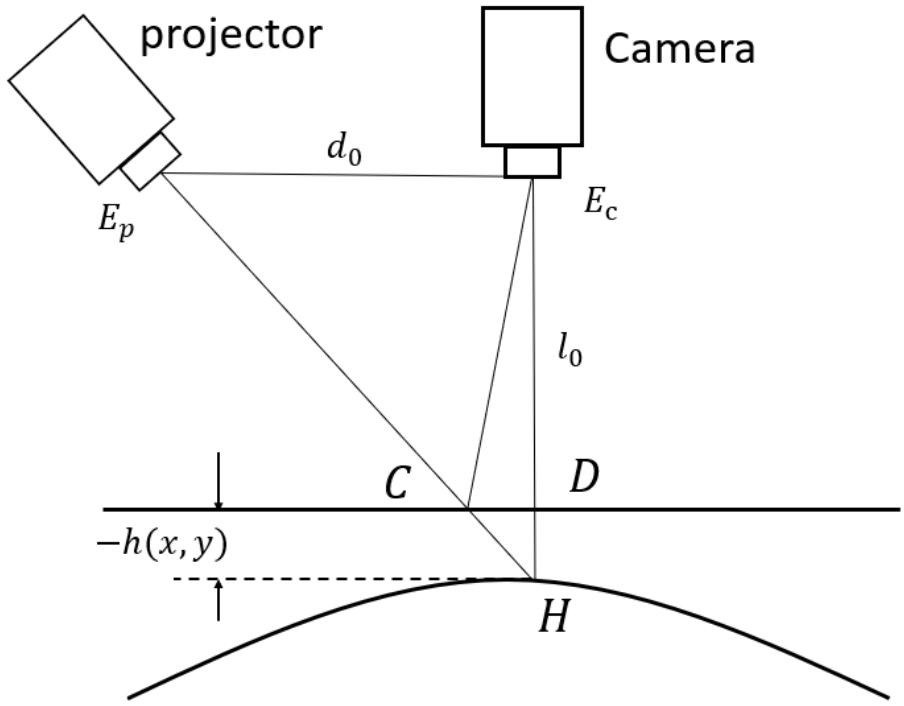


Fig. 1.2 FPP system model

## 1.2.1 Single-shot techniques

Single-shot techniques require the projection of only one fringe pattern to retrieve the height distribution of the object. Because the camera captures only one image, these techniques are suitable for real-time and fast object shape measurement. Nevertheless, single-shot techniques catch less information and may not guarantee a high accuracy due to the impact of background light and variations of the surface reflectivity.

### (a) Fourier transform profilometry (FTP)

FTP is one of the most widely studied single-shot techniques and was first proposed by Takeda *et al*. [48], which projects and captures only one sinusoidal fringe pattern on the object surface to reconstruct the object shape. The advantage of the sinusoidal pattern is that spectral analysis can be implemented easily. FTP adopts the Fourier transform to convert the fringe pattern from the spatial domain into the frequency domain. With the help of frequency analysis, the 3D shape of objects can be retrieved. Although the FTP algorithm is fast, the noise component mixed with the phase component is hard to be eliminated, resulting in low accuracy. Besides, the phase component and background component may overlap in the filtering process when the spatial frequency of the projected fringe pattern is relatively low and the shape of the object is relatively complex, which leads to reconstruction errors.

## (b) Techniques based on saw-tooth patterns

The saw-tooth technique employs saw-tooth fringe patterns to retrieve the object shape information, which is similar to the wrapped phase map from the sinusoidal pattern [49]. In contrast to FTP, the saw-tooth technique does not require the complex phase extract algorithm because the wrapped phase can be simply obtained by calculating the difference between the deformed saw-tooth map and the reference saw-tooth map. Then phase unwrapping algorithm is applied to find the absolute phase map. A triangular relationship among the projector, camera and object is used to convert phase map to height map. However, the influence from the ambient light and the reflectivity of the object surface degrades the accuracy of the reconstruction result.

## (c) Techniques based on color patterns

There are also techniques fusing multiple patterns in different colors into a single pattern [50-55]. Compared to the techniques with multiple projections and multiple acquisitions, such techniques require one pattern composed of three single-color patterns (red, green, and blue). A color projector and a three-channel camera are applied to cast and snap the multi-color fringe pattern. This camera can separate the red, green, and blue patterns by different colors, which have different frequencies. Simultaneously, the three patterns are phase-shifted. Analyzing the multiple patterns, the 3D shape of the object can be retrieved. With color patterns, objects can be reconstructed with higher accuracy than standard single-shot techniques. Nevertheless, the color camera increases the cost of the system. Meanwhile, the crosstalk phenomenon [56] happens between every two channels of the camera, which may degrade the accuracy of the reconstructed result.

### (d) Techniques based on frequency encoded patterns

Multiple fringe patterns, distinguished by their frequencies, can be superimposed. Each of the fringe pattern can be shifted in phase and then superimposed for measuring the object. The object-deformed fringe patterns of different frequencies can be separated in the frequency domain by bandpass filtering. This is followed by the typical phase-shifting algorithm to retrieve the phase. Separating the fringe patterns increases the complexity of computation [57], and a steep slope of the object may lead to spectrum overlapping in the frequency domain so that the reconstructed result is blurred.

## 1.2.2 Multiple-shot techniques

Multi-shot techniques generally improve the measurement accuracy at the cost of a longer measurement time. They require at least two fringe patterns (often three or more) to reconstruct the 3D shape of the object. Capturing multiple patterns increases the

information on the 3D shape of the object. Binary pattern [58-60], Gray-code pattern [61-64], intensity ratio method [65-71], speckle-embedded fringe patterns [72-74], and PSP [75-78] are typical multiple-shot techniques. These techniques are robust to the noise and object texture. However, multiple-shot techniques need to project and capture multiple patterns, which can be time-consuming. Besides, the object needs to keep stationary during the projection and acquisition. Otherwise, motion-induced errors will be introduced because of the loss of correspondence among the multiple captured patterns.

## (a) Techniques based on binary patterns

Binary patterns use only two illumination levels so that the projected patterns captured by a camera are presented as black and white stripes [58-60]. Meanwhile, a sequence of black and white stripes is projected on the reference plane to guarantee the uniqueness of each point. Normally, $K$ fringe patterns can encode $2^K$ unique stripes. Because the fringe patterns with extreme illumination levels are projected on each point, the binary encoded pattern is reliable and insensitive to the influence from ambient light and variation in reflectivity of the object surface. Thus, this technique is more robust than the non-binary techniques. However, the resolution of the reconstructed result is highly restricted by the number of projected patterns. Increasing the number of binary patterns can enhance the resolution, which also significantly increases the acquisition time. Therefore, techniques based on the binary pattern are not suitable for fast measurement or dynamic objects.

## (b) Techniques based on gray-level patterns

The use of gray-level patterns can decrease the number of projected fringe patterns. In contrast to binary patterns, the gray-level patterns employ multiple distinct levels of illumination to generate the unique coding of each point [61-64]. For example, the whole

illumination range can be divided into eight distinct levels, and $K$ fringe patterns can encode $8^K$ stripes, which effectively enhances the resolution of the measurement. The relatively small intensity interval between adjacent levels is easily influenced by the ambient light and variations in the reflectivity of the object surface.

## (c) Intensity ratio techniques

Intensity ratio techniques take full advantage of all intensity levels to measure the phase difference caused by the shape of the object [65-68]. The intensity values are integers that range from 0 to 255, so there are 256 levels of illumination, which is easier to specify the uniqueness of each point. The ramp intensity signal and uniform intensity signal are mixed to generate the intensity ratio patterns. The periodic ramp signal of intensity value increases from black to white across the whole image using the full range of intensity levels. The intensity differences between the adjacent points are the same, and the shape of the object can be extracted based on the triangulation [69,70]. The extensive range of illumination levels reduces the number of projected patterns and achieves a fast measurement speed. However, these techniques are sensitive to noise due to small intensity intervals. To separate the intensity between adjacent points, periodical patterns such as triangular patterns [67,68] and trapezoidal patterns [71] can be utilized. Even so, the ambiguity problem still appears due to the use of periodic patterns.

## (d) Techniques based on speckle-embedded fringe patterns

Speckle-embedded fringe patterns [72-74] fuse a pseudo-random speckle pattern and a fringe pattern into one pattern. After capturing a serial of composite patterns, the speckle component and fringe component are separated. The sinusoidal patterns are used to retrieve the wrapped phase map containing the height distribution of the object, which

applies the traditional phase retrieval algorithm. The speckle patterns from the composite patterns help determine the fringe order on each pixel for the phase unwrapping process. The fringe order on each pixel is determined by correlating the reference speckle pattern and a small area of the deformed speckle pattern. In general, the fringe order determination is highly influenced by the shape of the object. For example, a complex shape with a large slope may lead to the shadowing or overlapping of the speckle. Besides, the poor separation of patterns leads to poor reconstruction.

## (e) Phase-shifting profilometry

Phase-shifting profilometry is the most commonly used and extensively studied 3D shape reconstruction technique, which employs the sinusoidal fringe patterns to retrieve object height information [75-78]. Multiple equally phase-shifting patterns are projected and then captured by a camera. Using the feature of the phase-shifting fringe, the phase difference caused by the object can be retrieved. Meanwhile, the influence of background light and variation in the reflectivity of the object surface can be eliminated by jointly processing multiple patterns. Being robust against the noise and object texture, highly accurate results can be achieved. Because projecting and capturing multiple patterns are normally conducted at different times, the object must keep stationary during the projection and acquisition. Besides, the periodic patterns lead to the ambiguity of fringe order and phase unwrapping is required.

## (f) Techniques based on deep learning

Recently, deep learning has been used for 3D shape measurement based on FPP system due to its successes for computer vision and image processing [79]. Specifically, deep learning [80] can employ convolutional neural network (CNN) to automatically analyze

patterns from large amounts of historical information and then utilize the captured images to retrieve the height distribution of objects. The number of fringe order can be easily classified from the trained CNN duo to the limited number of label tag, and the edge of objects and systematic errors can be detected duo to the convolution kernel that extracts the edge and high frequency information from input image [81]. Besides, the CNN can predict the sub-component of traditional height retrieving algorithm to achieve higher measurement accuracy [82]. While the large computation time for training data and the massive training data set are required, which askes for tremendous training resource related to both expenses cost and time cost.

# 1.3. Dynamic object measurement using FPP

## 1.3.1 Challenges for dynamic object measurement

The PSP algorithm takes advantage of multiple patterns to achieve high spatial resolution and high measurement accuracy. However, the conventional PSP requires static objects, as the motion of the objects can significantly degrade the performance due to the loss of the correspondence of the points. A static object keeps the object height distribution invariant during the projection and acquisition of images so that the pixels containing the same height information are held in the same position among the captured images. This, however, is no longer the case when the object moves because not only the position of the dynamic object can change, but also the height value of the same point on the object can vary due to the 3D movement of the object. The variation of the position and height value is reflected in the phase values on multiple captured images. The phase variation violates the static assumption of the PSP algorithm. Hence, the traditional PSP algorithm may fail to reconstruct dynamic object surfaces

Compared with PSP, FTP projects only one pattern to reconstruct the 3D shape of the object. When the object is moving during the acquisition process, one shot of the pattern is adequate to retrieve all height information of the object. Therefore, the motion-induced errors have less effect on the phase retrieving process. However, FTP still has several disadvantages for dynamic object measurement. Firstly, the measurement accuracy for dynamic objects is limited due to its single-shot nature. Consequently, once the object phase information is blurred or missed, the relevant shape cannot be retrieved. Besides, the ambient light and variation in the reflectivity of the object surface are hard to be removed with only one pattern. In the frequency domain, the first sidelobe contains the object height information, and this fundamental component should be separated from other spectra, which leads to the limitation of the slope on the object surface. Aliasing between the spectra will affect the extraction of fringe pattern components and fail FTP reconstruction.

### 1.3.2 Existing FPP techniques for dynamic shape measurements

As discussed above, the FTP approach is a feasible solution for dynamic objects due to its single-shot nature. However, the measurement accuracy of FTP is low. On the contrary, high accuracy reconstruction may be achieved by multiple-shot PSP techniques, but they can suffer from motion-induced errors. In order to address the challenges for dynamic object measurement as presented in Section 1.3.1, the PSP and FTP techniques have been modified from different aspects. Related works for dynamic object measurement are reviewed below.

#### (1) Modified PSP for the measurement of dynamic objects

Several modified PSP approaches have been proposed for measuring dynamic objects. According to the targeted movement trajectory, we classify the existing approaches into the following categories.

## (i) Modified PSP for dynamic objects with 1D movement

Let us consider that the object moves in a one-dimensional (1D) space, i.e., along a straight line. In this case, every part of the object undergoes the same motion. This case is normally observed in the factory inspection process, where the objects are placed on the pipeline and they are moving along the movement trajectory of the pipeline. The FPP system is set over the pipeline, which is treated as the reference plane. During the delivery of the objects, their shapes are inspected.

Weise, *et al.* [83] proposed a method that combines the phase-shifting technique and stereo vision technique to compensate for the motion-induced errors. The phase-shifting processing aims to remove the influence from ambient light and reflectivity of the object surface, and stereo vision processing aims to solve the discontinuity problem on the object surface. When the movement trajectory of objects is 1D, there is a position shift of the corresponding point among capture images. This shift leads to ripple errors in the reconstruction results [88]. Then, the traditional PSP is modified to compensate for the errors by taking the shift caused phase difference into consideration. After that, stereo vision contributes to the fringe order determination for phase unwrapping, which addresses the discontinuities problem on moving artifacts. However, this technique needs three cameras to capture phase-shifting patterns and stereo vision patterns and assumes dynamic objects moving in one direction at a constant speed.

Yoneyama, *et al.* [84] also considered objects with 1D movements at a constant speed. A single fixed sinusoidal fringe pattern is cast on the dynamic object. During the movement of the object, cameras with linear array sensors are applied to detect the trajectory of the object and capture the deformed fringe pattern caused by the object. Because the movement direction and speed of the objects are known, the object can be captured at specific positions that can guarantee that the object induces the same phase shifts in the captured images. Using the deformed phase-shifting patterns, the height distribution of the object is reconstructed by the traditional PSP algorithm. In this method, there is no need for any phase-shifting process, and the algorithm for phase retrieval is simple. However, the movement speed needs be constant and known, which seems impractical in some real-world measurements.

Cao, *et al.* [85] proposed a PSP algorithm based on the orthogonal two-frequency fringe patterns to reconstruct the 3D shape of objects with 1D movements. The orthogonal fringe pattern is composed of a low-frequency pattern and a high-frequency pattern. During the movement of the target object, a series of orthogonal two-frequency fringe patterns are projected on the object and then captured. To separate the low-frequency fringe components and high-frequency components, a 2D window filter is employed to avoid the aliasing phenomenon in spectrum separation. The separated high-frequency fringe components are used to match the corresponding points of captured patterns, and the low-frequency fringe components are applied to retrieve the height distribution and alleviate the error from the phase unwrapping process. However, the movement of the object is highly restricted by 1D movement, which allows the object to move along only one specific direction.

A method based on PSP with unequal phase shifting is proposed by Li, *et al.* [86]. A fixed fringe pattern is projected on the dynamic object. The dynamic object moves along the

perpendicular direction of the fringe and a camera is used to capture the object. The fringe patterns captured from the dynamic object have phase shifts similar to those in standard PSP for static objects. The dynamic object may be captured by the camera at any time, so the shifting phase is unequal on the object. To determine the unequal phase shifting, FTP is employed to extract the edge of the dynamic object for matching the corresponding pixels among multiple captured images. This method extends the traditional PSP algorithm for the equal phase-shifting situation to the unequal phase-shifting situation. However, the 1D movement still limits the movement of the dynamic object.

Wang, *et al.* [87] proposed a PSP approach combined with a temporal phase unwrapping algorithm to reconstruct the dynamic object with a constant speed. In order to eliminate this motion-induced error, a modified PSP with six phase-shifting patterns is applied to enhance the measurement accuracy. At first, the displacement of the object among captured patterns is calculated based on the centroid of the dynamic object. This is then used to calculate the phase offsets on multiple fringe patterns. Third, a series of the designed fringe patterns are regenerated and projected on the object. After that, the patterns deformed by the object are captured by the camera to calculate the wrapped phase distribution. At last, the unwrapped phase map is obtained. This approach alleviates the motion-induced error from the dynamic object and takes advantage of high accuracy from PSP. Besides, the temporal phase unwrapping improves the robustness of fringe order determination. Nevertheless, the movement of the object is highly restricted, which requires the fixed movement trajectory and constant speed of the object.

### (ii) Modified PSP for dynamic objects with 2D movement

With 2D movements, the object can move freely in a flat plane. The 2D movement can be decomposed into rotation and translation. Rotation means every part of the object

moves in a circle covering the same rotating angle regarding the center point of objects, and the translation means every part of objects moves by the same amount with the same direction and distance. Meanwhile, dynamic objects with 2D movements are more common than 1D movement, which has wider applications. We classify the modified PSP into two categories, according to whether the motion parameters are explicitly estimated for compensating the motion-induced errors.

- **Direct compensation of the motion-induced errors**

We first summarize techniques that do not require explicit estimation of the motion parameters. Cong, *et al.* [88] investigated a Fourier-assisted PSP algorithm for dynamic objects. This algorithm utilizes the FTP to compensate for the errors for PSP. Each step of the phase-shifted fringe pattern is processed by FTP to obtain the phase map, so the motion-induced phase difference on the object can be estimated by analyzing the phase maps. After that, the traditional PSP is modified to retrieve the phase distribution of the object by taking the motion-induced phase difference into consideration. Besides, the maker-based phase unwrapping method is introduced to enhance the performance of dynamic object reconstruction. However, the system parameters are fixed empirically, which may not perform well when the objects are different.

In [89], Feng, *et al.* observed and summarized three types of artifacts caused by motion-induced errors. Motion ripples are ripple errors on the retrieved object surface, which are introduced by the variation of the dynamic object. Motion outlier errors are impulsive errors at the boundaries of moving objects and texture edges. Besides, the phase unwrapping errors are caused by the motion-induced error of the fringe order. In order to combat these artifacts, a motion compensation approach is proposed. The motion-induced phase shifts are initially estimated by comparing the three captured images. When the

objects have a constant speed, the motion-induced phase shifts between the first and second images as well as the second and third images can be initially estimated. Then, the least-square algorithm is applied to iteratively refine and correct the initially estimated phase shifts. To eliminate the outliers, the reference phase map is employed to compensate for the phase map that contains the object phase information. Then, the reliable pixels around the pixels with erroneous fringe order are detected by estimating the gradient, which are used to obtain the correct fringe order for phase unwrapping. This approach only works for objects with a constant moving speed, which limits the application.

In [90], Liu, *et al.* compensated the motion-induced errors by applying the pin-hole model. The pin-hole model describes the relationship between the 3D coordinate and the 2D projector and camera coordinate. By comparing the phase difference of corresponding points on the projector and camera coordinates, the motion of objects in 3D world coordinates can be estimated. After that, the motion of objects is converted to phase-shifting errors and then applied for the modified PSP to compute the new phase information of objects. Because this method treats each point independently, reconstruction quality for both rigid and non-rigid objects can be improved. However, the system is only suitable for objects with slow movement where the phase-shifting errors are within a fringe period.

Duan, *et al.* [91] proposed a novel approach for objects with arbitrary 2D movements by applying composited fence images and fringe images. The 2D movement of objects can be described as the rotation and translation of objects on a plane. In this approach, designed markers with vertical fences and horizontal fences are utilized to track the moving trajectory of dynamic objects among each PSP step. First, the cropped fence images are binarized, by which the rotation angles can be calculated by the *Hough*

*transform algorithm*. Then, translation distances along row and column directions are detected by the 1D hybrid phase correlation method. Third, the transformation parameters are applied to the reference phase map for compensating for the motion-induced errors. However, large-scale movement leads to the failure of rotation angle and translation displacement extraction, and the movement of objects is still limited to 2D movements.

Liu, *et al.* [92] proposed a method compensating the motion-induced errors by estimating the unknown phase shifting. In contrast to the static object, the varying position of the object among captured images results in unknown additional phase shifts. To determine the unknown shifts pixel by pixel, three successive captured images are combined to estimate the motion-induced errors. Because the object trajectory is unknown and the motion-induced errors change during acquisition, the object at the first position with no motion-induced error can be regarded as the reference to determinate the phase-shifting errors in the following captured images. Then, a phase map of the object without a motion artifact can be retrieved. To meet the requirement of real-time measurement, the phase ambiguity problem of the wrapped phase map is solved by the system geometry constraints. This method can be utilized for objects with non-homogeneous and significant motion but still targets 2D movement.

- **Motion parameter retrieval-aided compensation of the motion-induced errors**

There are also schemes that first estimate the motion parameters and then apply the movement model to compensate for the effect of motion-induced errors. Lu, *et al.* [93] addressed the reconstruction of the dynamic object with 2D movements by placing markers on the object surface to calculate the rotation matrix and the translation vector. With the established movement trajectory, the correspondences of the points on the object

among different captured images are established. Then the PSP is modified by generating a new reference phase map to retrieve the phase information. Lu, *et al.* [94] proposed an automatic approach to reconstruct 3D shapes for objects with 2D movements. Similar to [93], the rotation matrix and translation vector are also estimated to describe the movement of the object. In contrast to the markers-based approach, the SIFT algorithm is exploited to track the object. After obtaining the movement parameters, the correct phase value caused by object height is retrieved by the LS algorithm. This method addressed motion-induced errors. Besides, human intervention for the motion parameters extraction can be removed, and automatic measurements are thus possible. However, these methods are still limited to 2D movements.

### (iii) Modified PSP for dynamic objects with 3D movement

2D movement of objects limits the object to move on the reference plane, and the compensation of errors caused by the variation of position may be adequate to reconstruct the surface of the dynamic object. When 3D movement is introduced, the variation of height distribution also occurs, which adds significant challenges for retrieving the phase. There are fewer studies aiming to address such challenges.

Zhang and Yau [95] proposed a two-plus-one phase-shifting algorithm to measure the 3D shape of the object with 3D movements. In this method, two sinusoidal patterns with $\pi$ phase-shifting and a uniform flat pattern are used. All three patterns are combined to retrieve one phase map. Two phase-shifted sinusoidal patterns provide reference phase information and the object height information, and the uniform flat pattern captures the object texture information rather than object height information. The uniform flat pattern assists the fringe pattern to eliminate the background light and then the two fringe patterns can retrieve the object phase information. Due to the reduced patterns used for height

retrieved, the motion-induced errors have less effect on the reconstruction result than traditional PSP. At the same time, the resolution of the two-plus-one method can achieve the same level of PSP due to the elimination of background light and the reflectivity of the object surface. Though performance can be improved to some extent, the motion-induced errors between the two $\pi$ phase-shifted patterns can not be and still blur the reconstruction result.

Lu. *et al* extended their method from the 2D movement of the object to 3D movement in [96], where the 3D movement changes not only the position of the object but also the height information. Similar to [93], the rotation matrix and translation vector are also introduced to model the movement of the object, but they are extended from the 2D format to 3D, which also accounts for the height variation. First, the captured fringe patterns are rewritten as a new model by replacing the original reference phase map with an imaginary phase map. Then an iterative least-squares (LS) algorithm is performed to retrieve the phase difference caused by the object height information and compensate for the height variation errors from 3D movement. This method could estimate the correct object height distribution without knowing the height variation of the object, which converts the 3D movement model to the 2D movement model with extra phase variation. However, the height variation of the object is highly restricted, which only allows the translation in the direction of height rather than free 3D movement.

## (2) FTP-based techniques for dynamic object measurements

In contrast to the PSP techniques, the FTP techniques can retrieve the object surface from one captured image, and so it is not sensitive to the movement trajectory of objects. However, its accuracy is limited. To address this problem, FTP has been modified in several different ways, which may enhance dynamic object reconstruction.

### (i) Modified FTP with multiple shots

The measurement accuracy of the single-shot FTP method can be improved by increasing the number of the projected fringe patterns. Thus, the $\pi$ phase-shifting approach (IFTP) based on traditional FTP is proposed by Li, *et al.* [97]. An ordinary sinusoidal fringe pattern and a $\pi$ phase-shifted fringe pattern are projected and captured by a camera. During the movement of the object, two successive patterns are captured by the camera. By subtracting the two captured patterns, the zero-frequency component in the spectral domain is eliminated, which mitigates the frequency aliasing problem between adjacent frequency components. This method improves the measurable slope of the height variation on the object surface by around three times with the same system parameters. Meanwhile, the accuracy is better than that of conventional FTP by eliminating the background light. However, this method is not suitable for dynamic objects with large-scale movement.

The $\pi$ phase-shifting FTP approach was extended to measure the moving objects with constant speeds by Hu, *et al.* [98]. They propose to project only one sinusoidal pattern on the reference plane. Two regions are detected and captured by two line-scan cameras when the moving object is sliding in. The object will be captured twice from two cameras at the same time. The experiment system should be calibrated by the digital correlation method to guarantee the two fringe patterns on the object with $\pi$ phase-shifting and calculate the coordinate difference between two patterns. After obtaining the two phase-shifting patterns with known differences, the IFTP algorithm in [97] is employed to reconstruct the dynamic object. The accuracy of the reconstruction result is significantly enhanced. However, the high cost of line-scan cameras increases the difficulty of implementation.

Su, *et al.* [99] developed a new FTP-based algorithm to reconstruct the dynamic object. After using Fourier transform algorithm, filtering process, and inverse Fourier transform algorithm, a sequence of wrapped phase maps can be calculated. By combining the current time instant and the neighboring time instant, the phase difference between these two instants can be retrieved. In order to unwrap the phase map for the dynamic object, the 3D phase unwrapping algorithm is proposed. In this approach, only one reliable unwrapped phase map is required, and this unwrapped phase map can be obtained by a general spatial unwrapping algorithm. Then, the phase difference between the adjacent instants can be added to the original unwrapped phase map, so the absolute phase of the object in the next instant can be measured easily. Even the simple acquisition system and fewer phase unwrapping errors are the advantage of the method, the overlapping of the spectra influences the reconstructed result.

### (ii) Modified FTP with single shot

Even the modified FTP with multiple shots can improve the performance of the dynamic object reconstruction by receiving more information, the motion-induced errors may be introduced at the same time. Instead of employing extra fringe projections, single-shot FTP may be improved by using more advanced phase retrieval algorithms.

Two-dimensional FTP is proposed by Lin, *et al.* [100], which operates the fringe pattern from a two-dimensional perspective rather than one-dimensional. The captured deformed fringe pattern is converted from the spatial domain into the frequency domain by the 2D fast Fourier transform (FFT) algorithm, and the object-contained frequency component is extracted by the 2D Hanning window, then the filtered component is transformed by 2D IFFT to obtain the wrapped phase map. 2D FTP provides a clearer separation of the object-contained component from the background noise, so the measurement accuracy is

improved. Besides, the 2D phase unwrapping is more reliable with fewer fringe order errors. However, the reconstruction result is still influenced by the reflectivity of the object surface.

### 1.3.3 Outstanding issues and contributions

#### (1) Outstanding problems

From the discussion above, FPP has great potential for fast reconstruction, high accuracy, and dense resolution for measuring 3D shapes. Although several techniques have been developed for measuring moving objects with special forms of movement, it is still challenging to obtain high accuracy reconstruction of objects with general 3D movement using low-cost devices. The FTP approach employs a single fringe pattern. It is thus less sensitive to motion-induced errors, but the reconstruction result suffers from accuracy degradation due to such factors as ambient light, reflectivity variations on the object surface, and noise owing to its single-shot nature of FTP. For multi-shot techniques, the existing PSP solutions cannot eliminate the motion-induced errors when free 3D movement is present. In light of the above, we can identify the following outstanding problems for dynamic object measurement:

- For rigid objects with general 3D movements, when multiple fringe patterns are projected, the correspondence of the captured fringe patterns is lost as the position of the object changes. This together with the phase change due to height variation can significantly degrade the measurement performance. Is it possible to track the 3D movement of the dynamic object among the captured patterns to enable further processing?

- The motion-induced errors will be introduced in fringe patterns while applying the PSP techniques to moving objects. How do the motion-induced errors from general 3D movement influence the fringe patterns and how can these errors be described and compensated?
- The FTP is limited by its one-shot nature. Is it possible to enhance the performance of single FTP results and combine multiple FTP results to further improve the performance for dynamic object reconstruction?

## (2) Contributions

This thesis addresses the above outstanding problems for dynamic 3D shape measurements. The influence of object movement on the performance of FPP systems is examined. We focus on multiple-shot techniques (multiple-shot FTP or PSP) for achieving robust performance against background light and variations of reflectivity on the object surface. To eliminate the motion-induced errors, we make the following contributions in this thesis:

- We develop a marker-free, ICP-based method for estimating the motion parameters for rigid objects with free 3D movement, which can be well integrated into the standard FPP systems;
- We analyze the captured fringe patterns by taking the free 3D movement into consideration and develop a model-fitting approach to retrieve the object height distribution from multiple fringe patterns;
- We improve the FTP-based dynamic object measurement by alleviating the noise and fusing multiple FTP results and extend the approach to the PSP technique;
- Through numerous simulation and experimental studies, we demonstrate the performance of the proposed approaches.

## 1.4 Experiment setup

To achieve high-accuracy measurement for the dynamic object with low hardware cost and an easy-to-setup system, the experiment system for this thesis is based on the traditional FPP system, which contains a single camera and single projector. Fig.1.3 shows the photo of the system setup. The distances between the camera lens, projector, and target object on the reference plane are adjustable. This flexible system can meet the requirement of objects with different sizes, shapes, and movement states.

### 1.4.1 Projection and Acquisition

A color digital projector BENQ w1090 is employed, which is connected to the computer over a High-Definition Multimedia Interface (HDMI) port. The display gamma parameter, brightness, focus, and contrast for the RBG channels are tuned. A high-resolution IMAVISION MER-1070-10GM camera is applied to acquire the images, which is connected to the computer via a Gigabit Ethernet port. The camera has three individual RGB channels with the highest resolution of 3840×2748.

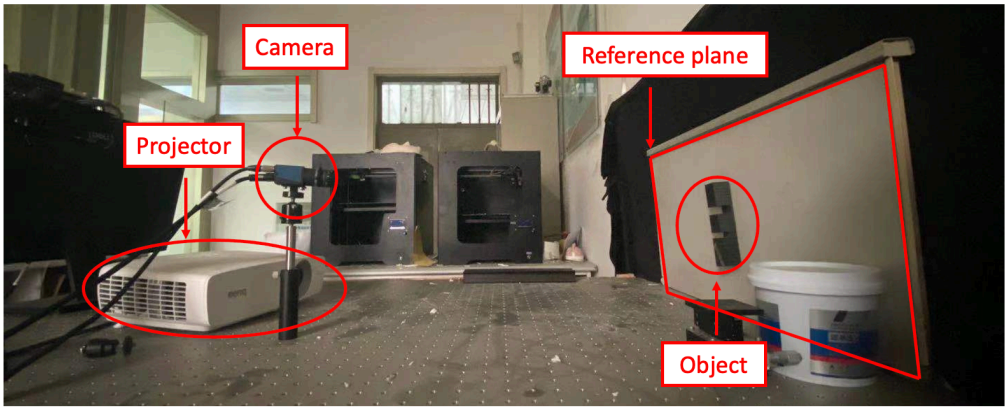


Fig. 1.3 The experiment system setup

## 1.4.2 Software Interface

A MATLAB Graphical User Interface (GUI) is designed to integrate hardware components, generate and control the fringe projection. The frequency and initial phase of the fringe patterns can be controlled digitally. Under the control of GUI, the final fringe pattern is presented as shown in Fig.1.4.

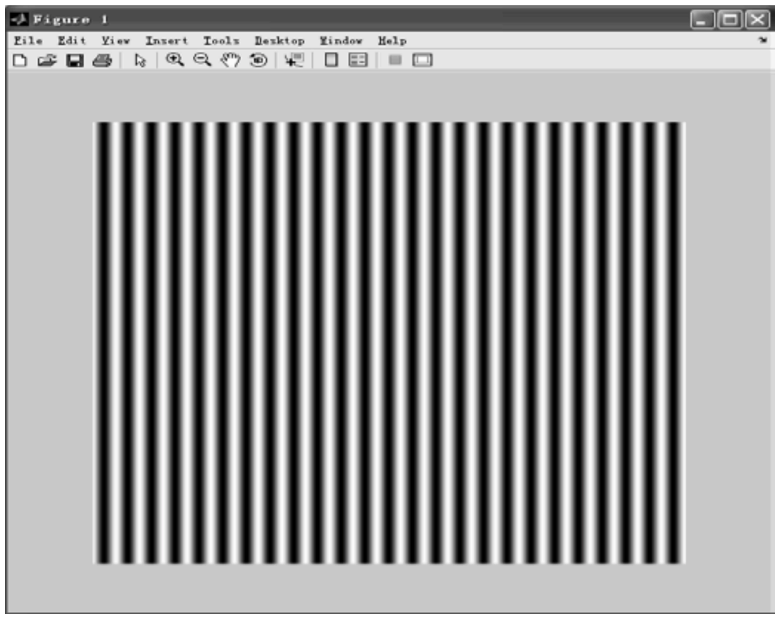


Fig. 1.4 Fringe produced

## 1.4.3 Processing of the Image projection and acquisition

In the experiment, the FPP system needs to capture two sets of images to reconstruct the object surface: one fringe pattern set on the reference plane only and one deformed pattern set on the object surface. For example, a mask shape is placed on the reference plane as the target object. Fig.1.5 shows two fringe patterns with and without the object. The projection and acquisition of the images use the following system setup. The camera is placed beyond the projector at a distance of 180mm. The distance between the lens of the camera and the reference plane is 725mm. The camera with a resolution of 1,900 × 1,600

pixels captures the field of vision with 400mm×200mm. Consequently, the equivalent spatial resolution is around 0.18 mm/pixel. This system is employed to implement the experiments in this thesis.

(a)

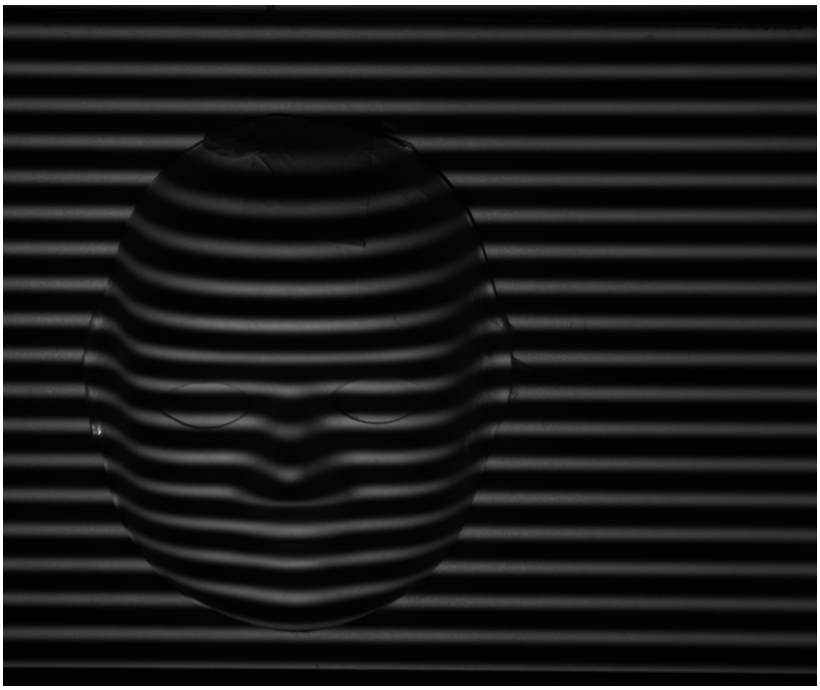

(b)

Fig. 1.5 Captured images from a reference plane (a) and object surface (b)

## 1.5 Structure of this thesis

The structure of this thesis is organized as below:

- Chapter 2 proposes a model fitting-based approach based on an iterative closest point algorithm (ICP) to compensate for the motion-induced errors for objects with 3D movements. By considering the movement information of the object, a new model of the fringe pattern that accounts for object movement is derived. Instead of retrieving the phase value by the PSP algorithm, the proposed method extracts the height information directly by fitting the model to the captured fringe images. The model-fitting problem can be solved by an exhaustive search over a range of height values. In order to reduce the computational complexity, an initial estimate of height value is obtained first. FTP algorithm is applied to retrieve the coarse height map of the objects, which provides the initial height values to search the real height for each point. In the meanwhile, the coarse height maps retrieved by FTP are utilized to extract movement parameters using the ICP algorithm. Simulations are performed to verify the feasibility.
- In Chapter 3, a new approach based on data fusion is proposed to improve the reconstruction result for rigid objects with 3D movements. By utilizing the knowledge of the motion parameters, multiple height maps are retrieved from several FTP measurements and then combined after compensating the motion effect. The proposed method suppresses the influence due to the ambient lights and reflectivity. To further improve the performance of the fusion method and estimation of motion

parameters, the RPCA algorithm is applied to eliminate impulsive errors and random, unstructured errors. Besides, error-suppressed height maps are then applied to estimate the motion parameters by ICP. Then, multiple height maps are fused using estimated motion parameters and weights adapted to the quality of captured fringe patterns. This method is extended to be combined with 3-step PSP to improve the performance. Simulations and experiments verify the effectiveness of the proposed schemes.

- To complete this thesis, Chapter 4 summarizes the findings and discusses the directions of future research.

# 2. MODEL FITTING-BASED RECONSTRUCTION OF DYNAMIC OBJECTS WITH 3D MOVEMENT

## 2.1 Introduction

Among the various fringe projection techniques (FPP) techniques for object surface reconstruction, PSP has attracted significant research interests. Thanks to its multi-shot nature, PSP is less sensitive to ambient light and reflectivity on the object surface. For static objects, the performance of PSP can be improved by projecting and capturing more phase-shifted fringe patterns. When the object moves, however, the movement may lead to significant degradation of the performance of the PSP due to the loss of correspondence. In order to address this challenge, the object motion may be tracked and used to compensate for the motion-induced phase errors. However, the existing approaches are only valid for objects with 1D, 2D and specific 3D movement, which is not the case of general 3D movements. Therefore, it is highly exigent to develop new approaches for measuring objects with general 3D movements using a simple FPP system.

This chapter proposes a novel approach to enhance the performance of 3D shape measurements using phase-shifting fringe projections. We consider rigid objects with 3D movements, which can be modeled by 3D rotation matrices and 3D translation vectors. The motion-induced position changes and phase shifts are integrated into the analysis of the deformed fringe patterns. Based on this, a model-fitting approach is developed to retrieve the height profile. In contrast to existing solutions for measuring moving objects, the proposed approach allows general 3D motion and employs marker-free estimation of

the motion parameters. The simulation results indicate that the proposed approach can achieve higher accuracy than the traditional FTP and PSP approaches for moving objects.

This chapter is organized as follows. Section 2.2 introduces the system model and formulates the problem. Section 2.3 details the proposed model fitting-based method. Section 2.4 evaluates the proposed method using simulations. Finally, Section 2.5 summarizes the findings.

## 2.2 Problem formulation

Let us consider the measurement of the 3D shape of a rigid object. Suppose a set of $K$ phase-shifting sinusoidal patterns with spatial frequency $f_0$ are projected at $K$ time instants. When the object is static, the fringe patterns captured respectively from the reference plane and the object can be written as:

$$s_k(x,y) = a_k(x,y) + b_k(x,y)cos\left(\varphi(x,y) + \frac{2\pi(k-1)}{K}\right),\ k = 1,2,\dots,K, \quad (2.1)$$

*and*

$$d_k(x,y) = a_k(x,y) + b_k(x,y)\,cos\left(\varphi(x,y) + \Phi_h(x,y) + \frac{2\pi(k-1)}{K}\right), k = 1,2,\dots,K, \quad (2.2)$$

where $a_k(x,y)$ is the average intensity and $b_k(x,y)$ is the intensity modulation of sinusoidal fringe patterns. Generally, $a_k(x,y)$ and $b_k(x,y)$ can be assumed constant over time. The PSP algorithm can eliminate the influence from $a_k(x,y)$ and $b_k(x,y)$ and then retrieve the height information wrapped in the phase $\Phi_h(x,y)$.

When the object moves during the $K$ time instants, both the position and height of the object surface can change, which results in deformed patterns different from (2.2). In such cases, the traditional PSP algorithm fails to extract the required phase $\Phi_h(x,y)$. Let the

3D coordinates of a point $P$ on the dynamic object surface at time instant $k$ be $(x_k, y_k, h_k)$, where $(x_k, y_k)$ defines the position on the X-Y plane and $h_k$ the corresponding height. The coordinates of the point $P$ measured at time instant $k$ can be modelled as:

$$\begin{bmatrix} x_k \\ y_k \\ h_k \end{bmatrix} = \boldsymbol{R}_k \begin{bmatrix} x_1 \\ y_1 \\ h_1 \end{bmatrix} + \boldsymbol{t}_k, \tag{2.3}$$

where $\boldsymbol{R}_k$ and $\boldsymbol{t}_k$ are the rotation matrix and translation vector relative to time instant 1, respectively, given by

$$\boldsymbol{R}_k = \begin{bmatrix} r_k^{11} & r_k^{12} & r_k^{13} \\ r_k^{21} & r_k^{22} & r_k^{23} \\ r_k^{31} & r_k^{32} & r_k^{33} \end{bmatrix}, \tag{2.4}$$

$$\boldsymbol{t}_k = \begin{bmatrix} t_k^1 \\ t_k^2 \\ t_k^3 \end{bmatrix}. \tag{2.5}$$

For general 3D movements, the transformation in (2.3) contains six degrees of freedom (6 DOF), including three for rotation and three for translation. Let us temporally drop the index $k$ for notational simplicity. The rotations matrix $\boldsymbol{R}$ can be parameterized by three rotation angles $\alpha$, $\beta$ and $\theta$ for the X, Y and Z axis respectively, as illustrated in Fig. 2.1.

The mutually orthogonal rotation matrices with respect to the three directions are given as

$$\boldsymbol{R}_x(\alpha) = \begin{bmatrix} 1 & 0 & 0 \\ 0 & \cos(\alpha) & -\sin(\alpha) \\ 0 & \sin(\alpha) & \cos(\alpha) \end{bmatrix} \tag{2.6}$$

$$\boldsymbol{R}_y(\beta) = \begin{bmatrix} \cos(\beta) & 0 & \sin(\beta) \\ 0 & 1 & 0 \\ -\sin(\beta) & 0 & \cos(\beta) \end{bmatrix} \tag{2.7}$$

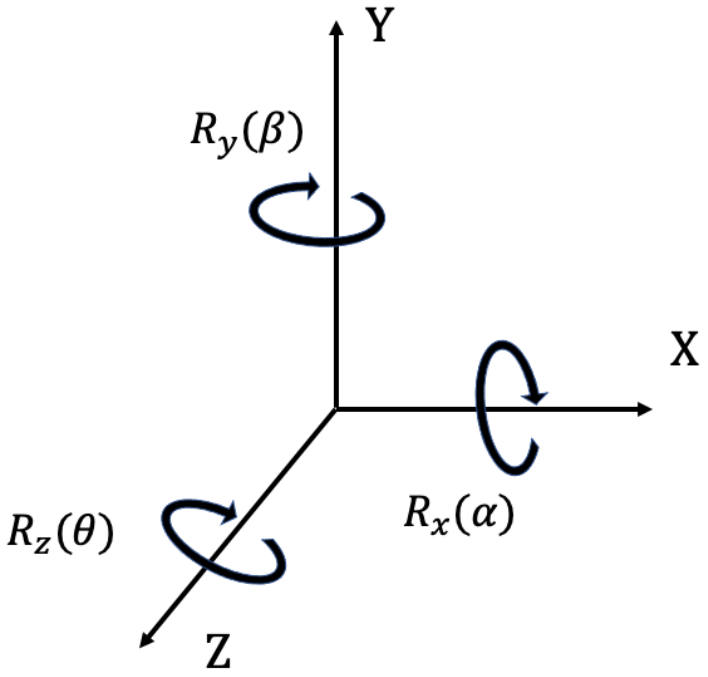


Fig. 2.1 Rotation matrices

$$\boldsymbol{R}_z(\theta) = \begin{bmatrix} \cos(\theta) & -\sin(\theta) & 0 \\ \sin(\theta) & \cos(\theta) & 0 \\ 0 & 0 & 1 \end{bmatrix} \tag{2.8}$$

The overall rotation matrix is computed as:

$$\boldsymbol{R} = \boldsymbol{R}_z(\theta)\boldsymbol{R}_y(\beta)\boldsymbol{R}_x(\alpha) \tag{2.9}$$

$$\boldsymbol{R} = \begin{bmatrix} \cos(\theta) & -\sin(\theta) & 0 \\ \sin(\theta) & \cos(\theta) & 0 \\ 0 & 0 & 1 \end{bmatrix} \begin{bmatrix} \cos(\beta) & 0 & \sin(\beta) \\ 0 & 1 & 0 \\ -\sin(\beta) & 0 & \cos(\beta) \end{bmatrix} \begin{bmatrix} 1 & 0 & 0 \\ 0 & \cos(\alpha) & -\sin(\alpha) \\ 0 & \sin(\alpha) & \cos(\alpha) \end{bmatrix} \tag{2.10}$$

$$\boldsymbol{R} = \begin{bmatrix} \cos(\theta)\cos(\beta) & \cos(\theta)\sin(\beta)\sin(\alpha) - \sin(\theta)\cos(\alpha) & \cos(\theta)\sin(\beta)\cos(\alpha) + \sin(\theta)\sin(\alpha) \\ \sin(\theta)\cos(\beta) & \sin(\theta)\sin(\beta)\sin(\alpha) - \cos(\theta)\cos(\alpha) & \sin(\theta)\sin(\beta)\cos(\alpha) - \cos(\theta)\sin(\alpha) \\ -\sin(\beta) & \cos(\beta)\sin(\alpha) & \cos(\beta)\cos(\alpha) \end{bmatrix} \tag{2.11}$$

From (2.11), the matrix $\boldsymbol{R}$ describes the three degrees of freedom for rotation, which together with the displacement vector $\boldsymbol{t}$ model the overall 3D movement.

In the following, we treat $(x_1,y_1)$ as known constants and $h_1$ the unknown height to be obtained. The gray value at the point $P$ from the deformed fringe patterns captured at time instant $k$ can be expressed as:

$$d_k^P(x_k, y_k) = a_k(x_k, y_k) + b_k(x_k, y_k)\cos\left(\varphi_k^P(x_k, y_k) + \Phi_h^P(x_k, y_k) + \frac{2\pi(k-1)}{K}\right) \tag{2.12}$$

Comparing (2.12) with (2.2) we can see that the 3D movement of the objects leads to the variation of both the position-related phase $\varphi_k^P(x_k, y_k)$ and the height-caused phase $\Phi_h^P(x_1, y_1)$. Such variations of the phases are mixed and hard to be separated and compensated. Meanwhile, the coordinates $(x_k, y_k)$ of the point $P$ are unknown after the movement because neither the movement parameters nor the original heights are available. This is in contrast to the previous studies [84], [94] for 1D or 2D movements where the coordinates of $P$ and variations of the position-related phase can be tracked. Hence it is challenging to retrieve the dynamic height of the surface from the captured patterns. In this chapter, we propose a novel approach to address this problem.

# 2.3 Model fitting-based height retrieval

The overall process of the proposed approach is illustrated in Fig. 2.2 for the case where $K = 3$ fringe patterns are used, but the technique can be generalized to a larger $K$. The key steps are summarized below:

- Acquire coarse estimates of the dynamic shape $\{\widetilde{\boldsymbol{H}}_k\}$ by applying FTP to each fringe image;
- Estimate the object motion parameters $\{\widehat{\boldsymbol{R}}_k, \hat{\boldsymbol{t}}_k\}$ from $\{\widetilde{\boldsymbol{H}}_k\}$ using ICP;

- Retrieve the 3D shape $\widehat{\boldsymbol{H}}_1$ by solving a model fitting problem for all points on the object surface.

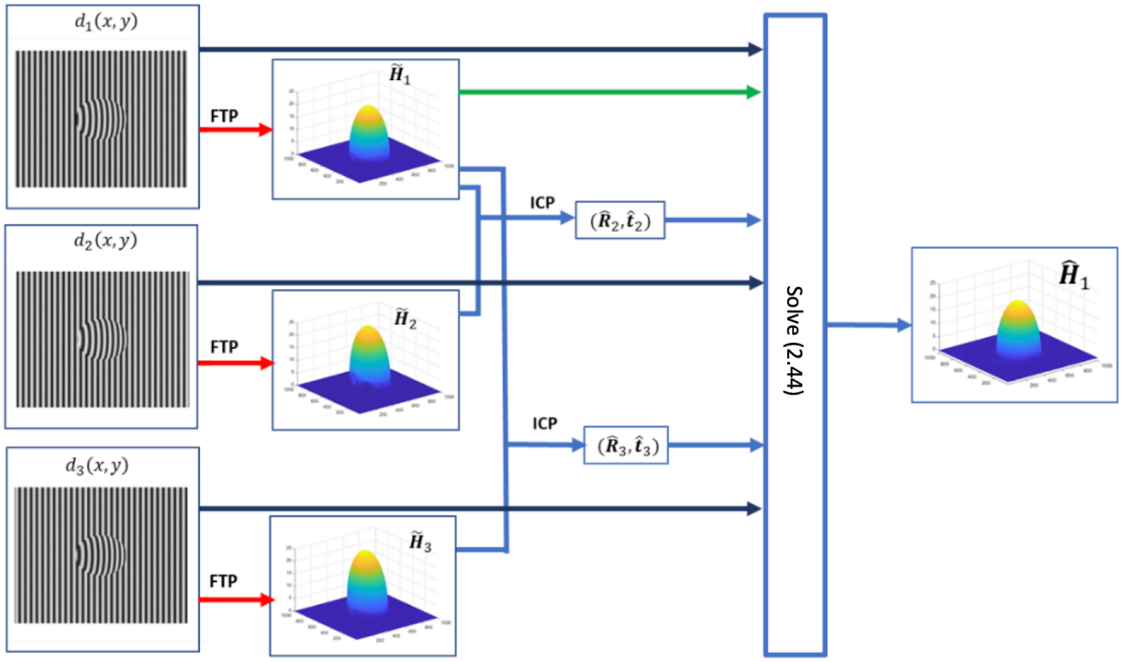


Fig. 2.2 Workflow of the proposed model fitting-based approach when K=3 phase-shifting fringe patterns are employed.

## Step 1: Initial height retrieval

Recall that at each time instant a deformed fringe image is captured, which can be exploited to retrieve a coarse estimate $\widetilde{\boldsymbol{H}}_k$ of the height map $\boldsymbol{H}_k = \{h_k^P\}$. This can be achieved by applying a standard FTP algorithm. At time instant $k$, the fringe pattern deformed by the object can be modeled as a composite of harmonic components [48]:

$$d_k(x,y) = r(x,y)\sum_{n=-\infty}^{\infty} A_n \, exp\left(i\left(2\pi n f_0 x + n\phi_k(x,y)\right)\right), \qquad (2.13)$$

and the corresponding reference fringe pattern is given by

$$s_k(x,y) = r_0(x,y)\sum_{n=-\infty}^{\infty} A_n \exp\left(i\left(2\pi n f_0 x + n\phi_0(x,y)\right)\right), \qquad (2.14)$$

where $r(x, y)$ is the (nonuniform) reflectivity of the object surface and $A_n$ is the Fourier series coefficient. Note that the reference fringe patterns can be obtained and stored before the measurement. Thus only $d_k(x, y)$ needs to be acquired during real-time measurements.

The first step of FTP is applying the Fourier transform on the fringe patterns. The fringe pattern in the frequency domain is illustrated in Fig.2.3. The height information of the object is wrapped into the first side lobe, which corresponds to the region $Q_1$. To extract the component containing the object information, a band-pass filter is employed to remove the rest components. Finally, an inverse Fourier transform is utilized to convert the signal from the frequency domain to the spatial domain, and the filtered pattern is expressed as:

$$\hat{d}_k(x, y) = A_1 r(x, y) \exp\left(i\left(2\pi f_0 x + \phi_k(x, y)\right)\right). \tag{2.15}$$

After similar FTP processing, the reference fringe pattern can be modeled as

$$\hat{s}_k(x, y) = A_1 r_0(x, y) \exp\left(i\left(2\pi f_0 x + \bar{\phi}_k(x, y)\right)\right). \tag{2.16}$$

The differences $\varphi_k(x, y) = \phi_k(x, y) - \bar{\phi}_k(x, y)$ between the phases $\phi_k(x, y)$ and $\bar{\phi}_k(x, y)$ carry the height information of the object at the time instant $k$. From (2.15) and (2.16), the phase difference distribution [48] can be obtained as

$$\varphi_k(x, y) = \mathrm{Im}\{\log [\, \hat{d}_k(x, y) \times \hat{s}_k^*(x, y)]\} \tag{2.17}$$

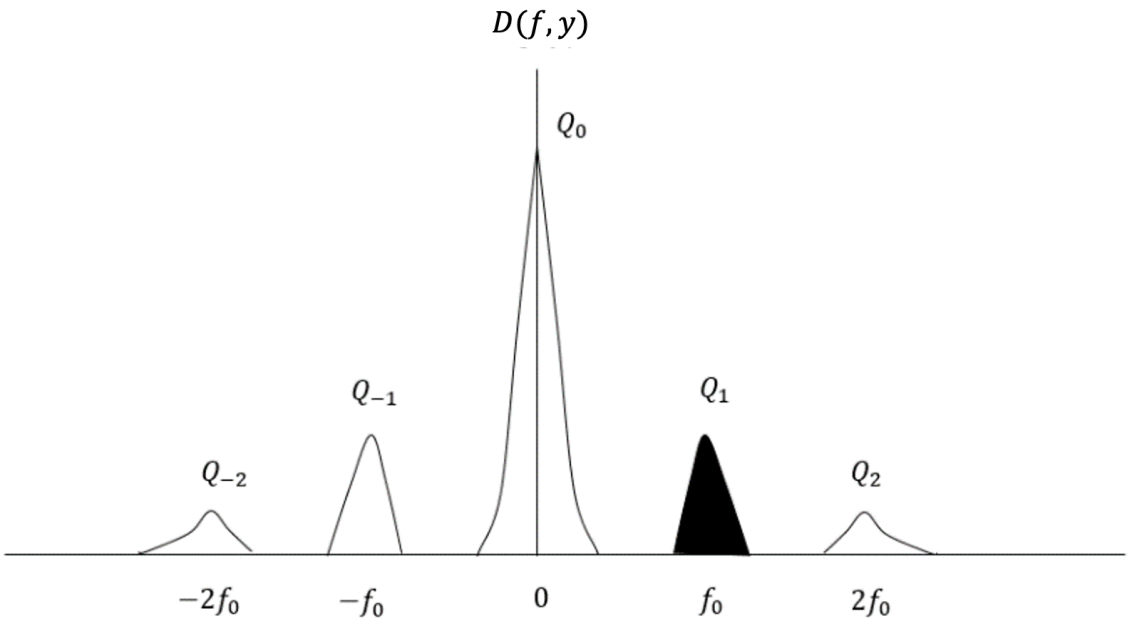


Fig. 2.3 Illustration of the fringe pattern in the frequency domain for a given y

where $*$ denotes conjugate, $\log(.)$ denotes the logarithm function, and $\mathrm{Im}(.)$ is the operation to obtain the imaginary part of the complex number. Note that $\{\varphi_k(x,y)\}$ are wrapped into the range $[-\pi,\pi)$ with $2\pi$ discontinuities. In order to obtain the real height distribution of the object, phase unwrapping algorithms are needed to eliminate the discontinuities in the wrapped phase map to produce the unwrapped phase map [101-116]. The relationships between the wrapped phase and unwrapped phase are shown below:

$$\Phi_k(x,y) = 2\pi I_k(x,y) + \varphi_k(x,y) \tag{2.18}$$

where $\Phi_k(x,y)$ is the unwrapped phase of $\varphi_k(x,y)$, and $I_k(x,y)$ indicates the fringe order. After obtaining the unwrapped phase map, the phase difference caused by the object is retrieved, then the height distribution of the object is obtained by utilizing the triangular relationship of the FPP system. As shown in Fig.1.2, $\Delta E_p E_c H$ is similar to $\Delta CDH$, so the following relationship holds:

$$\frac{\overline{CD}}{d_0} = \frac{-h(x,y)}{l_0 - h(x,y)}. \tag{2.19}$$

Using the fact

$$\Phi_h(x,y) = 2\pi f_0 \overline{CD} \tag{2.20}$$

the height value can be computed as

$$\tilde{h}_k(x,y) = \frac{L_0 \Phi_k(x,y)}{\Phi_k(x,y) - 2\pi f_0 d_0} \tag{2.21}$$

Fig.2.4 demonstrates the flowchart of the FTP algorithm. The FTP measurements at time instant $k$ is denoted by the matrix $\widetilde{\boldsymbol{H}}_k = \{\tilde{h}_k(x,y)\}$.

## Step 2: Estimation of motion parameters

The FTP measurements $\{\widetilde{\boldsymbol{H}}_k\}$ at different time instants provide initial coarse estimates of the dynamic object shape. In order to refine the height measurement, we now estimate the motion parameters by using $\{\widetilde{\boldsymbol{H}}_k\}$. This can be formulated as a point cloud registration problem to establish the correspondence between points in different fringe images [117-122]. Similar problems have been seen in computer vision or image processing [123-129]. We here solve this problem by using iterative closest point (ICP) technique [130-132], Starting from initial coarse estimates of the motion parameters, the correspondence between the points in the different measurements is established using a minimum Euclidean distance criterion.

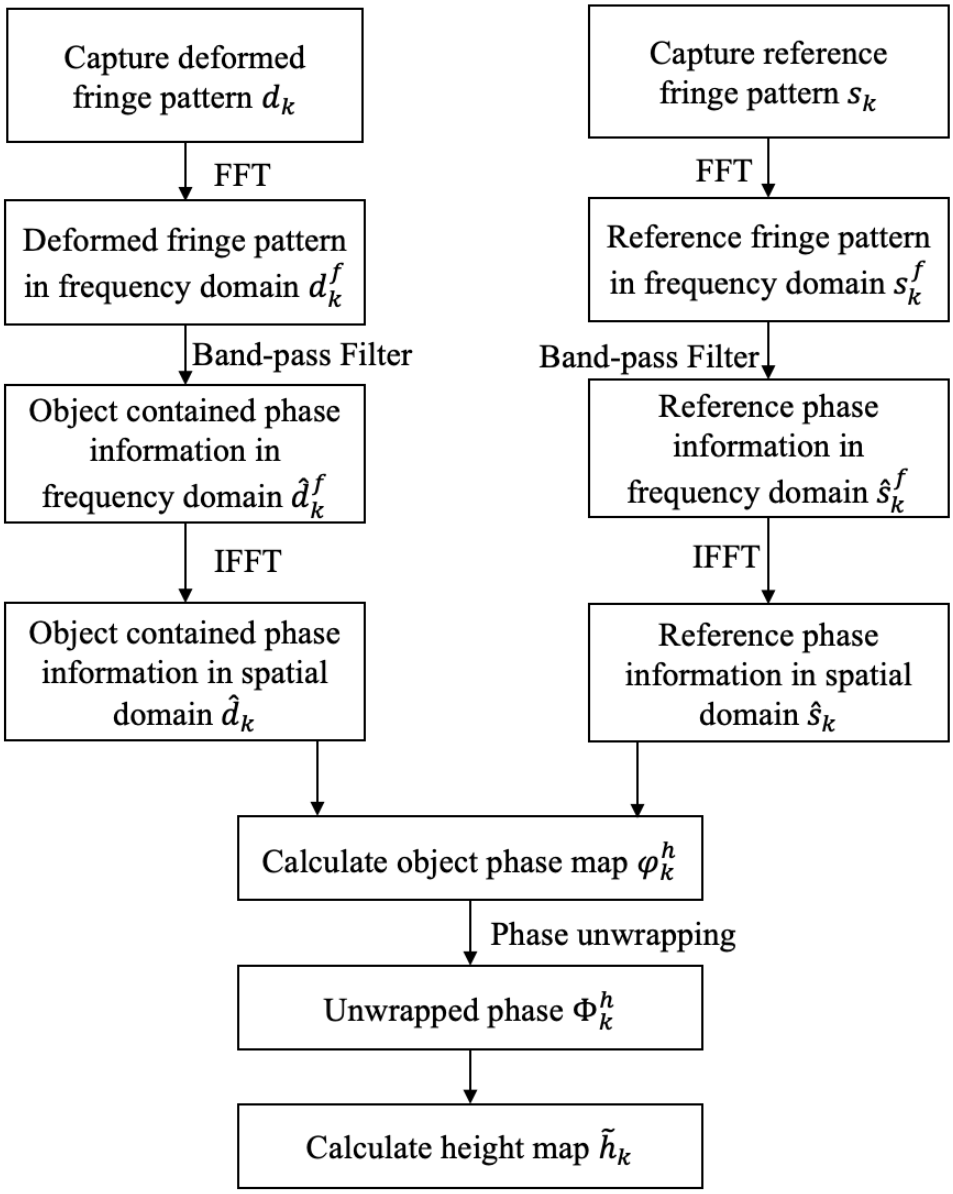


Fig. 2.4 Flowchart of FTP algorithm

The motion parameters are then refined based on the established correspondence using the least squares method. The above correspondence matching and motion parameter estimation are carried out in an iterative manner until a stopping criterion is met. In contrast to the methods using markers and SIFT [93, 94, 96], the ICP approach eliminates the needs of human intervention and feature points extraction for establishing the correspondence. We assume that the height of the reference plane is low and known. A

threshold is then set to distinguish the object and the background and extract the point set corresponding to the object. In general, the object point set $\{\widetilde{\boldsymbol{H}}_k\}$ each may contain a large set of points. Uniform sampling is used to extract a smaller subset of $\{\widetilde{\boldsymbol{H}}_k\}$ $\widetilde{\boldsymbol{H}}_k$ before ICP is applied, such that the computational complexity can be reduced. Let $\boldsymbol{Q} = \{\boldsymbol{q}_m, m = 1,2, \dots, M\}$ and $\boldsymbol{G} = \{\boldsymbol{g}_n, n = 1,2, \dots, N\}$ be the sets of 3D points sampled from the retrieved object surfaces at instant 1 and instant $k$, respectively. Let

$$\boldsymbol{q}_m \triangleq \begin{bmatrix} x_m \\ y_m \\ h_m \end{bmatrix}, \quad \boldsymbol{g}_n \triangleq \begin{bmatrix} u_n \\ v_n \\ z_n \end{bmatrix}, \quad \begin{matrix} m = 1,2, \dots, M, \\ n = 1,2 \dots, N \end{matrix} \tag{2.22}$$

The ICP algorithm aims to obtain the motion parameters and establish the correspondence relationships of the point set $\boldsymbol{Q}$ Qand the point set $\boldsymbol{G}$G. Let the Euclidean distance $d(\boldsymbol{g}_n, \boldsymbol{q}_m)$ between two points $\boldsymbol{g}_n$ and $\boldsymbol{q}_m$ be

$$d(\boldsymbol{g}_n, \boldsymbol{q}_m) = \sqrt{(x_m - u_n)^2 + (y_m - v_n)^2 + (h_m - z_n)^2}. \tag{2.23}$$

For each $\boldsymbol{g}_n$, the corresponding point in $\boldsymbol{Q}$ is estimated as

$$\boldsymbol{q}_n^* = \text{argmin}_{\boldsymbol{q}_m \in \boldsymbol{Q}} d(\boldsymbol{g}_n, \boldsymbol{q}_m). \tag{2.24}$$

Assume that $\boldsymbol{Q}' \triangleq \{\boldsymbol{q}_n^*\}$ is the set containing the estimated corresponding points of $\boldsymbol{G}$. Then the rotation matrix $\boldsymbol{R}$ and translation vector $\boldsymbol{t}$ are estimated by minimizing

$$E(\boldsymbol{R}, \boldsymbol{t}) = \sum_{n=1}^{N} \|\boldsymbol{g}_n - (\boldsymbol{R}\boldsymbol{q}_n^* + \boldsymbol{t})\|^2. \tag{2.25}$$

Let

$$\boldsymbol{q}' = \frac{1}{N}\sum_{n=1}^{N} \boldsymbol{q}_n, \quad \boldsymbol{q}_{cn} = \boldsymbol{q}_n - \boldsymbol{q}', \ n = 1,2, \cdots, N, \tag{2.26}$$

$$\boldsymbol{g}' = \frac{1}{N}\sum_{n=1}^{N} \boldsymbol{g}_n^*, \quad \boldsymbol{g}_{cn} = \boldsymbol{g}_n^* - \boldsymbol{g}', n = 1,2, \cdots, N. \tag{2.27}$$

Define the correlation matrix

$$\boldsymbol{C} = \sum_{n=1}^{N} \boldsymbol{q}_{cn}\, \boldsymbol{g}_{cn}^{T} \tag{2.28}$$

and find its singular value decomposition (SVD) as

$$\boldsymbol{C} = \boldsymbol{U}\boldsymbol{\Lambda}\boldsymbol{V}^{T}. \tag{2.29}$$

Then the optimal rotation matrix $\boldsymbol{R}$ is found as

$$\widehat{\boldsymbol{R}}' = \boldsymbol{V}\boldsymbol{U}^{\boldsymbol{T}} \tag{2.30}$$

and the translation vector $\boldsymbol{t}$ can be determined as:

$$\hat{\boldsymbol{t}}' = \boldsymbol{q}' - \widehat{\boldsymbol{R}}'\boldsymbol{q}' \tag{2.31}$$

The accuracy of $\widehat{\boldsymbol{R}}'$ and $\hat{\boldsymbol{t}}'$ depends on the correspondence established using (2.25). Such correspondence may be poor initially but can be improved iteratively by updating the data points using the estimated motion parameter as $\boldsymbol{q}_m \leftarrow \widehat{\boldsymbol{R}}'\boldsymbol{q}_m + \hat{\boldsymbol{t}}', m = 1,2,\dots,M$. The operations described by (2.25)-(2.31) are then repeated based on the updated data point set $\boldsymbol{Q} = \{\boldsymbol{q}_m\}\mathrm{G} = \{\mathrm{g_m}\}$, yielding updated $\widehat{\boldsymbol{R}}'$ and $\hat{\boldsymbol{t}}'$. Let $\widehat{\boldsymbol{R}}$ and $\hat{\boldsymbol{t}}$ denote the overall rotation matrix and translation vector and initialize them to $\widehat{\boldsymbol{R}} = \boldsymbol{I}_{3\times3}, \hat{\boldsymbol{t}} = \boldsymbol{0}_{3\times1}$. They are then updated iteratively as $\widehat{\boldsymbol{R}} \leftarrow \widehat{\boldsymbol{R}}'\widehat{\boldsymbol{R}}, \hat{\boldsymbol{t}} \leftarrow \widehat{\boldsymbol{R}}'\hat{\boldsymbol{t}} + \hat{\boldsymbol{t}}'$. The above process will be repeated for a preset number of iterations or until the value of the objective function $E(\widehat{\boldsymbol{R}}', \hat{\boldsymbol{t}}')$ becomes lower than a threshold. By letting $\boldsymbol{Q}$ and $\boldsymbol{G}$ be data points from $\widetilde{\boldsymbol{H}}_1$ and $\widetilde{\boldsymbol{H}}_k\mathrm{H_k}$ and applying the ICP algorithm, we can obtain the estimates $(\widehat{\boldsymbol{R}}_k, \hat{\boldsymbol{t}}_k)$ of the motion parameters $(\boldsymbol{R}_k, \boldsymbol{t}_k)$ defined in (2.3) for each time instant. In the end, the movement parameters relating $\widetilde{\boldsymbol{H}}_1$ and $\widetilde{\boldsymbol{H}}_k$ can be estimated.

## Step 3: Height distribution retrieval

We now introduce a new algorithm to recover the shape of the moving object from the captured phase-shifting fringe patterns. We assume that the rotation matrix $\widehat{\boldsymbol{R}}_k$ and translation vector $\hat{\boldsymbol{t}}_k$ estimated in Step 2 are perfect. Similar to the traditional PSP, the shape is retrieved on a point-by-point basis. Hence, it suffices to consider a single point, say $P$, on the object surface in order to introduce the proposed method. From (2.3)-(2.5), the movement of $P$ can be described as

$$x_k = f_k(h_1) \triangleq r_k^{11}x_1 + r_k^{12}y_1 + r_k^{13}h_1 + t_k^1 \tag{2.32}$$

$$y_k = g_k(h_1) \triangleq r_k^{21}x_1 + r_k^{22}y_1 + r_k^{23}h_1 + t_k^2 \tag{2.33}$$

$$h_k = z_k(h_1) \triangleq r_k^{31}x_1 + r_k^{32}y_1 + r_k^{33}h_1 + t_k^3 \tag{2.34}$$

Eq. (2.32) - (2.34) show that the position of the point $P$ can be tracked if $(x_1,y_1,h_1)$ is known and $\boldsymbol{R}_k$ and $\boldsymbol{t}_k$ are available from the ICP algorithm. Note that, however, $h_1$ is unknown. In the following, we introduce a model fitting method to find $h_1$.

We first establish the following model for the captured gray values corresponding to the point $P$:

$$\begin{gathered} M_1(h_1) \triangleq a_1(x_1, y_1) + b_1(x_1, y_1)\cos(\varphi(x_1, y_1) + \Phi_1(h_1)) \\ M_2(h_1) \triangleq a_2(f_2(h_1), g_2(h_1)) + b_2\,(f_2(h_1), g_2(h_1))\cos(\varphi(f_2(h_1), g_2(h_1)) + \Phi_2(z_2(h_1)) + \tfrac{2\pi}{K}) \\ \vdots \\ M_K(h_1) \triangleq a_K(f_K(h_1), g_K(h_1)) + b_K(f_K(h_1), g_K(h_1))\cos(\varphi(f_K(h_1), g_K(h_1)) + \Phi_K(z_K(h_1)) + \tfrac{2\pi(K-1)}{K}) \end{gathered} \tag{2.35}$$

Note that given the target point $P$'s location $(x_1, y_1)$ and the modeling parameters $\{\boldsymbol{R}_k, \boldsymbol{t}_k, a_k(x,y), b_k(x,y)\}$, the values of $M_k(h_1)$ are determined by $h_1$ only. On the other hand, the light intensity of the same point on the acquired fringe patterns are as follows:

$$\begin{aligned} D_1 &\triangleq d_1(x_1, y_1), \\ D_2(h_1) &\triangleq d_2(f_2(h_1), g_2(h_1)), \\ &\vdots \\ D_K(h_1) &\triangleq d_K(f_2(h_1), g_2(h_1)), \end{aligned} \tag{2.36}$$

where $d_k(.,.)$ are the fringe patterns actually acquired by the camera at the time instant $k$.

Equation (2.35) models the intensity value of the point *P* on the object-induced fringe patterns computed using the mathematic model, while (2.35) presents the intensity value of the same point on the fringe patterns actually acquired by the camera. In the noise-free case with no ambient lights, these two sets of intensity values should be the same if $(x_1, y_1, h_1)$ and the modeling parameters are all accurately known. However, as the shape of the object is yet to be measured, $h_1$ is unknown. In the following, we tackle this issue.

Since (2.35) models the light intensity for the same point on the object surface, we can assume that the reflectivity involved are all the same. Following the discussion below (2.12), we can then assume

$$a_k\big(f_k(h_1), g_k(h_1)\big) = a_1(x_1, y_1), k = 2,3 \dots, K, \tag{2.37}$$

$$b_k(f_k(h_1), g_k(h_1)) = b_1(x_1, y_1),\ k = 2,3 \dots, K. \tag{2.38}$$

Consider the case of *K*=3. Based on (2.35), we can then introduce the following metric with the aim to eliminate the influence of $a_k(x, y)$ and $b_k(x, y)$:

$$M(\hat{h}_1) = \frac{M_1(\hat{h}_1) - M_2(\hat{h}_1)}{M_1(\hat{h}_1) - M_3(\hat{h}_1)} = \frac{\cos\left(\varphi(x_1,y_1) + \Phi_1(\hat{h}_1)\right) - \cos\left(\varphi(f_2(\hat{h}_1), g_2(\hat{h}_1)) + \Phi_2(z_2(\hat{h}_1)) + \frac{2\pi}{3}\right)}{\cos\left(\varphi(x_1,y_1) + \Phi_1(\hat{h}_1)\right) - \cos\left(\varphi\big(f_3(\hat{h}_1), g_3(\hat{h}_1)\big) + \Phi_2(z_3(\hat{h}_1)) + \frac{4\pi}{3}\right)} \tag{2.39}$$

Meanwhile, we can also compute the following based on the acquired fringe patterns in (2.36):

$$D(\hat{h}_1) = \frac{D_1 - D_2(\hat{h}_1)}{D_1 - D_3(\hat{h}_1)}. \tag{2.40}$$

With (2.39) and (2.40), we can define a cost function as the following fitting error:

$$J(\hat{h}_1) = \left| M(\hat{h}_1) - D(\hat{h}_1) \right|^2. \tag{2.41}$$

In the ideal case $J(\hat{h}_1)$ is zero if $\hat{h}_1$ is equal to the true height $h_1$ of *P*. Therefore, we propose to estimate the height $h_1$ by solving the following model fitting problem:

$$\hat{h}_1^* = \arg\min_{\hat{h}_1} J(\hat{h}_1). \tag{2.42}$$

Problem (2.42) can be solved by exhaustive search over a feasible range of $\hat{h}_1$. In order to reduce the computational complexity, an initial estimate $\tilde{h}_1$ can be obtained first. The cost function in (2.42) is then minimized over a grid of $\hat{h}_1$ in the neighborhood of $\tilde{h}_1$ to produce a refined solution. In this work, we set such an initial estimate as the coarse estimate of $h_1$ obtained by applying the standard FTP, as illustrated in Step 1, to the fringe image at the time instant $k = 1$.

In practice, ambient lights create random noises in the captured fringe patterns $\{d_k(x_k, y_k)\}$ in (2.36). In contrast to the case where traditional PSP is applied to static objects, the noise in (2.36) can differ from each other and they cannot be fully cancelled in (2.40). As such, the solution of (2.42) can deviate from the true height $h_1$. To improve accuracy, we introduce a local polynomial fitting treatment. Instead of considering only the point *P* at $(x_1, y_1)$ while estimating its height, we consider a small local region $\Omega_P = \{(x_1 - 1, y_1), (x_1, y_1 - 1), (x_1, y_1), (x_1 + 1, y_1), (x_1, y_1 + 1)\}$ which includes the point

$P$ itself and also its four nearest neighbors. We model the object surface over $\Omega_P$ as a planar surface, i.e., the height of every point $P'$ at $(x_1', y_1')$ in $\Omega_P$ can be modeled linearly as

$$h'(\hat{h}_1) = \alpha(\hat{h}_1)(x_1' - x_1) + \beta(\hat{h}_1)(y_1' - y_1) + \hat{h}_1, \tag{2.43}$$

where $\hat{h}_1$ denotes the hypothesized height at point $P$. Given $\hat{h}_1$, the parameters $\alpha(\hat{h}_1), \beta(\hat{h}_1)$ are determined by fitting the FTP measurement results over $\Omega_P$ at $k = 1$ using the ordinary least squares method. Instead of the fitting error $J(\hat{h}_1)$ in (2.41), the sum of the fitting errors over the local surface $\Omega_P$ is chosen as the new cost function. Its minimizer is then used to estimate the height of $P$ as

$$\hat{h}_1^* = \arg\min_{\hat{h}_1} \sum_{P' \in \Omega_P} J\big(h'(\hat{h}_1)\big), \tag{2.44}$$

where $J\big(h'(\hat{h}_1)\big)$ denotes the cost function in (2.41) applied to a point $P'$ in $\Omega_P$.

# 2.4 Numerical Results

In order to quantitatively evaluate the estimated height map $\hat{h}(x, y)$, the NMSE (normalized mean squared error) is computed as:

$$\text{NMSE} = \frac{\sum_y \sum_x (\hat{h}(x,y) - h(x,y))^2}{\sum_y \sum_x (h(x,y))^2}, \tag{2.45}$$

where $h(x, y)$ is the true height map, $X$ and $Y$ are the numbers of pixels along the $x$-axis and $y$-axis, respectively.

We first examine the feasibility of applying the ICP algorithm to estimate the motion parameters. Consider an FPP system with $l_0 = 4000$mm and $d_0 = 600$mm. A spatially symmetric hemi-ellipsoidal object (with radius 200mm and height 20mm) is simulated as

shown in Fig.2.5(a) and then transformed by a known rotation matrix and translation vector into that in Fig.2.5(b). We treat the height map as a two-dimensional signal with average power $P_h$Ph. Noise with average power $P_n$Pn is added to the height distribution and the signal-to-noise ratio (SNR) is defined asSNR $= 10\log\frac{\mathrm{P_h}}{\mathrm{P_n}} SNR = 10log\frac{P_h}{P_n}$. The motion parameters are estimated by using the ICP algorithm from the two point clouds from Fig.2.5(a) and Fig.2.5(b). They can then be utilized to transform the height map in Fig.2.5(b) to predict that in Fig. 2.5(a). The prediction error refers to the difference between the height map in Fig. 2.5(a) and its prediction obtained from Fig.2.5(b) using the estimated motion parameters, which is shown in Fig.2.5(c) for $SNR = 30$ dB. The NMSE of the prediction is found to be 0.0032, 0.0108 and 0.0214 respectively under the SNR of 30 dB, 25dB and 20 dB.

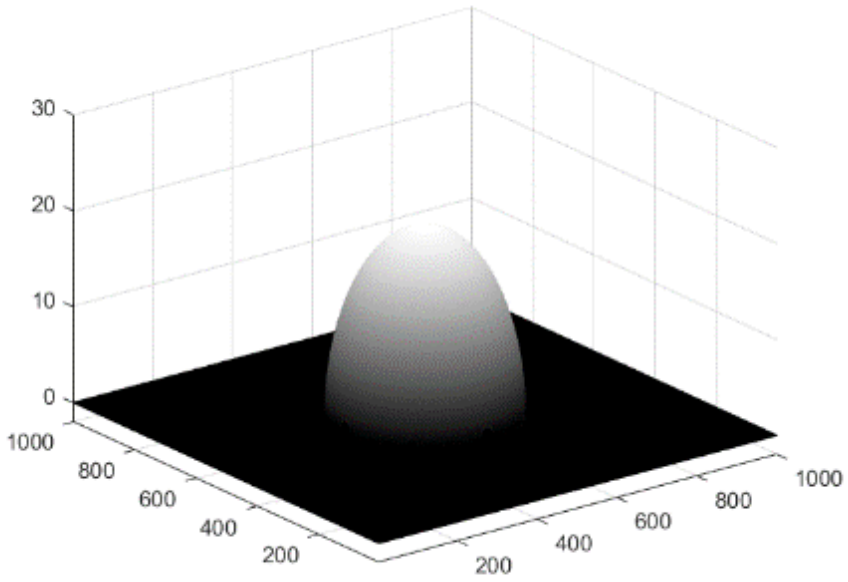


(a)

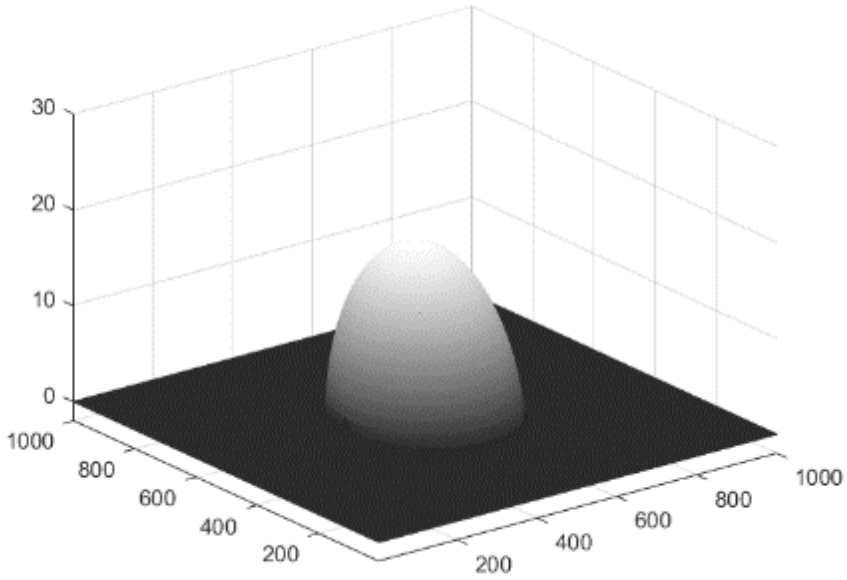


(b)

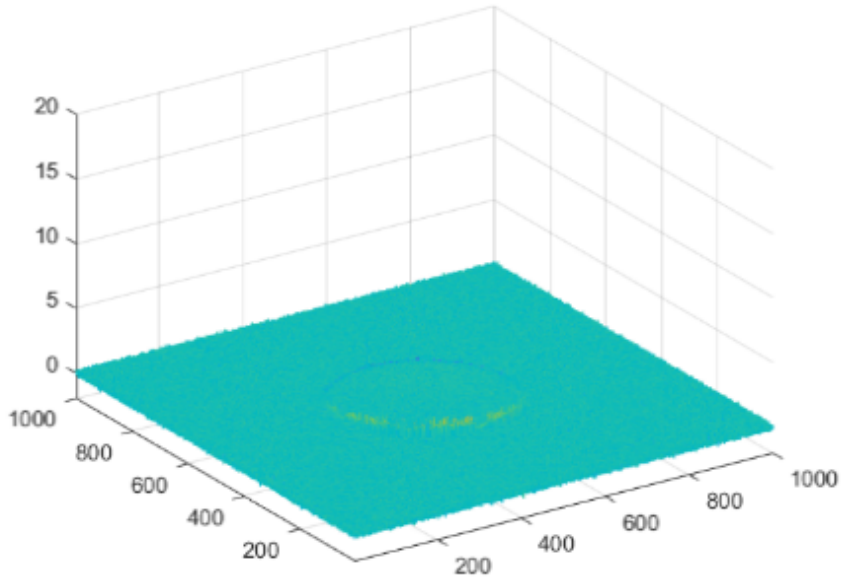


(c)

Fig. 2.5 Verification of the ICP algorithm at SNR=30dB. (a): Object before movement. (b): Object after movement. (c): Difference between the original object in (a) and its prediction obtained from (b) using the estimated motion parameters.

These results demonstrate the feasibility of using the ICP algorithm to estimate the motion parameters from noisy height maps. From Fig. 2.5(c), there can be a slight difference between the original map and the predicted map using the motion parameters estimated. This difference is partly caused by the modeling errors due to imperfect motion parameters estimation and linear interpolation. Note also that for spatially symmetric objects the same motion of the object may be described using different models. In this case, the motion parameters found by the ICP algorithm are not unique. In noisy cases, ICP aims to find the motion parameters that minimize the prediction errors described above.

We next present simulation results to verify the effectiveness of the proposed model fitting approach. In the first simulation, the proposed approach is compared with the traditional 3-step PSP and FTP methods. A hemi-ellipsoidal object with 3D movement is considered and its shape at three time instants $k = 1, 2, 3$ during the movement is shown in Fig. 2.6. We assume that phase-shifting fringe images are captured at the three time instants, based on which the object shape at the time instant $k = 1$ is retrieved. Fig. 2.7 compares the NMSE of the proposed approach with the alternative methods. The motion parameters $\{\boldsymbol{R}_k, \boldsymbol{t}_k\}$ are assumed perfectly known. The traditional 3-step PSP scheme is first applied to the three fringe images with the assumption that the object is static. From Fig. 2.7, it yields the worst NMSE for the height measurement, which cannot be alleviated by improving the SNR. This is due to the motion-induced artifact. The FTP applied to the fringe image at $k = 1$ is able to achieve a better NMSE thanks to its immunity to the object movement, but it is sensitive to noise due to its single-shot nature. The proposed modified PSP approach noticeably outperforms the two alternatives. This approach utilizes multiple fringe patterns and hence is more robust against noise compared to FTP. Furthermore, it alleviates the motion-induced artifact, which degrades the performance of

the traditional PSP, by estimating the motion parameters and compensating the motion-induced phase shifts.

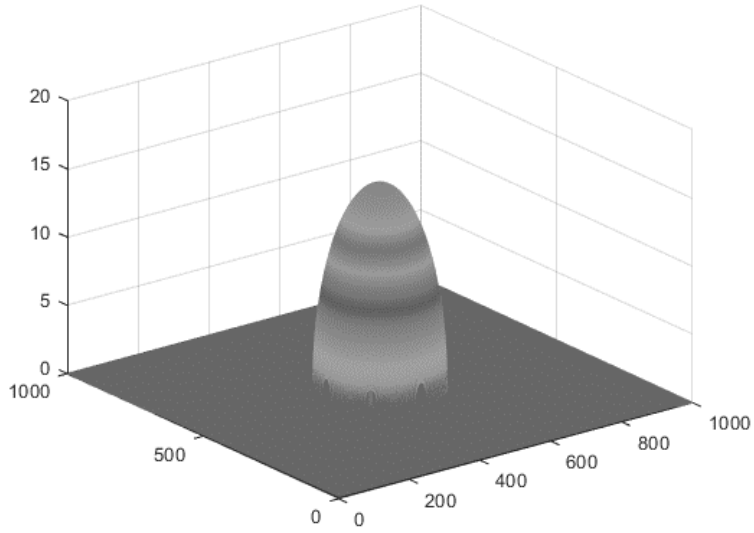


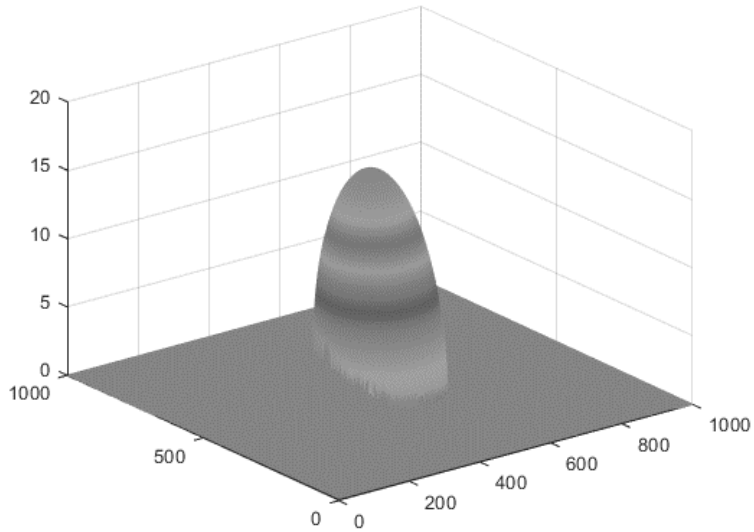

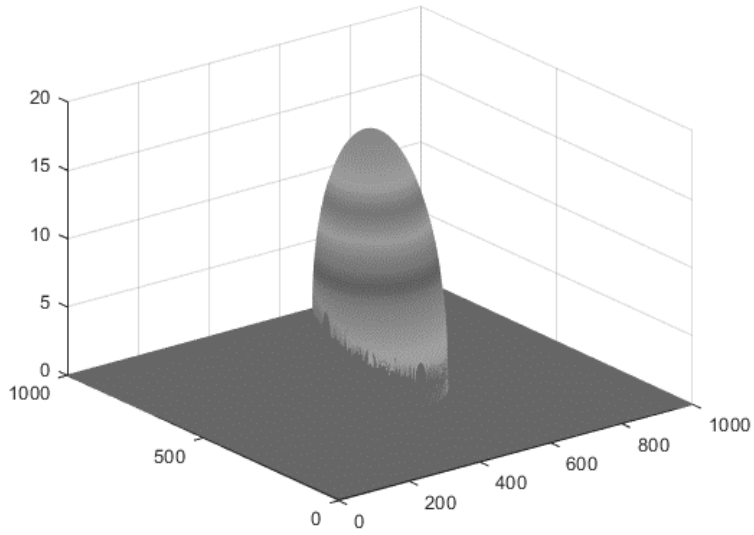


Fig. 2.6 Three states of a moving 3D object.

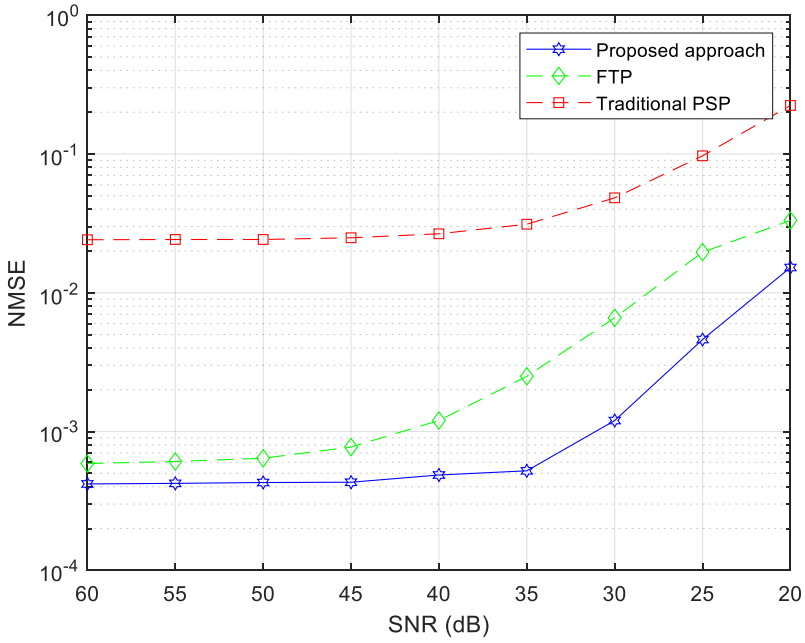


Fig. 2.7 Comparison of the proposed approach, the traditional 3-step PSP, and FTP.

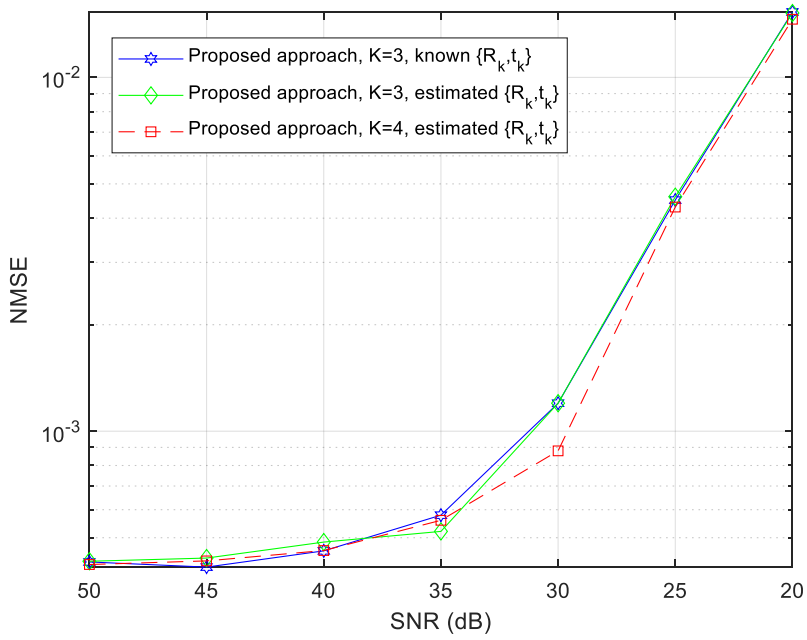


Fig.2.8 Influence of the knowledge of the motion parameter and number of steps on the proposed approach.

In Fig. 2.8, we examine the influence of the motion parameter estimation. The ICP-estimated motion parameters $(\widehat{\boldsymbol{R}}_k, \hat{\boldsymbol{t}}_k)$ are shown to yield nearly the same performance as the true $\{\boldsymbol{R}_k, \boldsymbol{t}_k\}$. Besides, we can also extend the proposed approach to employ more fringe projections. When $K = 4$, four fringe images are used. The metrics of $M(\hat{h}_1)$ and $D(\hat{h}_1)$ defined in (2.39) and (2.40) can be modified as follows before plugged into (2.41):

$$M(\hat{h}_1) = \frac{M_1(\hat{h}_1) - M_2(\hat{h}_1)}{M_3(\hat{h}_1) - M_4(\hat{h}_1)}, \quad D(\hat{h}_1) = \frac{D_1 - D_2(\hat{h}_1)}{D_3(\hat{h}_1) - D_4(\hat{h}_1)}. \tag{2.46}$$

From Fig. 2.8, employing more fringe projections may improve the accuracy of 3D reconstruction. However, the improvement can be limited by the errors in the estimated motion parameters.

## 2.5 Summary

In this chapter, a model-fitting approach has been proposed to compensate for the motion-induced errors in fringe projection profilometry. The proposed approach utilizes multiple phase-shifting fringe projections. The initial coarse estimates of the object height are obtained using Fourier transform profilometry based on which the motion parameters are estimated. A model of the deformed patterns is established, which takes into account the movement of the object surface in the 3D space. The model is fitted to the acquired fringe patterns, and the fitting error is minimized to retrieve the height map. The simulation results show that the proposed approach is effective in improving the accuracy of 3D shape reconstruction for moving objects.

# 3. DATA FUSION-BASED RECONSTRUCTION OF DYNAMIC OBJECTS WITH 3D MOVEMENT

## 3.1 Introduction

Chapter 2 proposes a model fitting approach to improve the performance for 3D shape measurement of objects with 3D movements. This approach employs exhaustive search to retrieve the height value, which is time-consuming. In order to reduce the computation complexity, we now propose a novel approach to enhancing the performance by fusing multiple height maps retrieved using standard FPP. We also consider rigid objects moving freely in the 3D space. Initial coarse measurements are obtained first, and robust principal component analysis (RPCA) is employed to alleviate the noise-induced errors. The results are then utilized to estimate the 3D motion parameters by applying the iterative closest point (ICP) method. Finally, we fuse the multiple height maps to obtain the final result using weights adapted to the quality of the captured fringe patterns.

The chapter is organized as follows. Section 3.2 presents the proposed method. Section 3.3 presents the simulation and experiment. Finally, conclusions are drawn in Section 3.4.

## 3.2 Data fusion approach

### 3.2.1 FTP-based fusion approach

FTP requires the projection of only one fringe pattern for each measurement. Its performance is insensitive to the motion, and hence it can be applied to each time instant to obtain a height map for a moving object. However, the performance of FTP is sensitive to background lights and abrupt changes of the object surface due to its single-shot nature. It is possible to fuse the FTP results from different time instants to achieve high-performance reconstruction. However, correspondence between these data must be established first. Besides, the single FTP results from different time instants may have different quality, which should also be taken into account.

In this section, we propose a method to improve the performance of the FTP approach for measuring moving objects by fusing multiple coarse measurements acquired at different time instants. The overall workflow is illustrated in Fig.3.1. Assume that FTP measurements at $K = 3$ time instants are fused as an example. The key steps are summarized below:

- Retrieve individual height map $\{\widetilde{\boldsymbol{H}}_k\}$ from each time instant $k$, and then denoise these maps by using robust principal component analysis (RPCA).
- Produce the resulting height maps $\{\widehat{\boldsymbol{H}}_k\}$ to estimate $(\widehat{\boldsymbol{R}}_k, \hat{\boldsymbol{t}}_k)$ of the 3D motion parameters by applying the ICP algorithm.
- Fuse height maps $\{\widehat{\boldsymbol{H}}_k\}$ with adaptive weights computed from the signal-to-noise ratios (SNR) $\{\Gamma_k\}$ to optimize the overall accuracy.

Note that the method can be easily extended to other values of $K$ and to the cases where multiple measurements are performed simultaneously using multiple cameras.

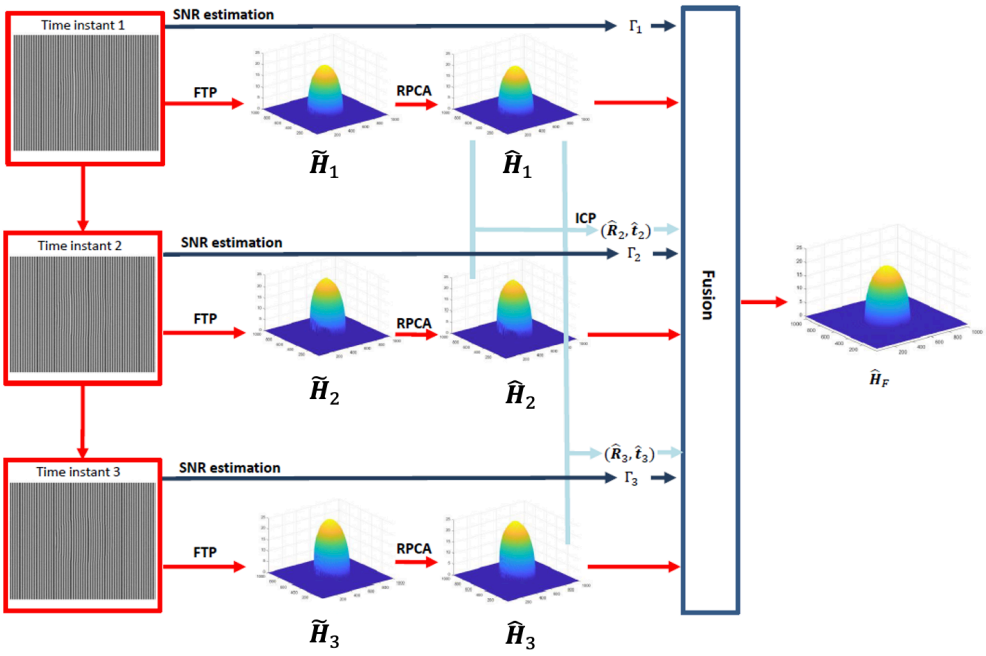


Fig. 3.1 Workflow of the proposed approach when height maps acquired at $K = 3$ time instants are fused.

## Step 1: Retrieval of initial height maps with denoising

A standard FTP process is applied to retrieve an object height map at each time instant. Since a single pattern is used for acquiring each height map, there can be significant errors in the retrieved height maps due to noise, etc. Such errors can lead to poor results for further processing.

Denote by matrix $\widetilde{\boldsymbol{H}}_k = \{\tilde{h}_k(x, y)\}$the height map obtained using FTP at time instant $k$. We can model $\widetilde{\boldsymbol{H}}_k$as the summation of the true object shape matrix $\boldsymbol{H}_k$, an impulsive error matrix $\boldsymbol{S}_k$, and a random, unstructured error matrix $\boldsymbol{W}_k$, i.e.,

$$\widetilde{\boldsymbol{H}}_k = \boldsymbol{H}_k + \boldsymbol{S}_k + \boldsymbol{W}_k, \ k = 1,2,\cdots,K. \tag{3.1}$$

For many applications, the object to be measured has a continuous surface shape, and in this case, it is reasonable to assume that $\boldsymbol{H}_k$ is a low-rank matrix, i.e., it can be represented

in a low-dimensional subspace using a small number of singular vectors. Meanwhile, the impulsive error $\boldsymbol{S}_k$ is sparse, i.e., only a small subset of its entries is non-zero with significant magnitudes. The above distinct features of $\boldsymbol{H}_k$ and $\boldsymbol{S}_k$ can be applied to recover them from $\widetilde{\boldsymbol{H}}_k$ with high accuracy. Intuitively, $\boldsymbol{S}_k$ can be estimated by thresholding the entries of $\widetilde{\boldsymbol{H}}_k$ while $\boldsymbol{H}_k$ can be retrieved by projecting $\widetilde{\boldsymbol{H}}_k$ onto the low-dimensional subspace spanned by its principal singular vectors. These processes, however, are subject to errors due to the mixing of $\boldsymbol{H}_k$ and $\boldsymbol{S}_k$ in $\widetilde{\boldsymbol{H}}_k$. In order to enhance accuracy, iterative algorithms can be applied to refine the estimates of $\boldsymbol{H}_k$ and $\boldsymbol{S}_k$ [133-139]. Various implementations of RPCA have been proposed in the past decade, e.g. [140], [141], which have been successfully applied to many areas such as computer vision.

The original RPCA can be formulated as a matrix decomposition problem, which incorporates rank and sparsity constraints. This problem is non-convex and NP-hard. In order to obtain tractable solutions, one can heuristically reformulate RPCA as the following principal component pursuit (PCP) problem [141]:

$$\min_{\boldsymbol{S}_k,\boldsymbol{H}_k} \gamma\|\boldsymbol{S}_k\|_{l_1} + \|\boldsymbol{H}_k\|_* \quad \text{s.t. } \left\|\boldsymbol{H}_k + \boldsymbol{S}_k - \widetilde{\boldsymbol{H}}_k\right\|^2 \leq \epsilon^2. \tag{3.2}$$

In the above, $\|\cdot\|_{l_1}$ is the $l_1$ norm, defined as the sum of the absolute values of the entries of a matrix, and $\|\cdot\|_*$ is the nuclear norm, defined as the sum of the singular values. The PCP reformulation is motivated by the fact that the $l_1$ norm and nuclear norm can act as surrogate functions of the sparsity level and rank, respectively. Therefore, minimizing these norms as in (3.2) can induce a sparse $\boldsymbol{S}_k$ and a low-rank $\boldsymbol{H}_k$, subject to a tolerance of residual errors. The rank, sparsity level, and level of residual errors of the solutions can be controlled by the parameters $\gamma > 0, \epsilon^2 > 0$. In particular, a smaller value of $\epsilon^2$ requires the residual error to be smaller. The parameter $\gamma$ controls the rank of the

recovered $\boldsymbol{H}_k$. A smaller $\gamma$ leads to a lower rank of $\boldsymbol{H}_k$, which may oversmooth the result and discard details of the shape information. A larger $\gamma$ leads to a larger rank of $\boldsymbol{H}_k$, which tends to include more errors in the recovered $\boldsymbol{H}_k$. The choice of $\gamma$ has been a topic intensively studied in the literature. However, there is no universally optimal solution available. So, we resort to numerical studies by simulating common objects under different shape complexity and noise levels and identify a suitable range for $\gamma$.

Various low-complexity algorithms have been proposed to solve (3.2). We here apply the alternating direction method (ADM) of [142] for its simplicity, but other methods [140, 141] can be alternatively used. For completeness, the ADM method is sketched as follows. Firstly, a multiplier $\boldsymbol{Z}_k$ is introduced to construct a cost function from (3.2) as

$$J(\boldsymbol{S}_k, \boldsymbol{H}_k, \boldsymbol{Z}_k) = \gamma \|\boldsymbol{S}_k\|_{l_1} + \|\boldsymbol{H}_k\|_* - \langle \boldsymbol{Z}_k, \boldsymbol{S}_k + \boldsymbol{H}_k - \widetilde{\boldsymbol{H}}_k \rangle + \frac{\rho}{2} \left\| \boldsymbol{S}_k + \boldsymbol{H}_k - \widetilde{\boldsymbol{H}}_k \right\|^2, \tag{3.3}$$

where $\rho > 0$ is a penalty parameter for controlling the tolerance of the residual error, and $\langle \cdot \rangle$ represents the standard trace inner product. The optimization problem then becomes the minimization of $J(\boldsymbol{S}_k, \boldsymbol{H}_k, \boldsymbol{Z}_k)$. Let $P^t(\cdot)$ be a thresholding operator with threshold $t > 0$, that is, $P^t(\mathbf{X})$ returns a matrix obtained by thresholding all the entries of $\boldsymbol{X}$ into the range $[-t, t]$. Let $n$ denotes the number of iteration of the ADM method, and $(\boldsymbol{S}_k^n, \boldsymbol{H}_k^n, \boldsymbol{Z}_k^n)$ the current solution. The solutions are then updated iteratively as follows:

- Generate $\boldsymbol{S}_k^{n+1}$:

$$\boldsymbol{S}_k^{n+1} = \left(\frac{1}{\rho}\boldsymbol{Z}_k^n - \boldsymbol{H}_k^n + \widehat{\boldsymbol{H}}_k\right) - P^{\frac{\gamma}{\rho}}\left(\frac{1}{\rho}\boldsymbol{Z}_k^n - \boldsymbol{H}_k^n + \widetilde{\boldsymbol{H}}_k\right). \tag{3.4}$$

- Generate $\boldsymbol{H}_k^{n+1}$:

$$\boldsymbol{H}_k^{n+1} = \boldsymbol{U}^{n+1}\text{diag}\left(\max\left\{\sigma_i^{n+1} - \frac{1}{\rho}, 0\right\}\right)(\boldsymbol{V}^{n+1})^T, \tag{3.5}$$

where $\boldsymbol{U}^{n+1}$, $\boldsymbol{V}^{n+1}$ and $\{\sigma_i^{n+1}\}$ are, respectively, the left singular vector matrix, right singular vector matrix and singular values of $\widetilde{\boldsymbol{H}}_k - \boldsymbol{S}_k^{n+1} + \frac{1}{\rho}\boldsymbol{Z}_k^n$.

- Update the multiplier:

$$\boldsymbol{Z}_k^{n+1} = \boldsymbol{Z}_k^n - \rho(\boldsymbol{S}_k^{n+1} + \boldsymbol{H}_k^{n+1} - \widetilde{\boldsymbol{H}}_k). \tag{3.6}$$

The above iterative algorithm can be terminated based on a pre-set number of iterations or variations of the solutions. We refer the readers to [142] for detailed discussion about the properties and implementation of the ADM method.

## Step 2: Motion parameter estimation

After applying the FTP and RPCA steps in step 1, $K$ height maps $\{\widehat{\boldsymbol{H}}_k\}$ are obtained, which may still suffer from errors. Fusing these height maps may improve the overall accuracy of the 3D reconstruction. In order to achieve this, we estimate the rotation matrix and translation vector from $\{\widehat{\boldsymbol{H}}_k\}$. Similar to Section 2.2, the ICP algorithm applied in this section is to find the transformation from $\{\widehat{\boldsymbol{H}}_k\}$ to $\{\widehat{\boldsymbol{H}}_1\}$, which is described by

$$\begin{bmatrix} x_1^P \\ y_1^P \\ h_1^P \end{bmatrix} = \bar{\boldsymbol{R}}_k \begin{bmatrix} x_k^P \\ y_k^P \\ h_k^P \end{bmatrix} + \bar{\boldsymbol{t}}_k \; k = 1,2,\cdots,K, \tag{3.7}$$

where $\bar{\boldsymbol{R}}_k$ and $\bar{\boldsymbol{t}}_k$ denote the rotation matrix and translation vector from the time instant $k$ to the time instant 1, respectively, and

$$\bar{\boldsymbol{R}}_k = \boldsymbol{R}_k^{-1}, \quad \bar{\boldsymbol{t}}_k = -\boldsymbol{R}_k^{-1}\boldsymbol{t}_k. \tag{3.8}$$

In this chapter, we denote by $(\widehat{\boldsymbol{R}}_k, \hat{\boldsymbol{t}}_k)$ the estimates of $(\overline{\boldsymbol{R}}_k, \bar{\boldsymbol{t}}_k)$. In the case of $k = 1$ for the first instant, $\widehat{\boldsymbol{R}}_1 = \boldsymbol{I}_{3\times3}, \hat{\boldsymbol{t}}_1 = \boldsymbol{0}_{3\times1}$.

## Step 3: Height maps fusion with adaptive weights

After obtaining the motion parameters $(\widehat{\boldsymbol{R}}_k, \hat{\boldsymbol{t}}_k)$ for $k = 2,3,\cdots,K$, the measurement results at different time instants can be fused. Let $\hat{r}_k^{ij}$ denote the $(i,j)$th entry of $\widehat{\boldsymbol{R}}_k$ and $\hat{t}_k^n$ the $n$th entry of $\hat{\boldsymbol{t}}_k$. According to (3.7), we can generate $K$ estimates of the height map at instant $k = 1$ from $(\widehat{\boldsymbol{R}}_k, \hat{\boldsymbol{t}}_k)$ and $\widehat{\boldsymbol{H}}_k$ as

$$\tilde{h}_{1,k}^P(x_1^P, y_1^P) = \hat{r}_k^{31} x_k^P + \hat{r}_k^{32} y_k^P + \hat{r}_k^{33}\, \tilde{h}_k^P + \hat{t}_k^3, \qquad k = 1,2,\cdots,K. \tag{3.9}$$

In the above, $(x_k^P, y_k^P)$ denote the coordinates of a point $P$ at the time instant $k$, and $\hat{h}_k^P$ the corresponding height in map $\widehat{\boldsymbol{H}}_k$. Linear interpolation is used to obtain $\hat{h}_{1,k}^P$ when $(x_k^P, y_k^P)$ do not fall on the center of a pixel. Finally, we fuse the multiple height maps in (3.9) to further alleviate noise-induced errors and improve accuracy. Note that due to the variations of the signal-to-noise-ratio (SNR), reflectivity, and orientation of the object with respect to the fringe patterns, the measured heights for the same point at different time instants have different accuracies. A weighted combination of the multiple height maps is employed with weights $\{w_k\}$:

$$\hat{h}_F(x_1^P, y_1^P) = \textstyle\sum_{k=1}^K w_k\, \hat{h}_{1,k}^P\big(x_{1,k}^P, y_{1,k}^P\big), \tag{3.10}$$

where we use the coordinates at time instant $k = 1$ to present the final height map $\widehat{\boldsymbol{H}}_F = \{\hat{h}_F(x_1^P, y_1^P)\}$. The optimal choice of $\{w_k\}$ is an open issue. In this work, we consider a heuristic approach similar to the maximum ratio combining (MRC) [143] that chooses $\{w_k\}$ according to estimates of the SNR in the fringe images $d_k(x,y)$ captured by the camera, which can be also modelled as:

$$d_k(x,y) = a_k(x,y) + b_k(x,y)cos\big(\varphi(x,y)\big) + n(x,y) \tag{3.11}$$

where $n(x,y)$ is the noise. Assume that the captured deformed fringe patterns contain the zero-mean noises $n(x,y)$ with variance $\sigma^2$, which are independent of the fringe signals. Then $a_k$ and $b_k$ can be estimated by averaging the captured images and curve fitting, respectively. We can verify that

$$\frac{1}{\hat{Q}\hat{T}}\sum_x d_k^2(x,y) \approx a_k^2 + \frac{b_k^2}{2} + \sigma^2, \tag{3.12}$$

where $\hat{T}$ is the period of the fringe and $\hat{Q}$ is the number of fringes. Therefore, we can obtain an estimate of the SNR of the captured image as:

$$\Gamma_k \triangleq \frac{\frac{1}{\hat{Q}\hat{T}}\sum_x\left(a_k+b_k\cos(\varphi(x,y))\right)^2}{\frac{1}{\hat{Q}\hat{T}}\sum_x n^2(x,y)} \approx \frac{a_k^2+\frac{b_k^2}{2}}{\frac{1}{\hat{Q}\hat{T}}\sum_x d_k^2(x,y)-\left(a_k^2+\frac{b_k^2}{2}\right)}. \tag{3.13}$$

Finally, we set the combining weights in (3.13) as

$$w_k = \frac{\sqrt{\Gamma_k}}{\sum_{n=1}^{K}\sqrt{\Gamma_k}}. \tag{3.14}$$

## 3.3.2 PSP-based fusion approach

The FTP-based fusion approach improves the reconstruction accuracy by denoising the height maps and then fusing the height maps with adaptive weights. However, the steep slope on object surface leads to the failure of the reconstruction from FTP. To combat this problem and achieve higher reconstruction accuracy, we extend the FTP-based fusion approach to PSP-based. The overall workflow of the proposed method is illustrated in Fig.3.2.

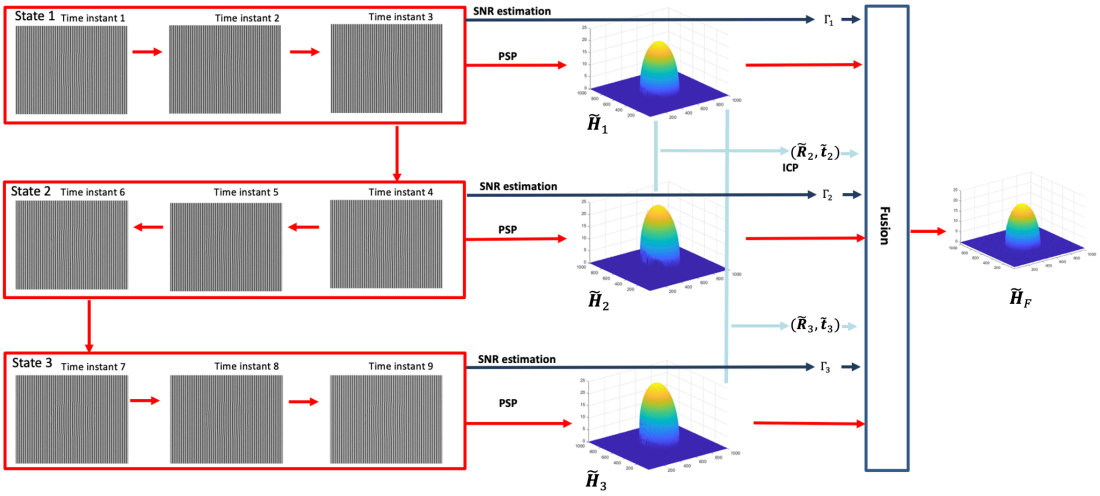


Fig.3.2

Fig. 3.2 Workflow of the PSP-based fusion approach when height maps acquired at $K$=9 time instants with $J$=3 states are fused.

## Step 1: Retrieval of initial height maps by PSP algorithm

Due to the multiple shots nature of PSP, the reconstruction of the object requires multiple fringe patterns from multiple time instants. So, we consider in total $J$ states of the object in motion and total $K$ fringe patterns are projected. At each movement state $j$, a small number of $\dot{K}$ fringe patterns are employed to reconstruct the object. Let $d_{\dot{k}}(x,y)$ be the $\dot{k}$th fringe image acquired at an arbitrary state and $s_{\dot{k}}(x,y)$ the corresponding reference image. From (2.11) and (2.12), the phase maps for the cases without and with an object can be retrieved as

$$\varphi^{s}(x,y) = \varphi(x,y) = \tan^{-1}\frac{-\sum_{\dot{k}=1}^{\dot{K}} s_{\dot{k}}(x,y)\sin\left(\frac{2\pi(\dot{k}-1)}{\dot{K}}\right)}{\sum_{\dot{k}=1}^{\dot{K}} s_{\dot{k}}(x,y)\cos\left(\frac{2\pi(\dot{k}-1)}{\dot{K}}\right)} \tag{3.15}$$

and

$$\varphi^d(x,y) = \varphi(x,y) + \Phi_h(x,y) = \tan^{-1}\frac{-\sum_{\dot{k}=1}^{\dot{K}} d_{\dot{k}}(x,y)\sin\left(\frac{2\pi(\dot{k}-1)}{\dot{K}}\right)}{\sum_{\dot{k}=1}^{\dot{K}} d_{\dot{k}}(x,y)\cos\left(\frac{2\pi(\dot{k}-1)}{\dot{K}}\right)} \tag{3.16}$$

In (3.15) and (3.16), the retrieved phase values are wrapped into $[-\pi, \pi)$. Phase unwrapping is then applied to obtain the absolute phase distribution $\Phi^s(x,y)$ and $\Phi^d(x,y)$. Then the phase difference caused by object shape can be calculated by

$$\Phi_h(x,y) = \Phi^d(x,y) - \Phi^s(x,y). \tag{3.17}$$

The height distribution can then be retrieved in the same way as (2.25). In summary, the flow chart of the PSP algorithm at each state is given in Fig. 3.3.

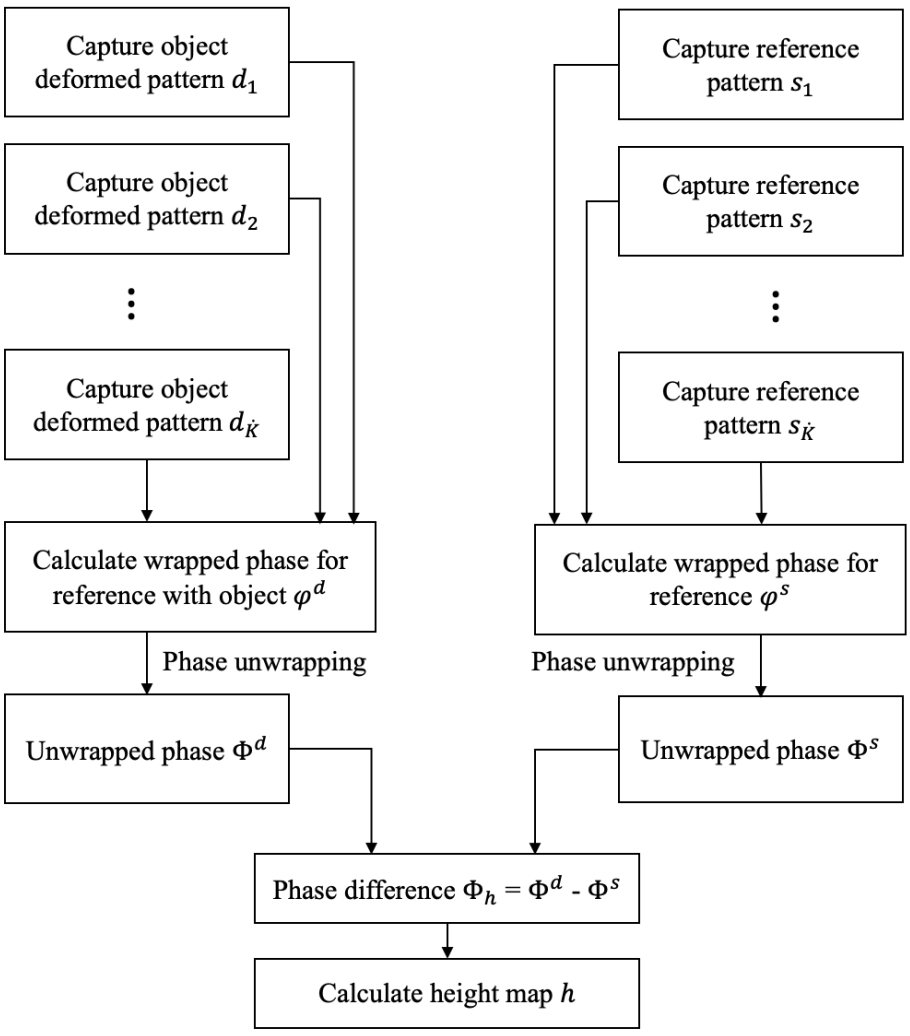


Fig. 3.3 Flowchart of the PSP algorithm

Since only a small number of patterns are used for acquiring each height map $\{\widetilde{\boldsymbol{H}}_j\}$ at each state, there are less motion-induced errors compared to PSP with large number of patterns. Compared to the FTP approach introduced earlier, more complex objects with steeper slopes can be reconstructed.

**Step 2: Motion parameters estimation**

After applying PSP, the initial height maps $\{\widetilde{\boldsymbol{H}}_j\}$ are obtained. To build correspondence among multiple height maps $\{\widetilde{\boldsymbol{H}}_j\}$, we also apply the ICP algorithm from Chapter 2 to estimate the 3D motion parameters $\widetilde{\boldsymbol{R}}_j$ and $\tilde{\boldsymbol{t}}_j$.

**Step 3: Height maps fusion with adaptive weights**

The final fused height map $\widetilde{\boldsymbol{H}}_F$ is obtained by applying adaptive weights calculated from the signal-to-noise ratios (SNR) $\{\Gamma_j\}$ of the captured fringe patterns, in the same way as the FTP-based fusion approach.

# 3.4 Simulation and experimental results

- **FTP based data approach**

We first verify the effectiveness of the FTP based fusion method. The workflow as demonstrated in Fig.3.1 is considered. In the simulation, the movement parameters at the three time instants are listed in Table 3.1 from (3.7), where the details of rotation angles and translation distance are from Chapter 2.

| Time instant | $(\alpha, \beta, \theta)$ | $\boldsymbol{t}$(mm) |
|---|---|---|
| 1 | 0°, 0°, 0° | (0,0,0) |

| | | |
|---|---|---|
| 2 | $-0.32°, -0.48°, 0.32°$ | (3,3,2) |
| 3 | $-0.64°, -0.64°, 0.64°$ | (5,6,4) |

Table. 3.1 Rotation angles and translation distance

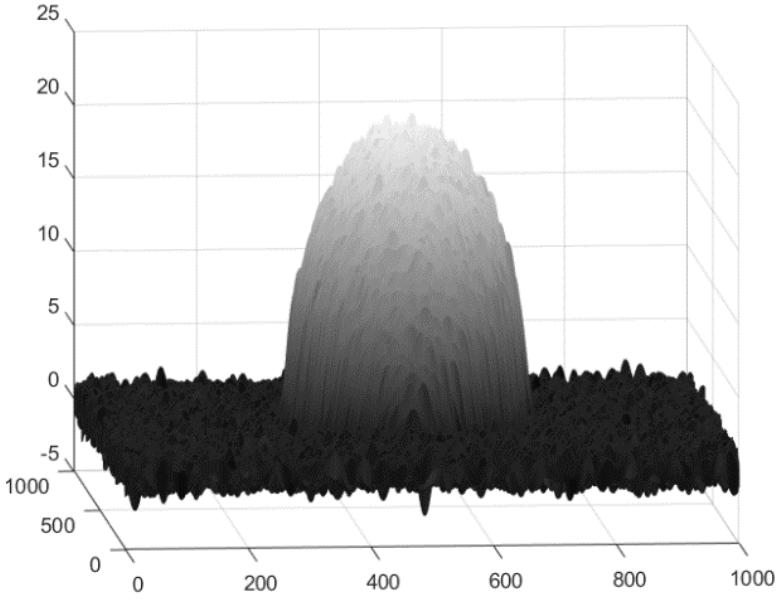


(a)

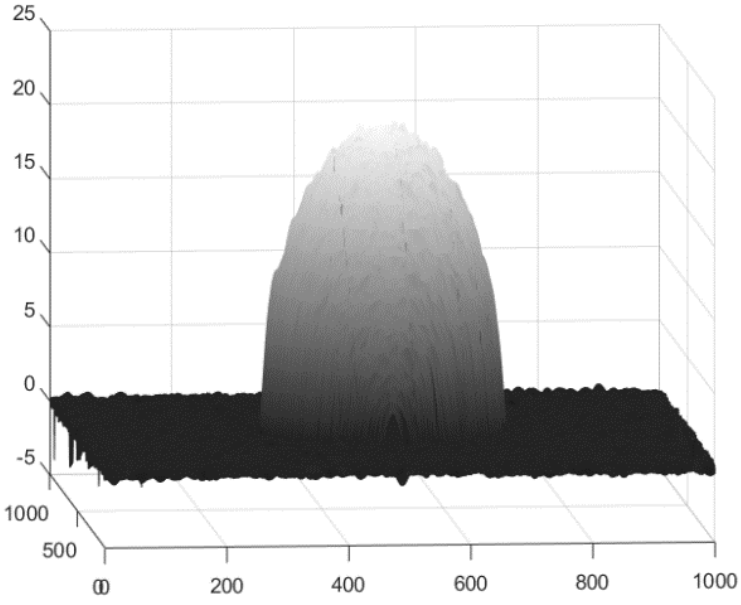


(b)

Fig. 3.4 Verification of the FTP based fusion approach for a 3D dynamic object at SNR=25dB. (a): FTP (b): FTP based fusion approach

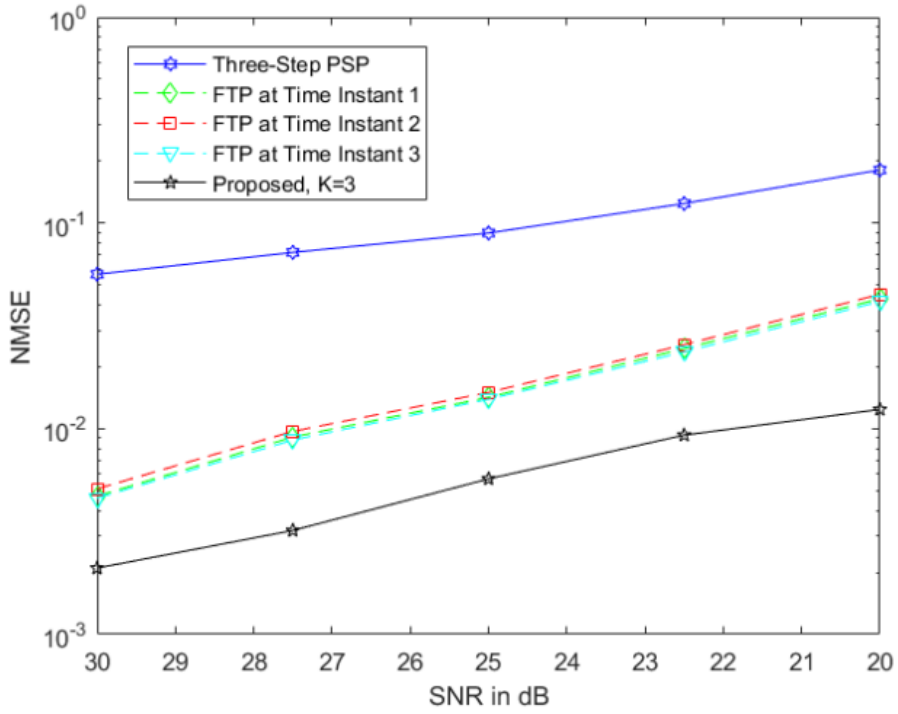


Fig. 3.5 Comparison of the FTP based fusion approach with three-step PSP and FTP.

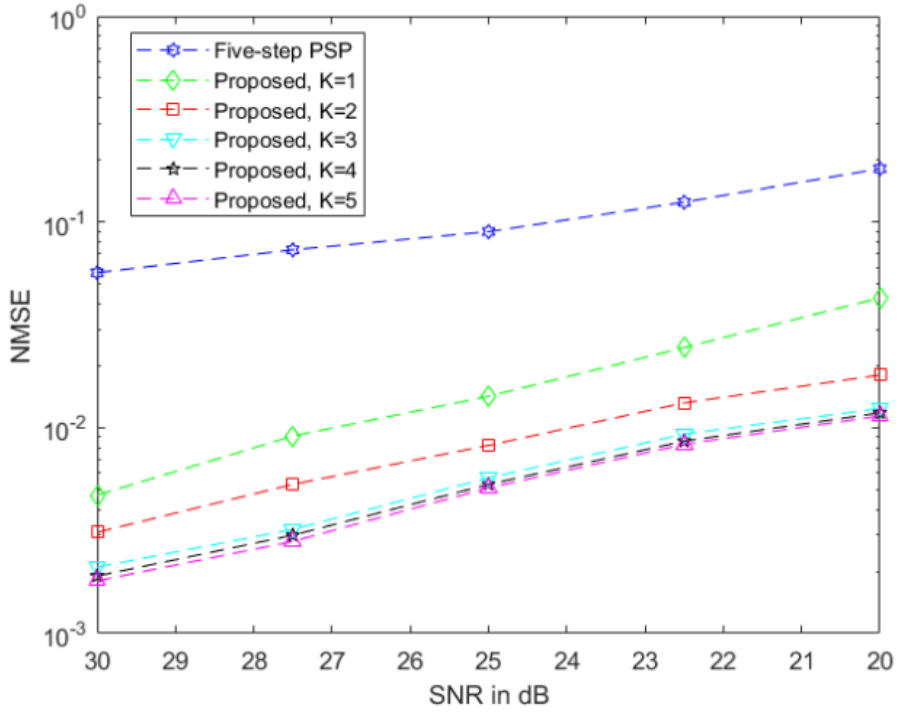


Fig. 3.6 Performance of the FTP based fusion approach with different numbers of height maps fused.

The standard FTP is first tested and its reconstruction result at SNR=25 dB is shown in Fig.3.4(a), achieving an NMSE of 0.0245 for the height measurement. In all simulations, we set $\gamma$=0.1 for the RPCA algorithm. The proposed method fuses the three height maps as shown in Fig. 3.4(b), achieving an NMSE of 0.0065. The NMSE comparisons under different SNRs are shown in Fig. 3.5. It is confirmed that the proposed approach can improve the performance compared to traditional FTP and PSP schemes. Note that the PSP scheme suffers from the motion artifacts. In Fig. 3.6, we also simulate the fusion of different numbers of height maps. The overall NMSE performance of the proposed approach depends on the measurement error of each height map, the motion parameter error from the ICP algorithm and linear interpolation error from height fusion. When $K$ is small, the overall performance is dominated by the original measurement error of each height map. When $K$ is large, the performance is dominated by the modeling errors which cannot be mitigated by increasing $K$. Overall, fusing more height maps can achieve better performance but the improvement of NMSE becomes minor when $K$ is large. In order to balance the computation time and reconstruction accuracy, we set $K$=3 in the experiment.

In the experiment, a gourd shaped object shown in Fig. 3.7 is captured at $K$=3 time instants, with its instantaneous shape illustrated in Fig. 3.8(a), 3.8(b) and 3.8(c). The movement of the object at the three time instants is shown in Fig. 3.8(d). Fig. 3.9(a) shows the performance of a three-step PSP scheme utilizing fringe patterns captured at the three time instants. Clearly, due to the motion artifact, such a PSP scheme performs poorly. The proposed approach applies FTP to obtain three height maps of the dynamic object, and the coarse height map acquired at the time instant 1. The PRCA algorithm is then applied to filter the coarse height map to produce a refined height map, as shown in Fig.3.9(c). The experimental results presented are based on the empirical choice of $\gamma$=0.1 determined from numerical simulations. The ICP algorithm works on the error-

suppressed height maps to estimate the rotation matrix and translation vector. With the uniform sampling rate of 1/500 and around 2000 points from each point cloud, ICP takes about 20 seconds when implemented using MATLAB on an Acer Aspire V 15 laptop with a 2.8 GHz CPU and 16G memory. Finally, the three height maps are fused using the motion parameters and SNR-based weights, as shown in Fig.3.9(d).

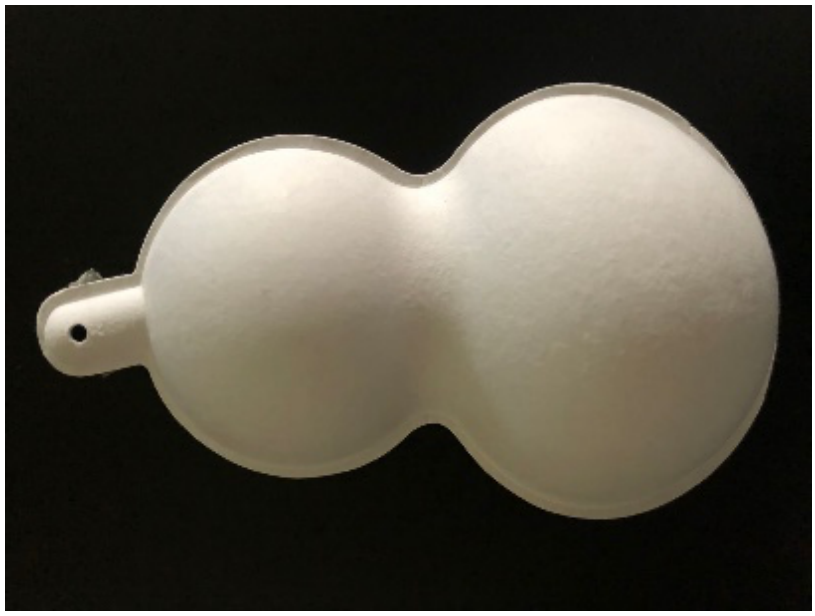

Fig. 3.7 The gourd shaped object.

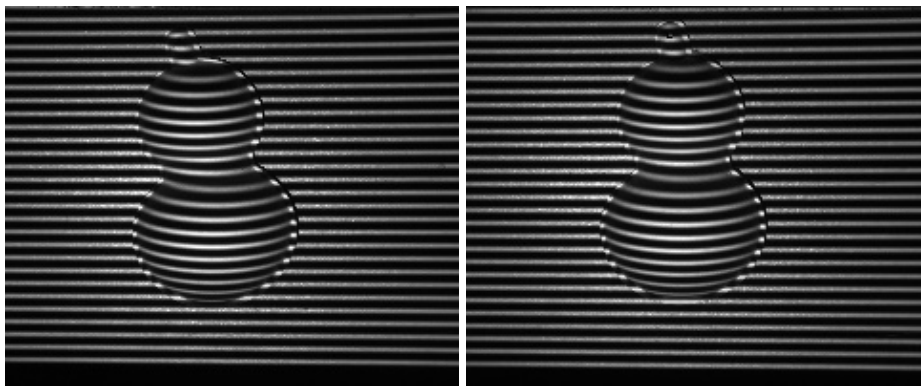

(a) (b)

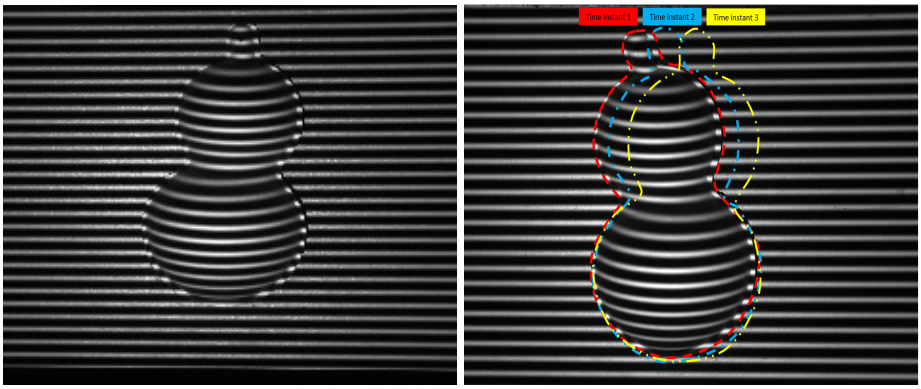


(c) (d)

Fig. 3.8 Dynamic 3D gourd at three time instants and movement trajectory.

In order to evaluate the performance improvement of the FTP based fusion technique over the traditional FTP, we also calculate the NMSE result for the experimental results presented above. As the true shape of the gourd is not known, the nine-step PSP result in Fig.3.10(a) (when the gourd is kept static) is assumed as the true shape. The NMSE with respect to Fig. 3.9 of the cases displayed above are obtained in Table 3.2.

| Traditional three-step PSP | Traditional FTP | RPCA filtered FTP | FTP based fusion approach |
|---|---|---|---|
| 0.6146 | 0.0135 | 0.0115 | 0.0054 |

Table. 3.2 Comparison of the NMSE results of the gourd shaped object

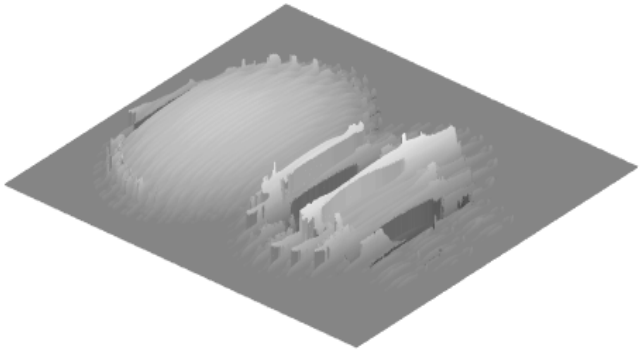

(a)

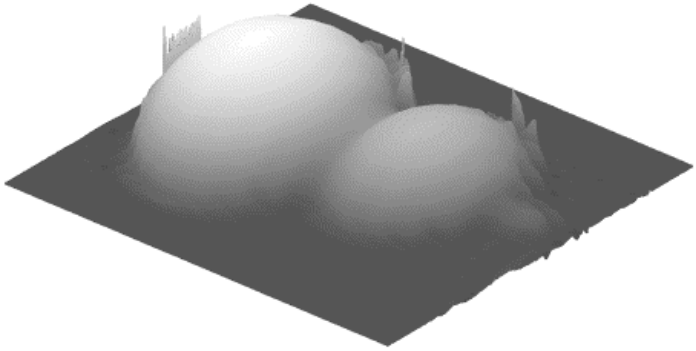

(b)

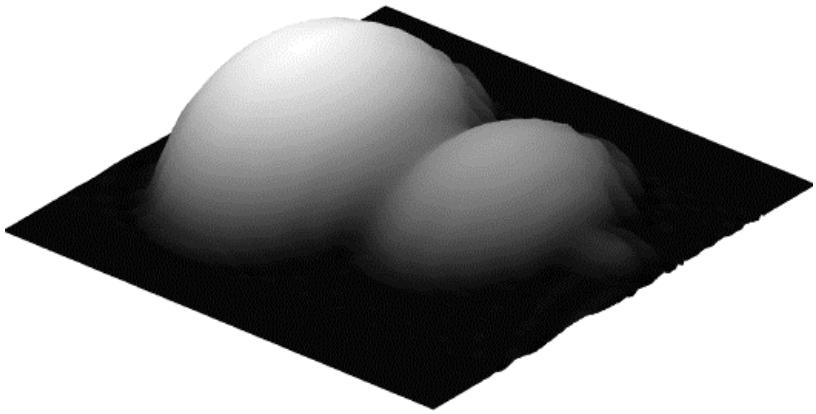

(c)

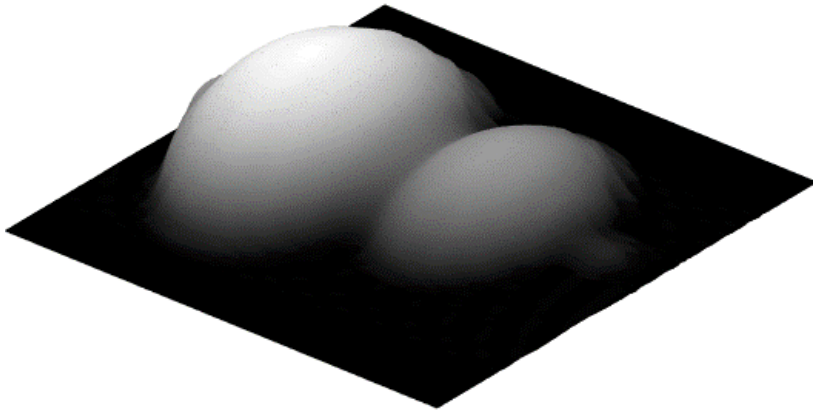

(d)

Fig.3.9 Comparison of the traditional FTP method and the FTP based fusion approach. (a): Results of three-step PSP using fringe patterns captured at the three different time instants in Fig. 3.8. (b): Reconstruction results from FTP. (c): Results obtained by refining (b) by using RPCA. (d): Results after fusing FTP results.

Because the movement of the object leads to the loss of correspondence, the NMSE of the three-step PSP is 0.6146, which indicates the failure of reconstruction. The NMSE of a coarse height map obtained by FTP is 0.0135. When the RPCA algorithm is employed, the NMSE is reduced to 0.0115. After fusing the multiple height maps, the NMSE result is reduced further to 0.0054. Fig.3.11 shows the reconstructed results for the cross sections at x = 800 as indicated in Fig.3.10(b), where the corresponding absolute errors can be observed. It is seen that, the proposed method is able to improve the performance of FTP for 3D dynamic objects.

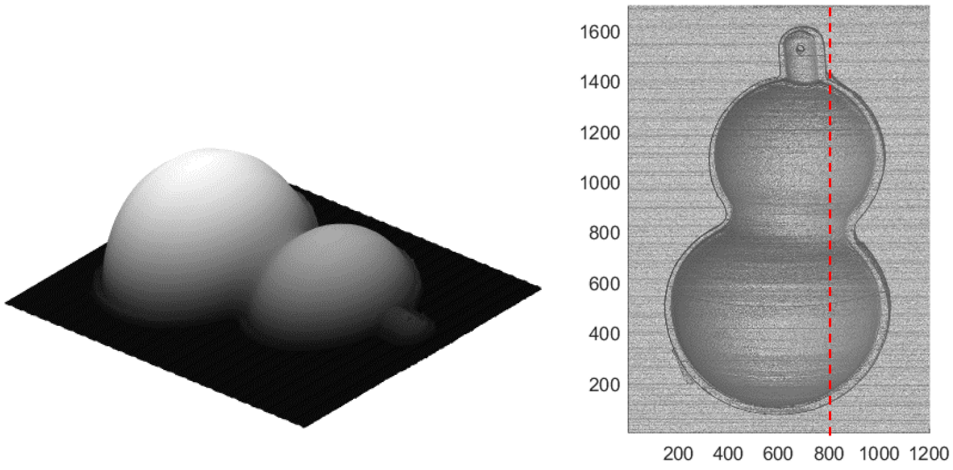


(a) (b)

Fig. 3.10 The result of nine-step PSP when the gourd shaped object is kept static.

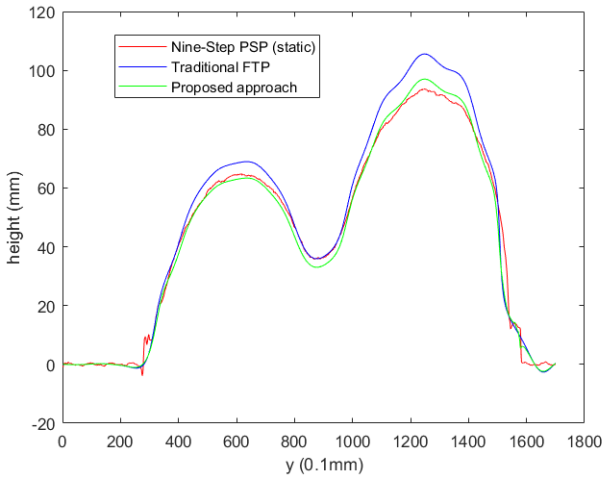


Fig. 3.11 The result of the cross section at x=800 as indicated in Fig. 10(b).

- **PSP based data approach**

Then we verify the effectiveness of the fusion approach when combined with three-step PSP. In the simulation, the movement parameters at the nine time instants are listed in Table 3.3:

| Time instant | $(\alpha, \beta, \theta)$ | $\boldsymbol{t}$(mm) |
|---|---|---|
| 1 | $0°, 0°, 0°$ | (0,0,0) |
| 2 | $-0.16°, -0.16°, 0.32°$ | (1,1,0) |
| 3 | $-0.16°, -0.32°, 0.32°$ | (1,2,1) |
| 4 | $-0.32°, -0.48°, 0.32°$ | (3,3,2) |
| 5 | $-0.48°, -0.48°, 0.32°$ | (3,4,3) |
| 6 | $-0.48°, -0.64°, 0.48°$ | (4,4,3) |
| 7 | $-0.64°, -0.64°, 0.64°$ | (5,6,4) |
| 8 | $-0.80°, -0.64°, 0.48°$ | (6,6,4) |
| 9 | $-0.48°, -0.80°, 0.48°$ | (6,7,4) |

Table. 3.3 Rotation angles and translation distance

A nine-step PSP with $2\pi/9$ phase shift is first tested and its construction result at SNR=30 dB is shown in Fig.3.12(a), achieving an NMSE of 0.0371 for the height measurement. The PSP based fusion approach fuses the three height maps obtained by applying three-step PSP to three states, each spanning three time instants. This way, the NMSE of the fused 3D map as shown in Fig. 3.12(b) is reduced to 0.0065, which is also better than the results from the three-step PSP with NMSE of 0.0249, 0.0190 and 0.0179 achieved at the three states. The NMSE comparisons under different SNRs are shown in Fig. 3.13, which confirms that the PSP based fusion approach can improve the performance compared to traditional PSP schemes. In Fig.3.14, we also simulate the fusion of different numbers of height maps with each obtained by three-step PSP. As we can see, fusing more height maps can achieve better performance. Compared to the model fitting approach from

simulation results, FTP and PSP based fusion approach saves around 85% computation time, while the less accurate reconstruction result will be achieved.

In the experiment, a moving object is captured at $J = 3$ states during its movement, as illustrated in Fig. 3.15. Fig. 3.16(a) shows the performance of a nine-step PSP scheme utilizing fringe patterns captured at nine time instants where each state spans three time instants. Clearly, due to the loss of correspondence, such a PSP scheme performs poorly. The proposed approach applies three-step PSP to obtain three height maps of the dynamic object and the coarse height map acquired at state 1 is shown in Fig.3.16(b). The ICP algorithm works on the coarse height maps to estimate the rotation matrix and translation vector. Finally, the three height maps are fused using the motion parameters and SNR-based weights, as shown in Fig.3.16(c). The experimental results demonstrate that the proposed method is feasible and improves the accuracy as compared to the traditional PSP method.

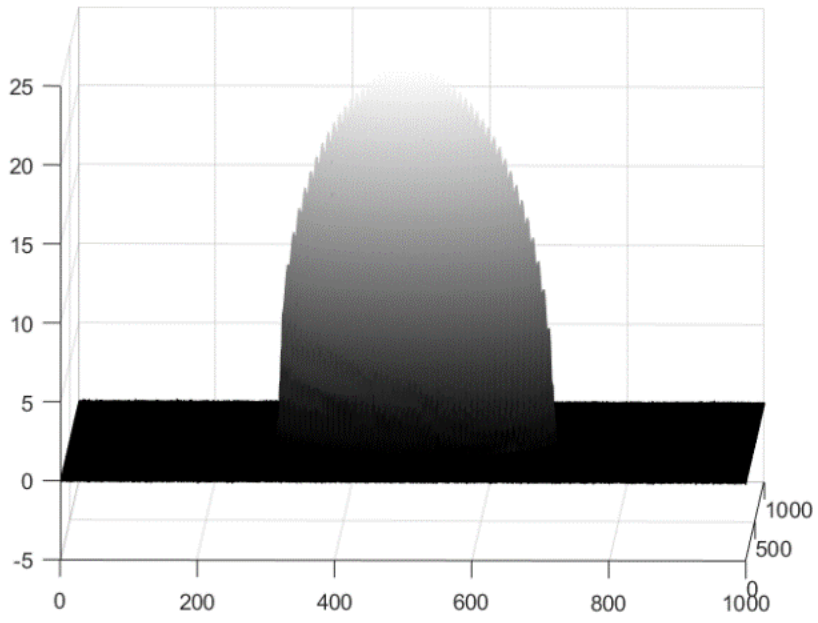


(a)

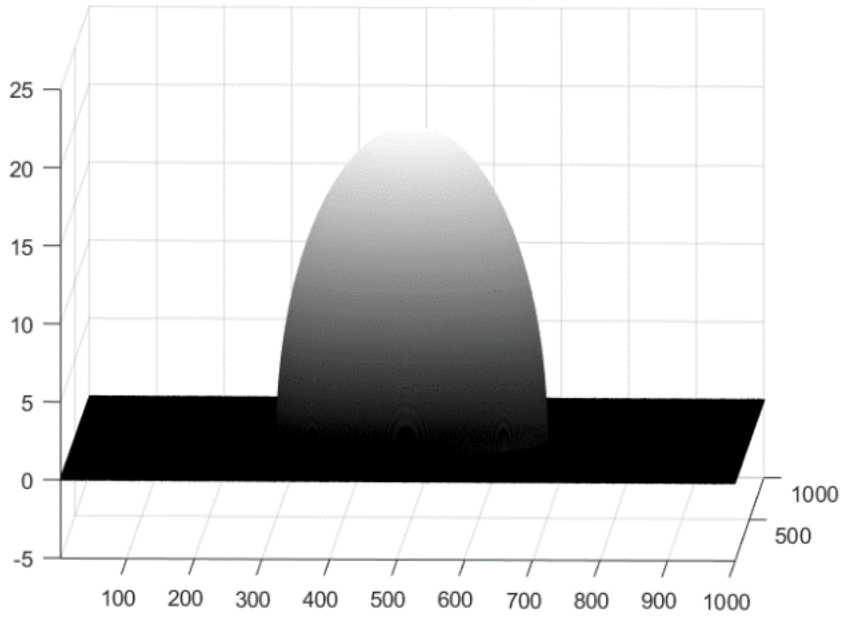


(b)

Fig.3.12 Verification of proposed approach for SNR=30dB. (a): Results of nine-step PSP for a 3D dynamic object. (b): PSP based fusion approach

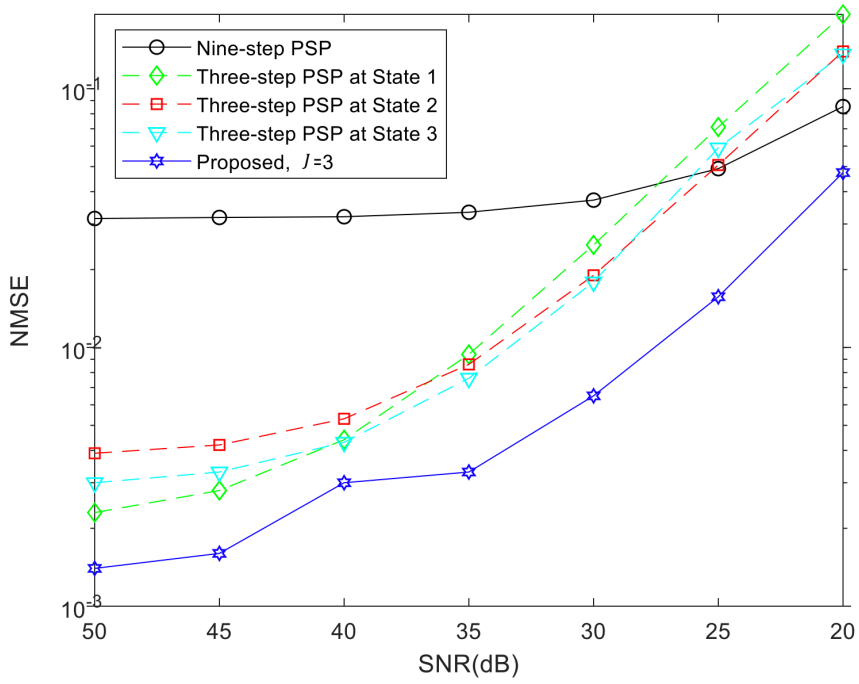


Fig. 3.13 Comparison of the PSP based fusion approach and nine-step PSP

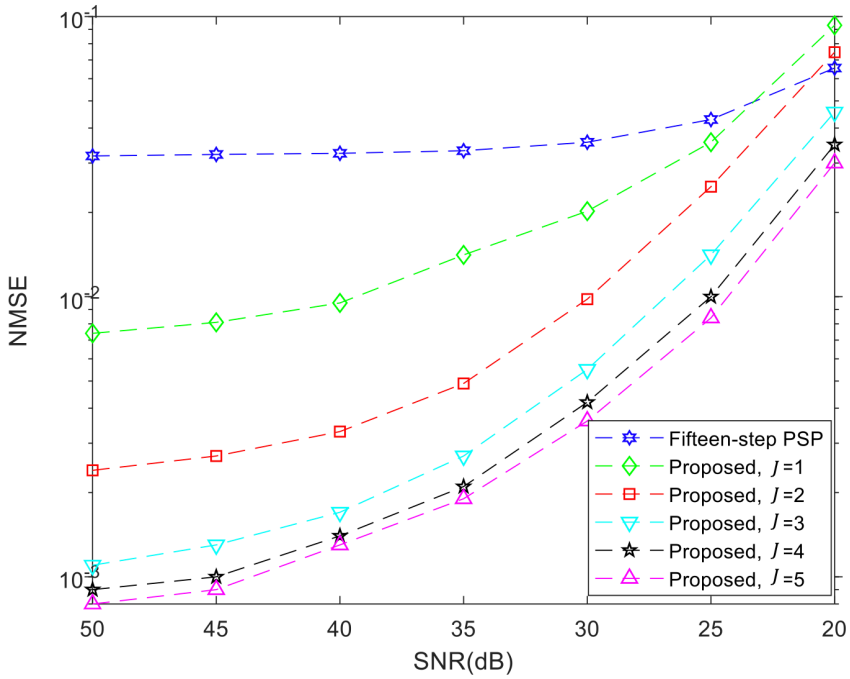


Fig. 3.14 Performance of the PSP based fusion approach with different number of height maps fused

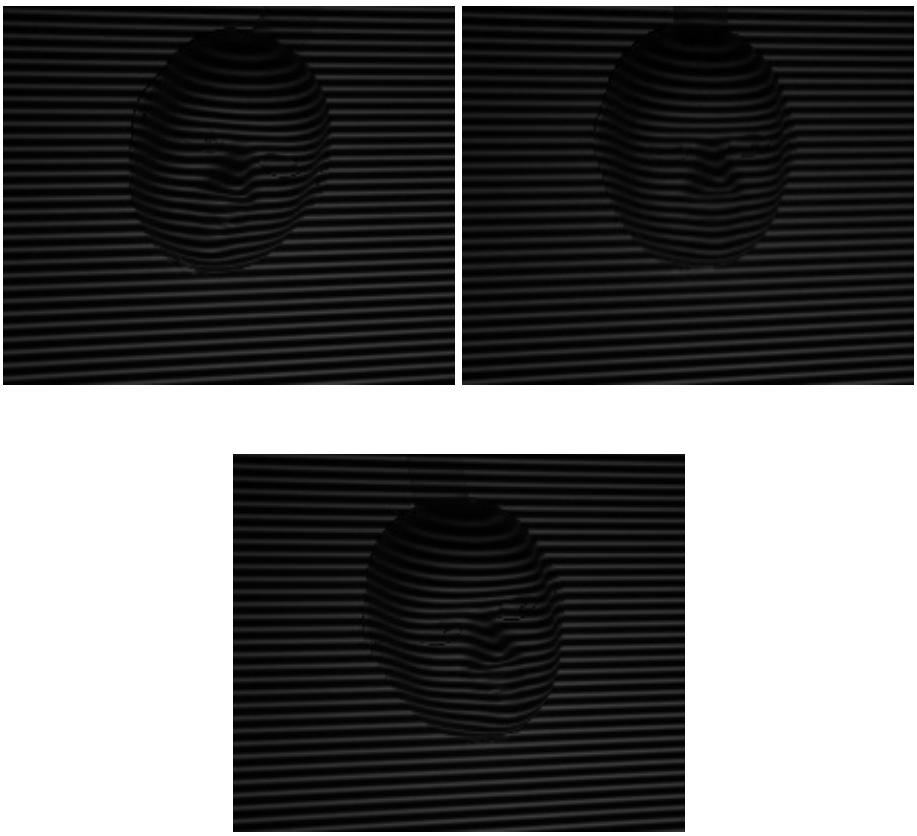

Fig. 3.15 Three states of a dynamic 3D mask.

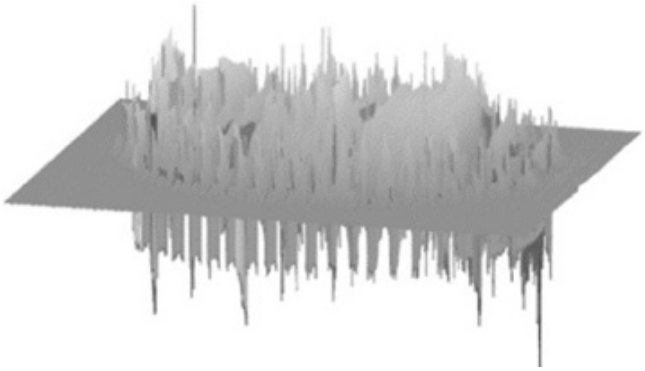

(a)

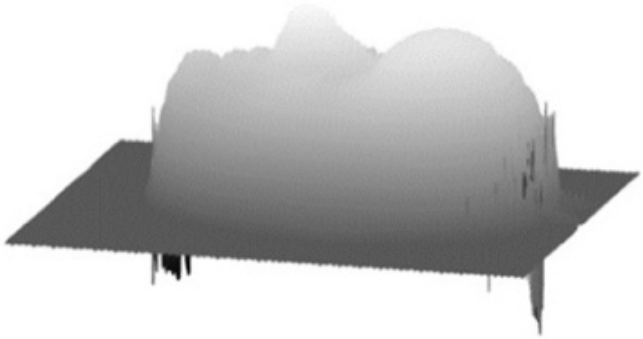

(b)

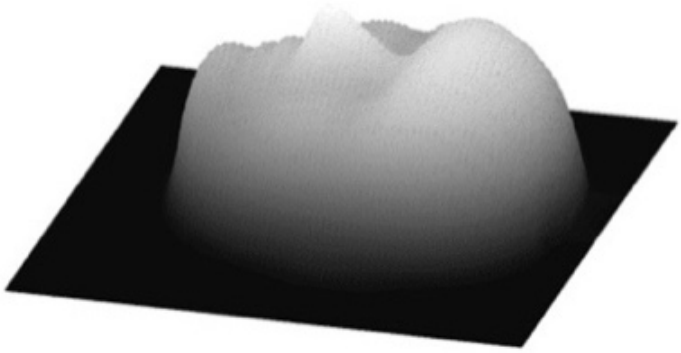

(c)

Fig. 3.16 Comparison of the traditional PSP and the PSP based fusion approach. (a): Results of nine-step PSP using fringe patterns captured at the nine different time instants in Fig. 3.15. (b): Results of PSP using fringe patterns at state 1. (c): Results after fusing the PSP result.

## 3.5 Conclusion

In summary, an FTP based fusion approach has been proposed to enhance the performance for reconstructing 3D dynamic objects. Initial height maps of the object are retrieved by using FTP at each time instant and then filtered using RPCA. The ICP algorithm is then applied to establish the correspondence relationship between 3D point clouds at different time instants. The multiple coarse height maps are fused by applying SNR-based weights. Then, this FTP based fusion approach is extended to PSP based fusion approach to achieve the high-performance reconstruction for dynamic objects without the limitation of the object shape. The performance of the data fusion approaches has been demonstrated by simulations and experiments.

# 4.CONCLUSION AND FUTURE WORKS

This chapter concludes the thesis and discusses potential future work.

## 4.1 Conclusions

This thesis focuses on enhancing the accuracy of measuring 3D shapes of dynamic objects using multiple-shot fringe projection profilometry (FPP). Novel techniques have been proposed to address several key challenges due to the 3D movement of objects. First, rigid 3D movements are described using motion parameters including the rotation matrix and translation vector, and a parameter estimation scheme is devised. Then, the estimated motion parameters are applied to model the fringe patterns deformed by the dynamic objects. Based on this, a model fitting approach is developed to estimate the height. Exploiting the correspondence established using the motion parameters, a data fusion approach is also designed to adaptively combine the height maps obtained at different time instants using standard FPP methods, such that the overall measurement accuracy can be enhanced. The proposed approaches are able to benefit from multiple-shot techniques to suppress the influence from ambient light and reflectivity on the object surface, such that robust and accurate measurements can be achieved. Specifically, the following contributions are made by this thesis.

- **Estimation of the motion parameters for general 3D movements in FPP systems**: A new method has been developed for estimating the rotation matrix and translation vector in multi-shot FPP schemes. In contrast to previous methods, the proposed method does not require markers to be attached or feature points to be extracted. Instead, it utilizes only the coarse height maps obtained using standard

FPP and the iterative ICP algorithm and can thus be well integrated into the FPP systems with minimum human intervention.

- **A model fitting approach for measuring the 3D shape of moving objects:** A key challenge for applying multi-shot FPP to objects with 3D movement is the unknown phase shifts in the captured fringe patterns caused by the change of the position and height of the object surface. In order to address this challenge, we utilize the estimated motion parameters to establish a new model for the fringe patterns captured at different time instants. By fitting the derived model to the acquired fringe patterns, the height distribution of the object is retrieved. This approach compensates for the errors caused by the 3D movement of the object, so that the accuracy of reconstruction can be improved.
- **A data fusion approach for measuring the 3D shape of moving objects:** Instead of fitting the captured fringe patterns as functions of the unknown height for each point on the object surface, we also propose an approach to enhance the measurements by fusing the data from multiple height maps. Coarse height maps are first obtained by applying FTP or PSP (with a small number of fringe patterns) at different time slots. Then the correspondences among these height maps are built by using the motion parameters estimated. This is applied to adaptively fuse the different height maps based on their quality. Denoising based on RPCA and adaptive weight factors determined from estimates of the SNR of the fringe patterns are shown effective to enhance the performance.

The proposed methods can be applied to reconstruct the 3D shape of dynamic objects during the movement. One potential application is the inspection of high-tech discrete manufacturing, which employs robot arm transmission rather than pipeline transmission. In contrast to the pipeline transmission involving dynamic objects with 1D and 2D

movement, the robot arm transmission introduces 3D movement of objects. Besides, the 3D shape measurement for the objects with 3D movement builds a real-time connection of the real world and the virtual world, which may also find applications in virtual reality, metaverse, etc.

## 4.2 Future work

Based on the findings of this study, the following future work can be identified.

- **Complexity reduction:** To obtain the motion parameters, the ICP algorithm is applied to iteratively estimate the rotation matrix and translation vector. Large numbers of iterations and points on the height maps lead to high computational complexity. Also, the model-fitting approach requires the search of the height on a point-by-point basis, which is still time-consuming. Therefore, techniques for reducing the computational complexity of the proposed approaches may be studied to improve the running efficiency of the proposed techniques.
- **Measurements of complex objects**: Both the model-fitting approach and data fusion approach utilize the FTP algorithm to extract the coarse height maps for estimating the motion parameters and initial heights. Furthermore, rigid objects are assumed. The performance of measurement may degrade when the object has a complex, discontinuous, or even non-rigid surface. Extending the proposed techniques to the more challenging cases may be considered for future work.

# 5. REFERENCE

[1] C. Liang-Chia and H. Chung-Chih, “Miniaturized 3D surface profilometer using digital fringe projection,” *Meas. Sci. Technol.*, vol. 16, no. 5, pp. 1061, 2005.

[2] J. Smisek, M. Jancosek, and T. Pajdla, “3D with Kinect,” *Proc. IEEE ICCV Workshops*, pp. 1154-1160, 2011.

[3] V. R. Duseev, and A. N. Malchukov, “Kinect sensor depth data filtering,” Mechanical Engineering Automation and Control Systems (MEACS)", *2014 International Conference on,* pp. 1-4, 2014.

[4] M. F. M. Costa, “Surface inspection by an optical triangulation method,” *Opt. Eng.*, vol. 35, no. 9, pp. 2743–2748, 1996.

[5] D. Borrmann, A. Nüchter, M. Đakulović, I. Maurović, I. Petrović, D. Osmanković, and J. Velagić, “A mobile robot based system for fully automated thermal 3D mapping,” *Adv. Eng. Informat.*, vol. 28, no. 4, pp. 425–440, 2014.

[6] S. T. Yılmaz, U. D. Özug˘urel, K. Bulut, and M. N. Inci, “Vibration amplitude analysis with a single frame using a structured light pattern of a four-core optical fibre”, *Opt. Commun.,* vol. 249, no. 4–6, pp. 515- 522, 2005.

[7] Q. Zhang and X. Su, “High-speed optical measurement for the drumhead vibration”, *Opt. Express*, vol. 13, no. 8, pp. 3110-3116, 2005.

[8] J. S. Massa, G. S. Buller, A. C. Walker, S. Cova, M. Umasuthan, and A. M. Wallace, “Time-of-flight optical ranging system based on time-correlated single-photon counting”, *Appl. Opt.*, vol. 37, no. 31, pp. 7298-7304, 1998.

[9] A. U. Din, I. A. Halin, and S. B. Shafie, “A review on solid state time of flight TOF range image sensors”, *Proc. IEEE Student Conf. Res. Develop.*, pp. 246-249, 2009-Nov.

[10] I. Moring and H. Ailisto, “Active 3-D vision system for automatic model-based shape inspection”, *Opt. Lasers Eng.*, vol. 10, no. 3–4, pp. 149-160, 1989.

[11] A. Kolb, E. Barth, R. Koch, and R. Larsen, “Time-of-flight cameras in computer graphics”, *In Computer Graphics Forum,* vol. 29, pp. 141–159, 2010.

[12] F. Chiabrando, R. Chiabrando, D. Piatti, and F. Rinaudo “Sensors for 3D Imaging: Metric Evaluation and Calibration of a CCD/CMOS Time-of-Flight Camera”, *Sensors*, vol. 9, no. 12, pp. 10080–10096, 2009.

[13] C. P. Keferstein and M. Marxer, “Testing bench for laser triangulation sensors”, *Sensor Rev.*, vol. 18 no. 3, pp.183–187, 1998.

[14] M. E. Bouzouraa, M. Kellner, U. Hofmann, and R. Lutz, “Laser scanner based road surface estimation for automotive applications”, *2014 IEEE SENSORS*, pp. 2034-2037, 2014.

[15] Q. Wu, D. Xu, and W. Zou, "A Survey on Three-Dimensional Modeling Based on Line Structured Light Scanner", *Proceedings of the 33rd Chinese Control Conference*, pp. 7439d-7444, Jul. 2014.

[16] Z. Ji and M. C. Leu, “Design of optical triangulation devices”, *Opt. Laser Tech.*, vol. 21, no. 5, pp. 335–338, 1989.

[17] E. Lilienblum and A. Al-Hamadi, “A structured light approach for 3-D surface reconstruction with a stereo line-scan system”, *IEEE Trans. Instrum. Meas.*, vol. 64, no. 5, pp. 1266-1274, May 2015.

[18] D. Vlasic, P. Peers, I. Baran, P. Debevec, J. Popovic, S. Rusinkiewicz, and W. Matusik, “Dynamic shape capture using multi-view photometric stereo”, *Proc. 28th Annu. Conf. Comput. Graph. Interactive Techn.*, 2009.

[19] L. Zhang, B. Curless, and S.M. Seitz, “Spacetime Stereo: Shape Recovery for Dynamic Scenes”, *Proc. IEEE Conf. Computer Vision and Pattern Recognition*, pp. 367-374, 2003.

[20] M. Z. Brown, D. Burschka, and G. D. Hager, “Advances in computational stereo”, *IEEE Trans. Pattern Analysis and Machine Intelligence*, vol. 25, no. 8, pp. 993–1008, 2003.

[21] R. Zhang, P. Tsai, J. E. Cryer, and M. Shah, “Shape from shading: A survey”, *IEEE Trans. on Pattern Analysis and Machine Intelligence*, vol. 21, no. 8, pp. 690–706, 1999.

[22] B. D. Lucas and T. Kanade, “An iterative image registration technique with an application to stereo vision”, *In IJCAL*, pp. 674-679, 1981.

[23] U. R. Dhond and J. K. Aggarwal, “Structure from stereo a review”, *IEEE Trans-actions on Systems Man and Cybernetics,* vol. 19, no. 6, pp.1489–1510, 1989.

[24] H. Takasaki, “Moiré topography”, *Appl. Opt.*, vol. 9, no. 6, pp. 1467–1472, 1970.

[25] R. Harding and R. Tait, “Moiré techniques applied to automated inspection of machined parts”, in *Proceedings of SME Vision ’86 Conference, Detroit, MI, June 3-5 1986*. Dearborn, MI: Machine Vision Association of SME, 1986.

[26] Z. Yueyi, X. Zhiwei, Y. Zhe, and W. Feng, “Real-Time scalable depth sensing with hybrid structured light illumination”, *IEEE Trans. Image Process.*, vol. 23, no. 1, pp. 97-109, 2014.

[27] Q. Xue, Z. Wang, J. Huang, and J. Gao, “Improving the measuring accuracy of structured light measurement system”, *Opt. Eng.*, vol. 53, no. 11, pp. 112204-112204, 2014.

[28] H. Weidong, G. Mingying, H. Yanhui, S. Lifeng, and Y. Shiqiang, “High- resolution 3D reconstruction for complex color scenes with structured light”, *IEEE International Conference on Multimedia and Expo Workshops (ICMEW)*, pp. 1-6, 2014.

[29] L. Merner, Y. Wang, and S. Zhang, “Accurate calibration for 3D shape measurement system using a binary defocusing technique”, *Opt. Lasers Eng.*, vol. 51, no. 5, pp. 514-519, 2013.

[30] J. Geng, “Structured-light 3D surface imaging: a tutorial”, *Adv. Optics and Photonics*, vol. 3, no. 2, pp. 128-160, 2011.

[31] J. Batlle, E. Mouaddib, and J. Salvi, “Recent progress in coded structured light as a technique to solve the correspondence problem: A survey”, *Pattern Recognit.*, vol. 31, no. 7, pp. 963–982, 1998.

[32] J. Salvi, J. Pages, and J. Batlle, “Pattern codification strategies in structured light systems”, *Pattern Recognit.*, vol. 37, no. 4, pp. 827–849, 2004.

[33] J. Salvi, S. Fernandez, T. Pribanic, and X. Llado, “A state of the art in structured light patterns for surface profilometry”, *Pattern Recognit.*, vol. 43, no.8, pp. 2666–2680, 2010.

[34] Z. Hanqi and Y. Wang, “A coordinate measuring machine with parallel mechanisms”, *IEEE International Conference on Robotics and Automation*, vol. 4, pp. 3256-3261, 1997.

[35] A. Wozniak and M. Dobosz, “Factors influencing probing accuracy of a coordinate measuring machine”, *IEEE Trans. Instrum. Meas.*, vol. 54, no. 6, pp. 2540-2548, 2005.

[36] J. Salvi, S. Fernandez, T. Pribanic, and X. Llado, “A state of the art in structured light patterns for surface profilometry”, *Pattern Recognit.,* vol. 43, no. 8, pp. 2666-2680, 2010.

[37] H. Hirschmller, “Accurate and Efficient Stereo Processing by Semi-Global Matching and Mutual Information”, *Proc. IEEE Conf. Computer Vision and Pattern Recognition*, vol. 2, pp. 807-814, 2005-June.

[38] K. Schreve, “How accurate can a stereovision measurement be?”, *Proc. 15th Int. Workshop Res. Edu. Mechatronics (REM)*, pp. 1-7, 2014.

[39] H. H. Kawasaki, R. Furukawa, R. Sagawa, and Y. Yagi, “Dynamic scene shape reconstruction using a single structured light pattern”, *Proc. IEEE Conf. Comput. Vision Pattern Recogn.*, pp. 1-8, 2008.

[40] S. Hsu, S. Acharya, A. Rafii, and R. New, “Performance of a time-of-flight range camera for intelligent vehicle safety applications”, *in Advanced Microsystems for Automotive Applications, Berlin, Germany:Springer*, pp. 205-219, 2006.

[41] E. Lachat, H. Macher, M.-A. Mittet, T. Landes, and P. Grussenmeyer, “First experiences with Kinect V2 sensor for close range 3D modelling”, *Proc. Int. Arch. Photogram. Remote Sens. Spatial Inf. Sci. (ISPRS)*, vol. XL-5/W4, pp. 93-100, 2015.

[42] S. Zhang, “High-Speed 3D imaging with digital fringe projection techniques”, *CRC Press*, vol. 5, 2016.

[43] J. Franca, M. Gazziro, A. Ide, and J. Saito, “A 3D scanning system based on laser triangulation and variable field of view”, *Proc. IEEE Int. Conf. Image Process.*, vol. 1, pp. 425-428, Sep. 2005.

[44] F. J. Shiou and M. X. Liu, “Development of a novel scattered triangulation laser probe with six linear charge-coupled devices (ccds)”, *Opt. Lasers Eng.*, vol. 47, no.1, pp. 7-18, 2009.

[45] J. Wu, R. Chang, and J. Jiang, “A novel pulse measurement system by using laser triangulation and a CMOS image sensor”, *Sensors*, vol.7, no.12, pp. 3366-3385, 2007.

[46] S. Chen, Y. Li, and J. Zhang, “Vision Processing for Realtime 3-D Data Acquisition Based on Coded Structured Light”, *IEEE Trans. Image Processing,* vol.17, no.2, pp. 167-176, 2008.

[47] P. M. Grin, L. S. Narasimhan, and S. R. Yee, “Generation of uniquely encoded light patterns for range data acquisition”, *Pattern recognit.*, vol. 25, no. 6, pp. 609–616, 1992.

[48] M. Takeda, H. Ina, and S. Kobayashi, “Fourier-transform method of fringe pattern analysis for computer-based topography and interferometry”, *J. Opt. Soc. Amer.,* vol. 72, no. 1, pp. 156-160, 1982.

[49] L. Chen, C. Quan, C. J. Tay, and Y. Fu, “Shape measurement using one frame projected sawtooth fringe pattern”, *Opt. Commun.,* vol. 246, no. 4-6, pp. 275-284, 2005.

[50] Z. Zhang, C. E. Towers, and D. P. Towers, “Time efficient color fringe projection system for 3D shape and color using optimum 3-frequency Selection”, *Opt. Express,* vol. 14, no. 14, pp. 6444-6455, 2006.

[51] Z. H. Zhang, C. E. Towers, and D. P. Towers, “Phase and colour calculation in colour fringe projection”, *J.Opt. A,* vol. 9, no. 6, pp. S81, 2007.

[52] W.-H. Su, “Color-encoded fringe projection for 3D shape measurements”, *Opt. Express,* vol. 15, no. 20, pp. 13167-13181, 2007.

[53] H. J. Chen, J. Zhang, D. J. Lv, and J. Fang, “3-D shape measurement by composite pattern projection and hybrid processing”, *Opt. Express,* vol. 15, no. 19, pp. 12318-12330, 2007.

[54] W.H. Su, “Projected fringe profilometry using the area-encoded algorithm for spatially isolated and dynamic objects”, *Opt. Express,* vol. 16, no. 4, pp. 2590-2596, 2008.

[55] Z. Zhang, D. P. Towers, and C. E. Towers, “Snapshot color fringe projection for absolute three-dimensional metrology of video sequences”, *Appl Opt.,* vol. 49, no. 31, pp. 5947-5953, 2010.

[56] Z. H. Zhang, “Review of single-shot 3D shape measurement by phase calculation-based fringe projection techniques”, *Opt. Lasers Eng.,* vol. 50, no. 8, pp. 1097-1106, 2012.

[57] K. Liu, W. Yongchang, D. Lau, Q. Hao, and L. Hassebrook, “Dual-frequency pattern scheme for high-speed 3-D shape measurement”, *Opt. express,* vol.18, no.5, pp.5229-44, 2010.

[58] I. Ishii, K. Yamamoto, K. Doi, and T. Tsuji, “High-speed 3D image acquisition using coded structured light projection”, *Proc. IEEE/RSJ Int. Conf. Intell. Robots Syst.*, pp. 925-930, 2007-Oct.–Nov.

[59] R. J. Valkenburg and A. M. McIvor, “Accurate 3D measurement using a structured light system”, *Image Vis. Comput.,* vol. 16, no. 2, pp. 99-110, 1998.

[60] J. L. Posdamer and M. D. Altschuler, “Surface measurement by space encoded projected beam systems”, *Comput. Graphics Image Processing,* vol. 18, no. 1, pp. 1-17, 1982.

[61] J. Pan, P. S. Huang, S. Zhang, and F. Chiang, “Color N-ARY gray code for 3-D shape measurement”, *12th International Conference on Experimental Mechanics*, 2004.

[62] D. Caspi, N. Kiryati, and J. Shamir, “Range imaging with adaptive color structured light”, *IEEE Trans. on Pattern Analysis and Machine Intelligence,* vol. 20, no. 5, pp. 470-480, 1998.

[63] E. Horn, and N. Kiryati, “Toward optimal structured light patterns”, *in 3-D Digital Imaging and Modeling, International Conference on Recent Advances*, pp. 28-35, 1997

[64] S. Inokuchi, K. Sato, and F. Matsuda, “Range-imaging for 3-D object recognition”, *in International Conference on Pattern Recognition (International Association for Pattern Recognition*, pp. 806–808, 1984.

[65] P. Jia, J. Kofman, and C. English, “Error compensation in two-step triangular-pattern phase-shifting profilometry”, *Opt. Lasers Eng.,* vol. 46, no. 4, pp. 311-320, 2008.

[66] P. Jia, J. Kofman, C. English, and A. Deslauriers, “Two-Step Triangular Phase-Shifting Method for 3-D Object-Shape Measurement”, *Proceedings of SPIE*, vol. 6049, pp. 141-150, 2005.

[67] P. Jia, J. Kofman, and C. English, “Two-step triangular-pattern phase-shifting method for three-dimensional object shape measurement”, *Opt. Eng.,* vol. 46, no. 8, pp. 083201, 2007.

[68] P. Jia, J. Kofman, and C. English, “Multiple-step triangular-pattern phase shifting and the influence of number of steps and pitch on measurement accuracy”, *Appl. Opt.,* vol. 46, no. 16, pp. 3253-3262, 2007.

[69] T. Miyasaka, K. Kuroda, M. Hirose, and K. Araki, “Reconstruction of realistic 3D surface model and 3D animation from range images obtained by real time 3D measurement system”, *International Conference on Pattern Recognition,* vol. 15, no. 4, pp. 594-597, 2000.

[70] G. Chazan and N. Kiryati, “Pyramidal intensity-ratio depth sensor”, *Technion Israel Institute of Technology*, 1995.

[71] P. S. Huang, S. Zhang, and F. P. Chiang, “Trapezoidal phase-shifting method for three-dimensional shape measurement”, *Opt. Eng.,* vol. 44, no. 12, pp. 123601, 2005.

[72] B. Budianto, P. Lun, and T. Hsung, “Marker encoded fringe projection profilometry for efficient 3d model acquisition”, *Appl. Opt.*, vol. 53, pp. 7442–7453, 2014.

[73] Y. Hu, Q. Chen, Y. Zhang, S. Feng, T. Tao, H. Li, W. Yin, and C. Zuo, “Dynamic microscopic 3d shape measurement based on marker-embedded fourier transform profilometry”, *Appl. Opt.*, vol. 57, pp. 772–780, 2018.

[74] Y. Zhang, Z. Xiong, and F. Wu, “Unambiguous 3D measurement from speckle-embedded fringe”, *Appl. Opt..* vol. 52, no. 32, pp. 7797–7805, 2013.

[75] S. Zhang, “High-resolution 3D profilometry with binary phase-shifting methods”, *Appl. Opt.,* vol. 50, no. 12, pp. 1753-1757, 2011.

[76] G. Lai and T. Yatagai, “Generalized phase-shifting interferometry”, *J. Opt. Soc. Am. A,* vol. 8, no. 5, pp. 822-827, 1991.

[77] X. Su, W. Zhou, G. V. Bally, and D. Vukicevic, “Automated phase measuring profilometry using defocused projection of a Ronchi grating”, *Opt. Commun.,* vol. 94, no. 6, pp. 561-573, 1992.

[78] H. Su, J. Li, and X. Su, “Phase algorithm without the influence of carrier frequency”, *Opt. Eng.,* vol. 36, no. 6, pp. 1799-1805, 1997.

[79] S. Feng, Q. Chen, G. Gu, T. Tao, L. Zhang, Y.Hu, W. Yin, and C. Zuo, “Fringe pattern analysis using deep learning”, *Adv. Photonics*., vol. 1, no. 02, pp. 1-7, 2019.

Fringe pattern analysis using deep learning

[80] C. Zuo, J. Qian, S. Feng, W. Yin, Y. Li, P. Fan, J. Han, K. Mao, and Q. Chen, “Deep learning in optical metrology: a review”, *Light Sci. Appl.,* vol. 11, no. 39, pp. 2047-7538, 2022.

[81] W. Yin, Q. Chen, S. Feng, T. Tao, L. Huang, M. Trusiak, A. Asundi, and C. Zuo, “Temporal phase unwrapping using deep learning”, Sci. Rep., vol. 9, no. 1, pp. 20175-12, 2019.

[82] M. Cywinska, F. Brzeski, W. Krajnik, K. Patorski, C. Zuo, and M. Trusiak, “Deep Density: Convolutional neural network based estimation of local fringe pattern density”, *Opt. Lasers Eng.*, vol. 145, no. 4, pp.106675, 2021.

[83] T. Weise, B. Leibe, and L. Van Gool, “Fast 3D scanning with automatic motion compensation”, *IEEE Conference on Computer Vision and Pattern Recognition,* pp. 1-8, 2007.

[84] S. Yoneyama, Y. Morimoto, M. Fujigaki, and Y. Ikeda, “Three-dimensional surface profile measurement of a moving object by a spatial-offset phase stepping method”, *Opt. Eng.,* vol. 42, no. 1, pp. 137-142, 2003.

[85] Y. Cao, Y. Wu, K. Peng, and M. Lu, “A new method using orthogonal two-frequency grating in online 3D measurement”, *Opt. Laser Tech.*, vol. 83, pp. 81-88, 2016.

[86] Y. Li, Y. Cao, Z. Huang, D. Chen, and S. Shi, “A three dimensional on-line measurement method based on five unequal steps phase shifting”, *Opt. Commun.,* vol. 285, no. 285, pp. 4285-4289, 2012.

[87] J. Wang, “A novel 3D measurement technique for rigid moving objects with a determined movement trajectory and constant movement speed”, *AIP adv.*, vol. 9, pp. 055227, 2019.

[88] P. Cong, Z. Xiong, Y. Zhang, S. Zhao, and F. Wu, “Accurate dynamic 3D sensing with Fourier-assisted phase shifting”, *IEEE J. Sel. Topics Signal Process.*, vol. 9, no. 3, pp. 396-408, 2015.

[89] S. Feng, C. Zuo, T. Tao, Y. Hu, M. Zhang, C. Qian, and G. Gu, “Robust dynamic 3-D measurements with motion-compensated phase-shifting profilometry”, *Opt. Lasers Eng.*, vol. 103, pp. 127-138, 2018.

[90] Z. Liu, P. C. Zibley, and S. Zhang, “Motion-induced error compensation for phase shifting proilometry”, *Opt. Express*, vol. 26, no. 10, pp. 12632-12637, 2018.

[91] M. Duan, Y. Jin, C. Xu, X. Xu, C. Zhu, and E. Chen, “Phase-shifting profilometry for the robust 3-D shape measurement of moving objects”, *Opt. Express*, vol. 27, no. 16, pp. 22100-22115, 2019.

[92] X. Liu, T. Tao, Y. Wan, and J. Kofman, “Real-time motion-induced-error compensation in 3D surface-shape measurement”, *Opt. Express*, vol. 27, no. 18, pp. 25265-25279, 2019.

[93] L. Lu, J. Xi, Y. Yu, and Q. Guo, “New approach to improve the accuracy of 3-D shape measurement of moving object using phase shifting profilometry”, *Opt. Express*, vol. 21, no. 25, pp. 30610–30622, 2013.

[94] L. Lu, Y. Ding, Y. Luan, Y. Yin, Q. Liu, and J. Xi. “Automated approach for the surface profile measurement of moving objects based on PSP”, *Opt. Express*, vol. 25, no. 25, pp. 32120, 2017.

[95] S. Zhang and S. T. Yau, “High-speed three-dimensional shape measurement system using a modified two-plus-one phase-shifting algorithm”, *Opt. Eng.,* vol. 46, no. 11, pp. 113603, 2007.

[96] L. Lu, J. Xi, Y. Yu, and Q. Guo, “Improving the accuracy performance of phase-shifting profilometry for the measurement of objects in motion”, *Opt. lett.*, vol. 39, no. 23, pp. 6715–6718, 2014.

[97] J. Li, X. Su, and L. Guo, “Improved fourier transform profilometry for the automatic measurement of three-dimensional object shapes”, *Opt. Eng.*, vol. 29, pp. 1439-1444, 1990.

[98] E. Hu and Y. He, “Surface profile measurement of moving objects by using an improved π phase-shifting Fourier transform profilometry”, *Opt. Lasers Eng.,* vol. 47, no. 1, pp. 57-61, 2009.

[99] X. Su, W. Chen, Q. Zhang, and Y. Chao, “Dynamic 3-D shape measurement method based on FTP”, *Opt. Lasers Eng.*, vol. 36, no. 1, pp. 49-64, 2001.

[100] J. Lin and X. Su, “Two-dimensional Fourier transform profilometry for the automatic measurement of three-dimensional object shapes”, *Opt. Eng.*, vol. 34, pp. 3297, 2006.

[101] S. Zhang, “Phase unwrapping error reduction framework for a multiple- wavelength phase-shifting algorithm”, *Opt. Eng.*, vol. 48, no. 10, pp. 105601-105608, 2009.

[102] J.M. Huntley and H.O. Saldner, “Temporal phase-unwrapping algorithm for automated interferogram analysis”, *Appl. Opt.*, vol. 32, no. 17, pp. 3047-3052, 1993.

[103] R. M. Goldstein, H. A. Zebker, and C. L. Werner, “Satellite radar interferometry: Two dimensional phase unwrapping”, *Radio Sci.,* vol. 23, no. 4, pp. 713-720, 1988.

[104] H. Zhao, W. Chen, and Y. Tan, “Phase-unwrapping algorithm for the measurement of three-dimensional object shapes”, *Appl. Opt.,* vol. 33, no. 20, pp. 4497-4500, 1994.

[105] S. Fang, L. Meng, L. Wang, P. Yang, and M. Komori, “Quality-guided phase unwrapping algorithm based on reliability evaluation”, *Appl. Opt.,* vol. 50, no. 28, pp. 5446-5452, 2011.

[106] Y. Ding, J. Xi, Y. Yu, W. Cheng, S. Wang, and J. F. Chicharo, “Frequency selection in absolute phase maps recovery with two frequency projection fringes”, *Opt. Express,* vol. 20, no. 12, pp. 13238-13251, 2012.

[107] J. Lu and H. Su, “Fast phase unwrapping algorithm based on region partition for structured light vision measurement”, *Opt. Eng.,* vol. 53, no. 4, pp. 044103, 2014.

[108] W. Lohry, V. Chen, and S. Zhang, “Absolute three-dimensional shape measurement using coded fringe patterns without phase unwrapping or projector calibration”, *Opt. Express,* vol. 22, no. 2, pp. 1287-1301, 2014.

[109] E. Zappa and G. Bus Ca, “Comparison of eight unwrapping algorithms applied to Fourier-transform profilometry”, *Opt. Lasers Eng.,* vol. 46, no. 2, pp. 106-116, 2008

[110] R. Goldestein, H. Zebker, and C. Werner, “Satellite radar interferometry: two-dimensional phase unwrapping”, *Radio Sci.,* vol. 23, no. 4, pp. 713–720, 2016.

[111] X. Xie, Y. Liu, Z. Shou, Q. Zeng, G. Wang, Q. Huang, and X. Gao, “ Phase unwrapping algorithm based on a rank information filter”, *Appl. Opt.*, vol. 60, no. 22, pp. 6648-6658, 2021.

[112] D. Bone, “Fourier fringe analysis: the two-dimensional phase unwrapping problem”, *Appl. Opt.,* vol. 30, no. 25, pp. 3627–3632, 1991.

[113] T. Flynn, “Two-dimensional phase unwrapping with minimum weighted discontinuity”, *J. Opt. Soc. Am. A*, vol. 14, no. 10, pp.2692–2701, 1997.

[114] M. Pritt, “Phase unwrapping by means of multigrid techniques for interferometric SAR”, *IEEE Trans. on Geosci. Remote Sensing*, vol. 34, no. 3, pp. 728–738, 1996.

[115] D. Ghiglia and L. Romero, “Robust two-dimensional weighted and unweighted phase unwrapping that uses fast transforms and iterative methods”, *J. Opt. Soc. Am. A,* vol. 11, no. 1, pp. 107-117, 1994.

[116] M. A. Herráez, D. R. Burton, M. J. Lalor, and M. A. Gdeisat, “Fast two-dimensional phase-unwrapping algorithm based on sorting by reliability following a noncontinuous path”, *Appl. Opt.*, vol. 41, no. 35, pp. 7437-7444, 2002.

[117] W. Lan, N. Li, and Q. Tong, “PointNetLK-OBB: A Point Cloud Registration Algorithm with High Accuracy”, *International Journal of Computer and Information Engineering*, vol. 15, no. 5, pp. 296-304, 2021.

[118] P. Biber and W. Straßer, “The Normal Distributions Transform: A New Approach to Laser Scan Matching”, *Proc. IEEE/RSJ Int'l Conf. Intelligent Robots and Systems*, pp. 2743-2748, 2003.

[119] M. Magnusson, A. Lilienthal, and T. Duckett, “Scan registration for autonomous mining vehicles using 3D-NDT”, *J. Field Robotics*, vol. 24, no. 10, pp. 803–827, 2007.

[120] L. Montesano, J. Minguez, and L. Montano, “Probabilistic scan matching for motion estimation in unstructured environments”, *IEEE/RSJ International Conference on Intelligent Robots and Systems*, 2005

[121] Y. Chen and G. Medioni, “Object modeling by registration of multiple range images”, *IEEE International Conference on Robotics and Automation,* vol. 3, pp. 2724-2729, 1991.

[122] P. J. Besl and H. D. Mckay, “A method for registration of 3-d shapes”, *IEEE Trans. on Pattern Analysis & Machine Intelligence*, vol. 14, no. 2, pp. 239-256, 1992.

[123] A. Zhang, W. Sun, C. Ge, and F. Li, “Fast global registration of multiple 3D data sets from outdoor large scenes”, *High Tech. Lett.,* vol. 14, pp. 6-13, 2004.

[124] P. J. Besl and N. D. Mckay, “A method for registration of 3-D shapes”, *IEEE Trans. on Pattern Analysis & Machine Intelligence.* vol.14, no.2, pp.239-256, 1992.

[125] K. Pulli, “Multiview Registration for Large Data Sets”, *Proc. Second Int'l Conf. 3-D Imaging and Modeling*, pp. 160-168, 1999-Oct.

[126] Y. Wu, W. Wang, K. Lu, K, Y. Wei, and Z. Chen, “A new method for registration of 3D point sets with low overlapping ratios”, *Procedia CIRP,* vol. 27, pp. 202–206, 2015.

[127] R. Huang, Y. Xu, W. Yao, L. Hoegner, and U. Stilla, “Robust global registration of point clouds by closed-form solution in the frequency domain”, *ISPRS J. Photogrammetry Remote Sens.*, vol. 171, pp. 310-329, 2021

[128] D. Aiger, N. J. Mitra, and D. Cohenor, “4-Points congruent sets for robust pairwise surface registration”, *ACM Trans. Graphics,* vol. 27, pp. 85–94, 2008.

[129] X. Ge, “Non-rigid registration of 3D point clouds under isometric deformation”, *ISPRS J. Photogrammetry Remote Sens.,* vol. 121, pp. 192–202, 2016.

[130] S. Rusinkiewicz and M. Levoy, “Efficient variants of the ICP algorithm”, *3-D Digital Imaging and Modeling 2001. Proceedings. Third International Conference*, pp. 145-152, 2001.

[131] F. Wang and Z. Zhao, “A survey of iterative closest point algorithm”, *Proc. Chin. Autom. Congr. (CAC)*, pp. 4395-4399, 2017.

[132] J. Minguez, L. Montesano, and F. Lamiraux, “Metrix-based iterative closest point scan matching for sensor displacement estimation”, *IEEE Trans.Robot.*, vol. 22, no. 5, pp. 1047-1054, 2006.

[133] V. Chandrasekaran, S. Sanghavi, P. A. Parrilo, and A. S. Willsky, “Rank-sparsity incoherence for matrix decomposition”, *SIAM J. Optimization*. vol. 21, no. 2, pp. 572–596, 2011.

[134] A. Beck and M. Teboulle, “A fast iterative shrinkage-thresholding algorithm for linear inverse problems”, *SIAM J. Imag. Sci.*, vol. 2, no.1, pp.183–202, 2009.

[135] R. Gnanadesikan and J. Kettenring, J, “Robust estimates, residuals, and outlier detection with multiresponse data”, *Biometrics,* vol. 28, pp. 81–124, 1972.

[136] M. Fishler and R. Bolles, “Random sample consensus: A paradigm for model fitting with applications to image analysis and automated cartography”, *Comm. ACM*, vol. 24, pp. 381–385, 1981.

[137] Q. Ke and T. Kanade, “Robust -Norm Factorization in the Presence of Outliers and Missing Data by Alternative Convex Programming”, *Proc. IEEE Conf. Computer Vision and Pattern Recognition*, pp. 739-746, 2005.

[138] F. de la Torre and M.J. Black, “A Framework for Robust Subspace Learning”, *Int'l J. Computer Vision*, vol. 54, no. 1, pp. 117-142, 2003.

[139] J. Wright, Y. Peng, Y. Ma, A. Ganesh, and S. Rao, “Robust principal component analysis: Exact recovery of corrupted low-rank matrices by convex optimization”, *NIPS*, vol. 58, pp. 289-298, 2009.

[140] N. Vaswani, T. Bouwmans, S. Javed, and P. Narayanamurthy, “Robust subspace learning: Robust PCA, robust subspace tracking, and robust subspace recovery”, *IEEE Signal Process. Mag.*, vol. 35, no. 4, pp. 32–55, 2018.

[141] E. J. Candès, X. Li, Y. Ma, and J. Wright, “Robust principal component analysis” *J. ACM*, vol. 58, no. 3, pp. 1-37, 2011.

[142] X. Yuan and J. Yang, “Sparse and low-rank matrix decomposition via alternating direction methods”, *Pac. J. Optim.*, vol. 9, no. 1, pp. 167–180, 2013.

[143] V. A. Aalo and J. Zhang, “Performance analysis of maximal ratio combining in the presence of multiple equal-power cochannel interferers in a Nakagami fading channel”, *IEEE Trans. Veh. Technol.*, vol. 50, no. 2, pp. 497–503, 2001.